EXPERIMENTAL AND THEORETICAL STUDY OF HYDRAULIC FRACTURING IN IMPERMEABLE AND PERMEABLE MATERIALS

Final Report

October 1981

By: M. B. Rubin

Project Supervisor: A. L. Florence

Prepared for:

DEPARTMENT OF ENERGY
Morgantown Energy Technology Center
Collins Ferry Road
Morgantown, West Virginia 26505

Attention: Dr. C. Komar

Contract No. AC-21-79MC11597

SRI Project PYU 8975

SRI International
333 Ravenswood Avenue
Menlo Park, California 94025
(415) 326-6200
TWX: 910-373-2046
Telex: 334 486

UNCLASSIFIED

SECURITY CLASSIFICATION OF THIS PAGE *(When Data Entered)*

REPORT DOCUMENTATION PAGE		READ INSTRUCTIONS BEFORE COMPLETING FORM
1. REPORT NUMBER	2. GOVT ACCESSION NO.	3. RECIPIENT'S CATALOG NUMBER
4. TITLE *(and Subtitle)* EXPERIMENTAL AND THEORETICAL STUDY OF HYDRAULIC FRACTURING IN IMPERMEABLE AND PERMEABLE MATERIALS		5. TYPE OF REPORT & PERIOD COVERED Final Report Sept 79 to Oct 81 6. PERFORMING ORG. REPORT NUMBER SRI Project PYU 8975
7. AUTHOR(s) M. B. Rubin Project Supervisor: A. L. Florence		8. CONTRACT OR GRANT NUMBER(s) AC-21-79MC11597
9. PERFORMING ORGANIZATION NAME AND ADDRESS SRI International 333 Ravenswood Avenue Menlo Park, CA 94025		10. PROGRAM ELEMENT, PROJECT, TASK AREA & WORK UNIT NUMBERS
11. CONTROLLING OFFICE NAME AND ADDRESS Department of Energy Morgantown Energy Technology Center Morgantown, West Virginia 26505		12. REPORT DATE October 1981 13. NUMBER OF PAGES 182
14. MONITORING AGENCY NAME & ADDRESS*(if different from Controlling Office)*		15. SECURITY CLASS *(of this report)* Unclassified 15a. DECLASSIFICATION/DOWNGRADING SCHEDULE
16. DISTRIBUTION STATEMENT *(of this Report)*		
17. DISTRIBUTION STATEMENT *(of the abstract entered in Block 20, if different from Report)*		
18. SUPPLEMENTARY NOTES		
19. KEY WORDS *(Continue on reverse side if necessary and identify by block number)* Hydraulic Fracture Impermeable Material Permeable Material Fluid Leak-Off		

20. ABSTRACT *(Continue on reverse side if necessary and identify by block number)*

Experiments were conducted to study hydraulic fracture propagation in impermeable and permeable materials. The complicating effects of fluid leak-off and proppant transport were separated by conducting experiments on an impermeable material without proppants, on a permeable material without proppants, and, finally, on the same permeable material with proppants.

Borehole pressure, pressure in the fracture, fracture width, and fracture length were measured in both impermeable and permeable experiments. In addition,

DD FORM 1 JAN 73 1473 EDITION OF 1 NOV 65 IS OBSOLETE

UNCLASSIFIED

SECURITY CLASSIFICATION OF THIS PAGE *(When Data Entered)*

the extent of fluid penetration into the permeable material was measured in the permeable experiments. It was observed that both the borehole pressure and the pressure gradient in the fracture were considerably larger in the experiments with proppants than in the experiments without proppants.

The results of the impermeable and permeable experiments were compared with the corresponding predictions of a solution developed here as well as those of other simple formulas for hydraulic fracture propagation. Although the predictions of the present solution are an improvement over those of the other simple solutions, future research is needed to reduce the discrepancy between theory and experiment. This discrepancy is attributed to the effect of fluid penetration on the fracture mechanics of the permeable medium.

SUMMARY AND CONCLUSIONS

Experiments were conducted to study hydraulic fracture propagation in impermeable and permeable materials. The main objective of this program was to provide quantitative experimental data for computer code development and verification. The complicating effects of fluid leak-off and proppant transport were separated by conducting experiments on an impermeable material without proppants, on a permeable material without proppants, and, finally, on the same permeable material with proppants.

The impermeable models were constructed of PMMA, and experiments were conducted to measure the borehole pressure, pressure in the fracture, fracture width, and fracture length as functions of time during fracture propagation. Using Dow Corning 200 silicone fluid (100,000 centistoke) as the fracturing fluid, we were able to produce quasi-static continuous fracture propagation.

The permeable models were constructed of hydrostone, and Dow Corning 200 silicone fluid (1,000 centistoke) was used as the fracturing fluid. In these experiments, we measured the extent of fluid penetration into the hydrostone as well as the borehole pressure, pressure in the fracture, fracture width, and fracture length as functions of time.

A flow-cycle treatment of the permeable model was simulated by intermittently pumping, relieving the borehole pressure, and repumping the model.

In the permeable experiments with proppants, a slurry of proppants was pumped into the borehole both with and without a pad volume of clear fluid preceding it. Both the borehole pressure and the pressure gradient in the fracture were considerably larger in the experiments with proppants than in the experiments without proppants.

The classical fluid leak-off model was reexamined, and another solution was developed to detemine the extent and width of a propagating vertical hydraulic fracture in an infinite permeable medium. In this solution, the flow velocity of fluid penetrating the formation is determined as part of the solution instead of being specified as it is in the classical fluid leak-off model. The closed-form solution obtained shows that the functional form of the flow velocity is significantly different from the form usually specified.

The results of the impermeable and permeable experiments were compared with the corresponding predictions of the solution developed here as well as those of other simple formulas for hydraulic fracture propagation. For the impermeable exeriments, the predictions of the present solution compared very well with the experimental data. However, for the permeable experiments, the present solution predicted values for the borehole pressure and fracture width that were much lower than those observed in the experiments. This discrepancy between theory and experiment is attributed to the effect of fluid penetration into the formation on the fracture mechanics of the permeable medium. Although the predictions of the present solution are an improvement over those of the other simple solutions, future research is required to modify the simple solutions and computer codes that analyze hydraulic fractures. This is because the common fracture mechanics models used in these solutions and codes neglect the effect of fluid penetration.

CONTENTS

ILLUSTRATIONS

ILLUSTRATIONS (continued)

ILLUSTRATIONS (continued)

ILLUSTRATIONS (continued)

ILLUSTRATIONS (continued)

ILLUSTRATIONS (continued)

Appendix B

ILLUSTRATIONS (continued)

TABLES

Appendix A

1. INTRODUCTION

1.1 Background Information

Hydraulic fracturing is a common technique used for enhancing the production of oil or gas from a well. In a hydraulic fracture treatment fluid is pumped down the borehole of the well at a sufficient rate of flow to fracture the rock formation containing the oil or gas. It is hoped that the productivity of the well will be increased by increasing the surface area of the formation that is in direct communication with the borehole.

In response to the in situ stresses in the formation, the fracture will tend to "heal" or close up when the pressure is relieved. Therefore, it is very common to mix solid particles, called proppants, with the fracturing fluid. Presumably, these proppants are carried by the fracturing fluid into the fracture. Then when the pressure is relieved in the borehole, the fracture closes and proppants are trapped between the fracture faces maintaining a residual fracture opening. Since the permeability of the proppant pack is generally much greater than the permeability of the rock formation, the flow of oil or gas from the surface area of the formation in contact with the proppant pack to the borehole is enhanced.

The size and location of the proppant pack that determines the residual opening of the fracture is controlled by the characteristics of the hydraulic fracture treatment used to stimulate the well. Since fluid leaks into the formation as the fracture propagates, the proppant concentration in the fracturing fluid and the mechanical properties (e.g., viscosity) of the slurry (mixture of proppants and fracturing fluid) are continually changing. Generally, a certain amount of clear fluid, called a pad volume, is pumped into the formation before the slurry of proppants is pumped in. The pad volume is used to help prevent the concentration of proppants near the fracture tip from increasing too rapidly.

Depending on the characteristics of the formation, it may be desirable to use more than one pad volume and more than one size proppant. However, to design a hydraulic fracturing treatment for a particular well, it is necessary to have a set of formulas or a computer code that can accurately predict the size and location of the proppant packs associated with a wide variety of fracturing treatments. Because of the increasing cost of hydraulic fracture treatments, it is becoming more important to understand the mechanisms that control hydraulic fracturing so that the complex stimulation treatments can be optimally designed for each well.

Because of in situ stresses and vertical layering of typical rock formations, many hydraulic fractures can be modeled as vertical fractures of limited vertical extent (see Figure 1). Even when the effects of proppants are neglected, the problem of propagating a vertical hydraulic fracture in a permeable material is quite complicated. This problem has been analyzed by many researchers and has been reviewed extensively in a monograph by Howard and Fast.[1] The classical solution was obtained by Carter[2] by assuming that the fracture width and fracturing pressure are both constant. To analyze fluid leak-off, Carter[2] specified the flow velocity to be inversely proportional to the square root of the time that a given location of the fracture is exposed to fracturing fluid, the proportionality constant being the fluid-loss coefficient. Others later reformulated the problem by relaxing some of the restrictions associated with the classical solution, but most of them who included fluid leak-off continued to specify the flow velocity in the form taken by Carter.[2] Broadly speaking, these researchers can be separated into two groups: those who assume that plane strain conditions exist in vertical planes perpendicular to the fracture plane and those who assume that plane strain conditions exist in horizontal planes. Perkins and Kern[3] and Nordgren[4] are included in the first group, and Khristianovic and Zheltov,[5] Geertsma and de Klerk[6] and Daneshy[7] are included in the second group. Those in the first group neglect the fracture mechanics of the fracture tip, whereas those in the

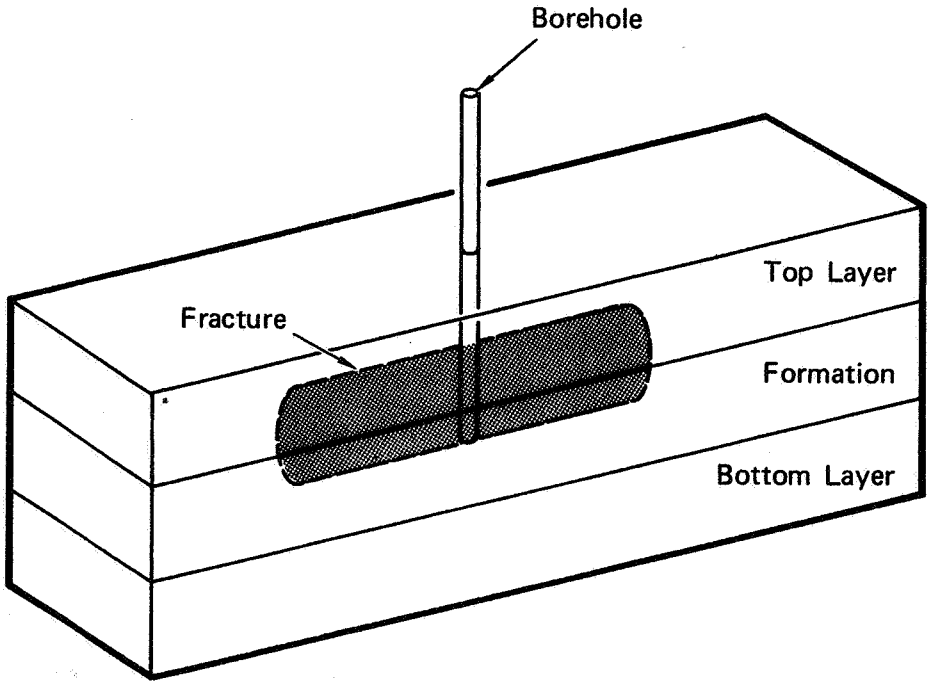

FIGURE 1 VERTICAL FRACTURE IN MODEL FORMATION

second group include it. These solutions have been compared by Geertsma and Haafkens.[8]

Those authors mentioned above who have included leak-off in their models have used the classical fluid leak-off model[2] and have specified the functional form of the flow velocity.* Recently, however, Hagoort, Weatherill, and Settari[9] have developed a computer program to model the propagation of waterflood-induced hydraulic fractures that does not use the classical leak-off model. Settari[10] has applied a similar computer program to study hydraulic fracture treatments in which the fluid leak-off is not as high as that associated with waterfloods.

In the present study, the classical fluid leak-off model is reexamined (see Appendix A), and the problem of determining the extent and width of a propagating vertical hydraulic fracture in an infinite medium is solved, assuming that plane strain conditions exist in horizontal planes. The time dependent fracture width and fluid pressure are determined by assuming that the fracture is uniformly pressurized and that linear elastic fracture mechanics applies. The formation is taken to be permeable in the direction normal to the fracture plane, and the flow velocity of fluid penetrating the formation is determined as part of the solution instead of being specified as it is in the classical fluid leak-off model.[2] A closed-form solution is obtained that shows that the functional form of the flow velocity is significantly different from the form usually specified. Furthermore, this solution is extremely easy to use for designing hydraulic fracture treatments.

Many researchers have developed computer programs to predict the size and location of the proppant pack that maintains the residual fracture opening. In particular, we note the work of van Domselaar and Visser,[11] Novotny,[12] and Daneshy.[13] Novotny's[12] work emphasizes the importance of accurately modeling proppant settling during fracture

---

*It is not clear exactly what form the flow velocity takes in Daneshy's[7] computer program.

closure. Also the prediction of the size and location of the proppant pack is strongly influenced by the particular equations used to model the settling velocity. For this reason, Clark and Quadir[14] have recently provided a critical review of particle settling velocity equations.

The various computer programs used to predict the results of specific hydraulic fracturing treatments cannot be verified by comparing theoretical predictions with measurements taken in the field alone because many of the critical parameters needed to verify the codes (e.g., fracture length and the residual propped fracture opening) cannot be easily measured in the field. Therefore, the results of laboratory experiments are needed to verify the codes. Examples of such experiments are those of Haimson and Fairhurst,[15] who measured the value of the critical pressure for fracture initiation in a porous-permeable material (hydrostone), the experiments of Novotny[12] and Sievert et al., who measured proppant settling velocities for flow between vertical, parallel, impermeable walls and the experiments described here.

1.2 Proppant Transport-Fracture Mechanics Interaction Study

Few, if any, experiments have been conducted to measure borehole pressure, pressure in the fracture, fracture width, and fracture length during propagation of a hydraulic fracture in impermeable and permeable materials. Therefore, SRI proposed to the Department of Energy the interactive laboratory and computational program shown in Figure 2.

The main objectives of the program are to:

(1) Provide quantitative experimental data needed for computer code development and verification.

(2) Verify computational predictions of the laboratory experiments.

(3) Verify computational predictions for a specific well stimulation treatment in a field test.

The program shown in Figure 2 consists of a series of experimental and computational tasks required to meet these objectives. The initial

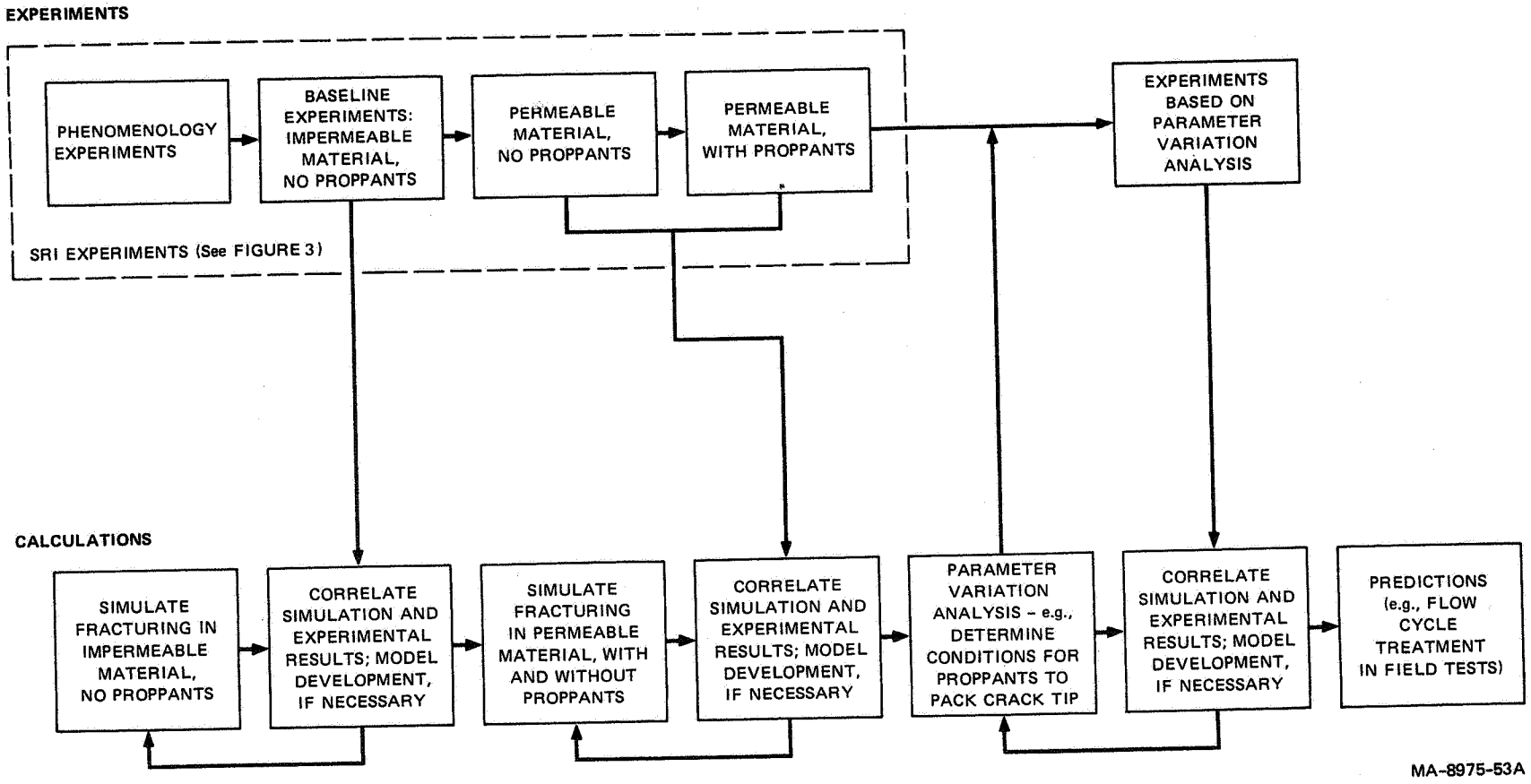

FIGURE 2 PROPPANT TRANSPORT-FRACTURE MECHANICS INTERACTION STUDY

experimental tasks (performed by SRI and discussed in more detail later) provide the basic measurements necessary to verify computational predictions of hydraulic fracture treatments in both an impermeable and a permeable material. At each stage, the experimental data must be replicated by computer code simulations of the experiments and numerical model development proceeds as necessary.

Once confidence in the computer code predictions for laboratory experiments is established, the code can be used to perform a parameter variation analysis for a range of conditions of interest in field tests (e.g., the conditions required for proppants to pack the fracture tip). Then laboratory, though not necessarily scaled,* experiments can be designed to reproduce these conditions and verify the code predictions or provide a basis for code modification.

After some cycle of iterations between experiments and computations is performed, the computational code will be verified, at least for the conditions of interest in particular field tests. At that point, predictions about specific field experiments or optimization of fracture design in a field experiment can be made with some degree of confidence.

The computational effort was to be performed by another agency** under separate contract, and the laboratory effort was to be performed by SRI. Because the computational effort was not funded, the second and third objectives could not be met, and the interactive experimental-computational aspects of the program were eliminated. However, the first objective was met by performing the experiments enclosed by the broken lines in Figure 2.

The experimental program conducted by SRI is outlined in Figure 2 and is shown in greater detail in Figure 3. The ultimate goal of this

---

*The laboratory experiments will not necessary be scaled because parameters such as gravity and fracture toughness do not scale easily.

**University of Ohio by Professor Sunder Advani.

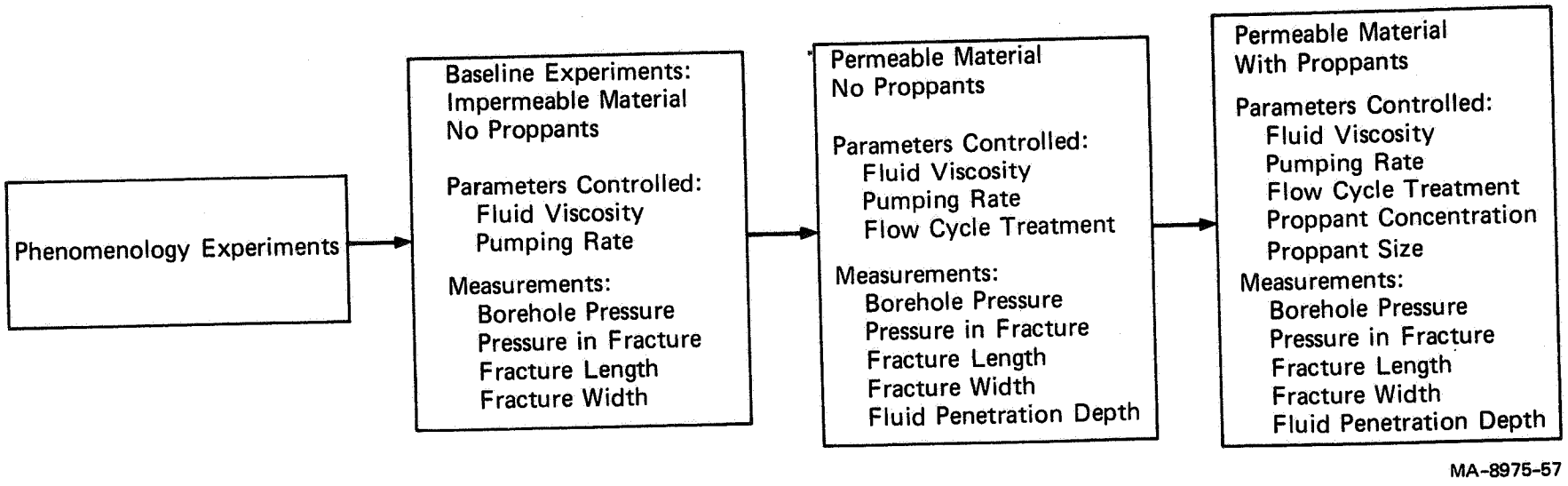

FIGURE 3 SRI EXPERIMENTAL PROGRAM FOR PROPPANT TRANSPORT-FRACTURE MECHANICS INTERACTION STUDY OF THE FLOW-CYCLE TREATMENT PROCESS

program was to obtain experimental information about proppant transport during hydraulic fracture propagation in a permeable material. The phenomenology experiments, described in Appendix B, were conducted to obtain preliminary information about proppant transport during hydraulic fracture propagation. Because the phenomenology experiments demonstrated that fluid leak-off was required for significant proppant transport, no quantitative data were obained from experiments with proppants in an impermeable material. These experiments also showed that we needed to use a highly viscous fluid (100,000 centistoke) as a fracturing fluid to obtain continuous quasi-static fracture propagation in the impermeable models.

A series of "baseline" experiments were conducted to determine the fracture conditions and fluid pressure in an impermeable material polymethylmethacrylate (PMMA) without proppants. These experiments provided information about the interaction between the fluid flow and the fracture mechanics of the formation without the complicating effects of fluid leak-off and the presence of proppants. Fluid viscosity and pumping rate were controlled and borehole pressure, pressure in the fracture, fracture length, and fracture width were measured as functions of time during fracture propagation.

To separate the effects of fluid leak-off and proppant transport, two sets of experiments were performed in a permeable material (hydrostone). In the first set, no proppants were used, and the role of fluid leak-off on fracture growth was determined. In the second set, proppants were mixed with the fluid, and the effect of the proppants on fracture growth was determined using this same permeable material. In both sets of experiments, we also controlled the flow-cycle treatment by intermittently pumping, relieving the borehole pressure, and repumping the models. The depth of fluid penetration into the formation was also measured.

The experiments on an impermeable material are described in Section 2, and the experiments on a permeable material are described in Section 3. The theoretical developments that were used to design and

interpret the experiments on a permeable material were written as a paper, titled "On Fluid Leak-Off During Propagation of a Vertical Hydraulic Fracture." A copy of this paper, which has been submitted for publication, is included in Appendix A. Appendix B describes the phenomenology experiments, and Appendix C describes an investigation of the conditions that exist at the intersection of the fracture with the interface of the PMMA layers in the impermeable models.

2. IMPERMEABLE EXPERIMENTS

2.1 Experimental Procedures and Setup

The pump system for the impermeable experiments consists of a hand pump for prefracturing the models, a motor pump* for the main fracture of the models, and a separation chamber to separate the water in the pump system from the highly viscous fracturing fluid. This pump system is shown schematically in Figure 4. For a constant volumetric pumping rate, the fracture in the impermeable models propagated in two phases. In the first phase, the fracture propagation was driven by the release of the stored energy in the pumping fluid** and the compressibility of the fluid cannot be neglected. In the second phase, the fracture propagation was driven by the pump, and the compressibility of the fluid can be neglected. Because the main objective of this program was to obtain quantitative experimental data needed for computer code development and verification, we decided to focus attention on the second phase of fracture propagation, which is more representative of field conditions.

To minimize the extent of the first phase of fracture propagation, we fractured the impermeable models in two stages: prefracture followed by main fracture. Air was evacuated from the pumping fluid using a vacuum pump, and the valves to the vacuum pump and water reservoir (see Figure 4) were closed to create a closed pump system. For the prefracture the valve above the hand pump (see Figure 4) was closed, and the hand pump was used to pressurize the fluid until the model fractured.

---

*The hand pump and motor pump were made by High Pressure Equipment Company, Inc., 1222 Linden Avenue, Erie, Pennsylvania.

**By pumping fluid, we mean the fluid that is pressurized in the closed pumping system.

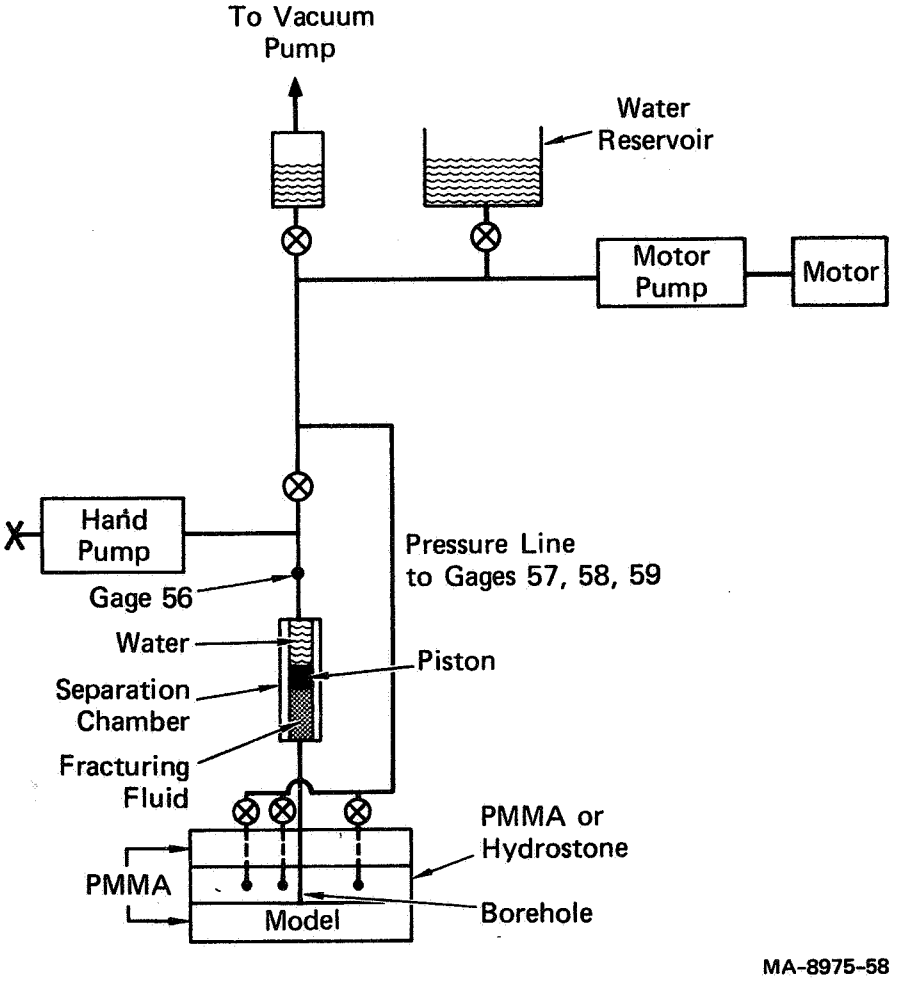

FIGURE 4 SCHEMATIC OF PUMP SYSTEM

(The symbol ⊗ stands for a valve.)

This had the effect of reducing the final length of the prefracture by reducing the volume of fluid being pressurized during the prefracture and hence reducing the stored strain energy in the pumping fluid. After the prefracture was complete, the valve above the hand pump (see Figure 4) was opened, and the fracture was brought into communication with the main motor driven pump system. The main fracture then proceeded by pumping with the motor pump at a constant volumetric flow rate of 73.2 mm^3/s.

The impermeable models were constructed by bonding three layers of PMMA together with chloroform. This construction technique was used to vertically contain the fracture in the middle PMMA layer by creating weak interfaces at the top and bottom of the middle layer. Figure 5 shows the dimensions of the impermeable models. For future reference, we note that models 25 and 27 were slightly bigger than model 28. A borehole 6.35 mm in diameter was drilled through the top layer into the middle layer, and vertical scratches 0.56 mm deep were placed on opposite sides of the borehole in the middle layer to initiate the fracture along the length of the model (x-z plane in Figure 6). The section of the borehole in the top layer was then cased with a steel tube 6.35 mm OD and 3.18 mm ID. The steel casing extended slightly into the middle layer to eliminate problems with debonding the top interface.

A Setra* gage (model 204E, 0 to 5000 psi) was used to measure the pressure outside the borehole (see Gage 56 in Figure 6). Setra gages (model 204E, 0 to 1000 psi) were also used to measure the pressure at three locations in the fracture (see Gages 57, 58, and 59 in Figure 6). These Setra gages were chosen because of the accuracy needed to measure the gage pressure** in the fracture and the pressure differences between

---

*These pressure gages were made by Setra Systems, Inc., 1 Strathmore Rd., Natick, MA.

**Although these Setra gages are absolute pressure gages, we referenced all gage readings to their readings in atmospheric pressure.

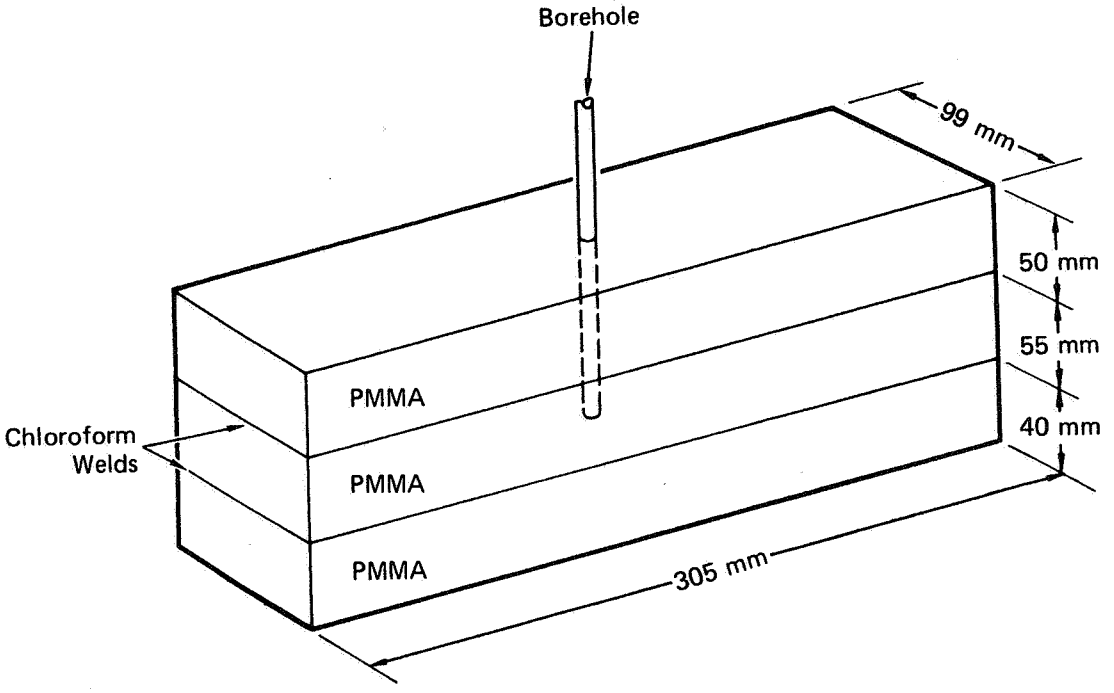

(a) MODELS 25 AND 27

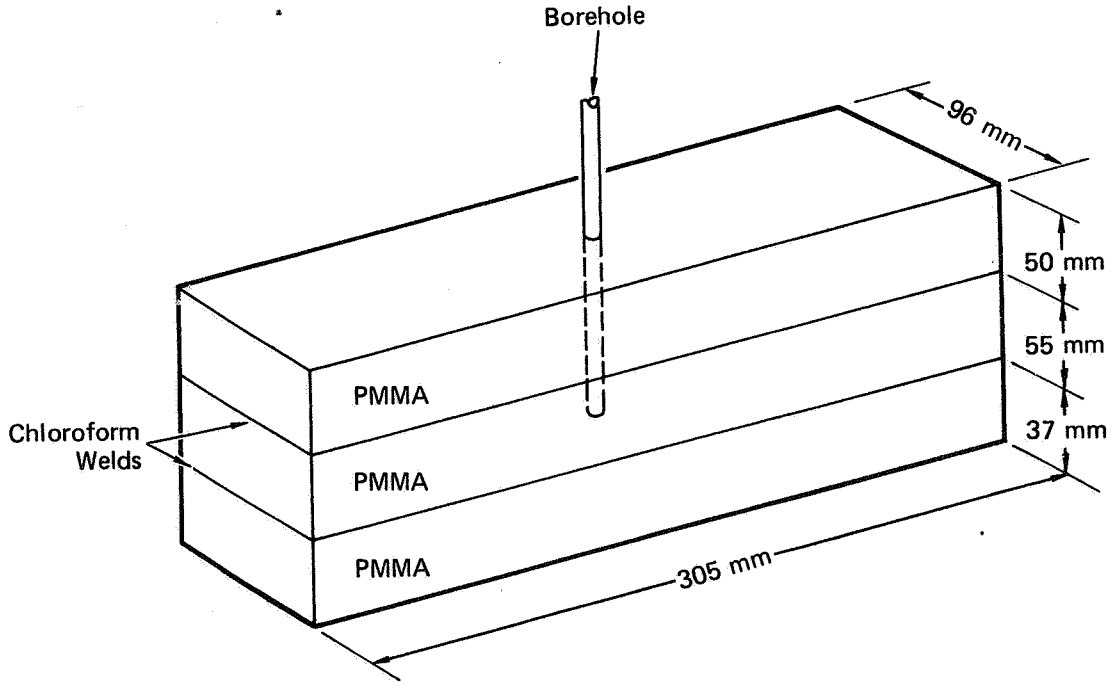

(b) MODEL 28

MA-8975-59

FIGURE 5 DIMENSIONS OF IMPERMEABLE MODELS

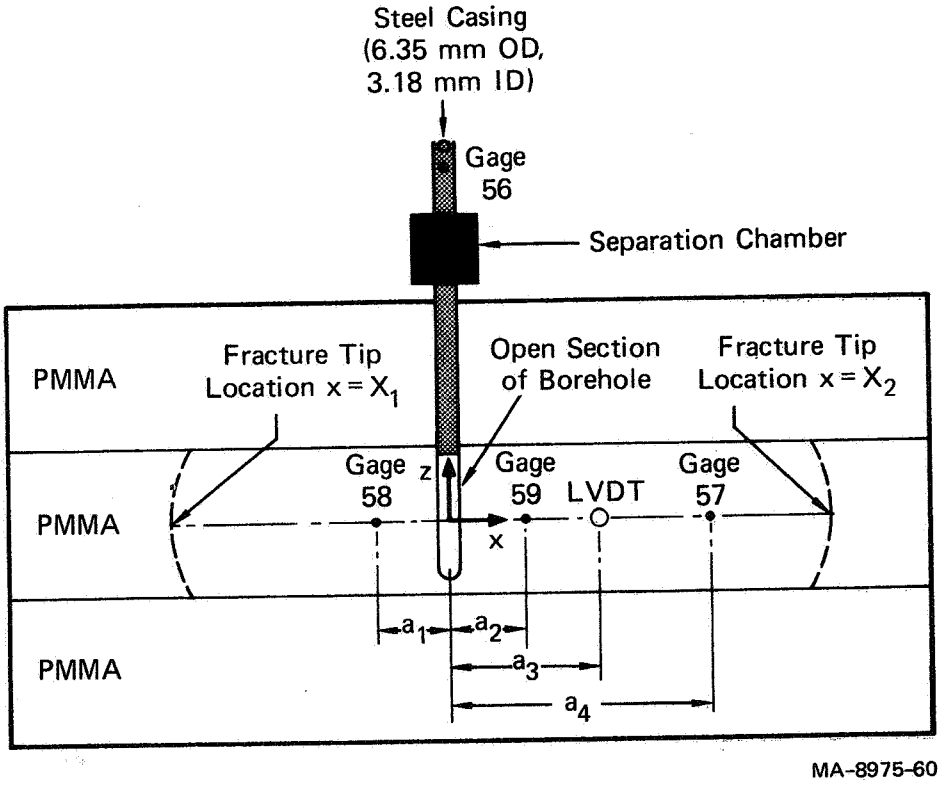

FIGURE 6 LOCATIONS OF PRESSURE GAGES 56, 57, 58, AND 59, LVDT, AND FRACTURE TIPS RELATIVE TO THE BOREHOLE IN THE IMPERMEABLE MODELS

points in the fracture. These gages have a precision of ± 0.11% of full range. Figure 7 is a sketch of the access holes used to measure the pressure in the fracture in the impermeable models. These access holes were filled with fracturing fluid, then the gages were attached and prepressurized slightly to prevent trapped air from influencing the pressure measurements. Table 1 summarizes the values of the parameters a_1, a_2, a_3, and a_4 (see Figure 6) describing the gage locations in the impermeable models.

Table 1

VALUES OF PARAMETERS DESCRIBING GAGE LOCATIONS IN IMPERMEABLE MODELS[A]

Parameter	Models 25 and 27	Model 28
a_1 (mm)	15.0	15.0
a_2 (mm)	15.0	15.0
a_3 (mm)	28.5	28.5
a_4 (mm)	71.0	41.0

[a] see Figure 6.

A linear variable differential transducer* (LVDT) was used to measure the fracture width at one location. Figure 6 shows the location of the LVDT, and Figure 8 is a sketch of the LVDT mounting used in the impermeable models. Basically, the LVDT was used to measure the change in the separation of two points that were 35 mm apart in the unstressed,

*The LVDT (model PCA-220-020, ± 0.020 in.) and signal conditioner (model CAS-025) were manufactured by Schaevitz Engineering, P. O. Box 505, Camden, N.J. 08101.

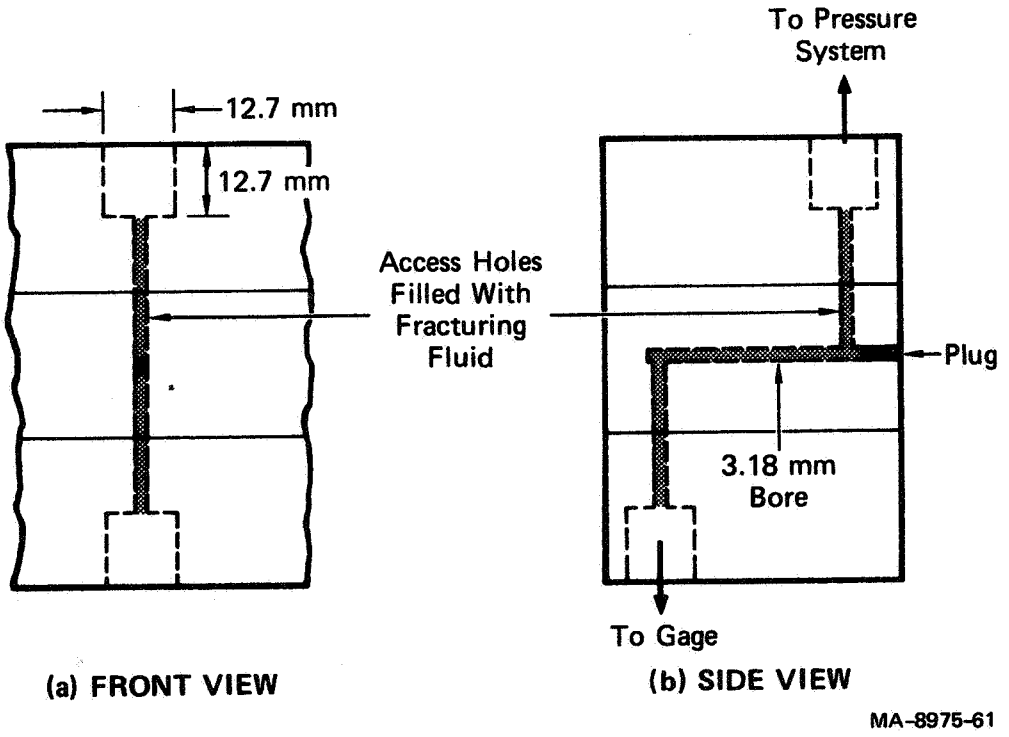

FIGURE 7 SKETCH OF ACCESS HOLES USED TO MEASURE PRESSURE IN THE FRACTURE IN THE IMPERMEABLE MODELS

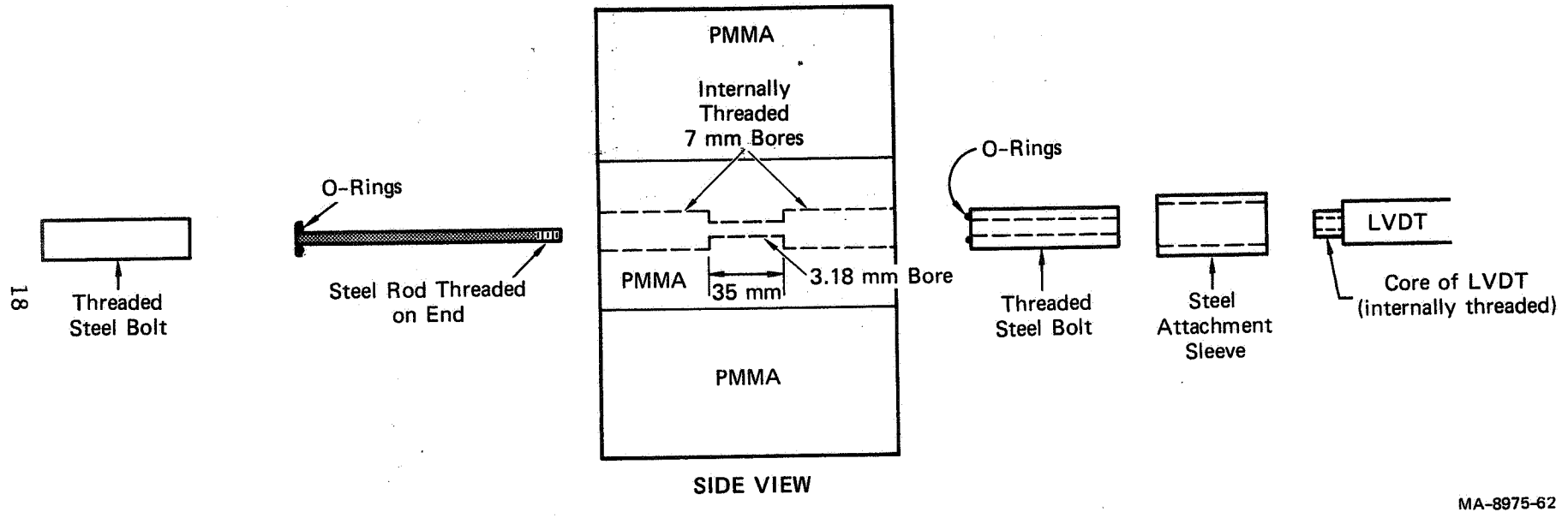

FIGURE 8 SKETCH OF LVDT MOUNTING USED FOR IMPERMEABLE MODELS

unfractured model. The 35 mm gap, which represents the active length of the fracture width gage, was required because we could not accurately predict the location of the fracture surface at distances from the borehole since the fracture curved as it propagated instead of propagating as a plane surface.

The LVDT and associated electronics were calibrated to within $\pm$ 2.5 μm. However, additional errors are introduced when the LVDT is used as a fracture width gage. In particular, when the fracture passes through the active element of the fracture width gage, the material in the 35-mm gap (see Figure 8) will be in a state of compression so the fracture width will be greater than the value recorded by the gage. The magnitude of this error is directly proportional to the pressure in the fracture and is estimated to be less than* 21 μm during the main fracture of the impermeable models.

Both the prefracture and main fracture of the impermeable models were photographed at 24 fps (frames per second) using a Locam motion picture camera. Back lighting was used to illuminate the models.

All gages were recorded on Nicholet scopes (model 2090-3) that were syncronized with the films. The digitizing unit for time during both the prefracture and the main fracture was 0.05 s. The digitizing units for the pressure gages and LVDT are summarized in Table 2. Also included in Table 2 are the values to within which the gages and associated electronics could be calibrated. The RMS precision of each gage was calculated by taking the square root of the sum of the squares of the digitizing unit and the calibration value. These RMS precision

---

*The strain ε in the PMMA is less than p/E where p is the pressure in the fracture and E = 3.28 GPa is Young's modulus. Thus, the error e in the fracture width is less than (p/E) x 35 mm. During the main fracture p is less than about 2 MPa so e is less than (2/3.28) (35) = 21 μm.

values may be used to place error bounds on the quantitative measurements reported later. As noted above, the fracture width measurement in the impermeable experiments underestimates the actual fracture width by less than 21 μm.

Table 2

GAGE PRECISION VALUES FOR
IMPERMEABLE AND PERMEABLE EXPERIMENTS

Gage	Digitizing Unit	Calibrated to Within	RMS Precision
56 (MPa)	0.027	± 0.034	± 0.04
57 (MPa)	0.0055	± 0.0069	± 0.009
58 (MPa)	0.0055	± 0.0069	± 0.009
59 (MPa)	0.0058	± 0.0069	± 0.009
LVDT (μm)	0.5	± 2.5	± 3

Recall that the pressure recorded by Gage 56 was the pressure outside the borehole (see Figure 6). To determine the pressure P_b in the borehole, we measured the pressure drop between the location of Gage 56 and the borehole while pumping the fracturing fluid through the separation chamber and the steel casing into the atmosphere. Figure 9 shows the pressure recorded by Gage 56 during this experiment. The borehole pressure P_b was determined by subtracting the average value (0.38 MPa) of the flat section of the record in Figure 9 from the pressure recorded by Gage 56. The steep pressure rise near the end of the record in Figure 9 is associated with the piston hitting the bottom of the separation chamber.

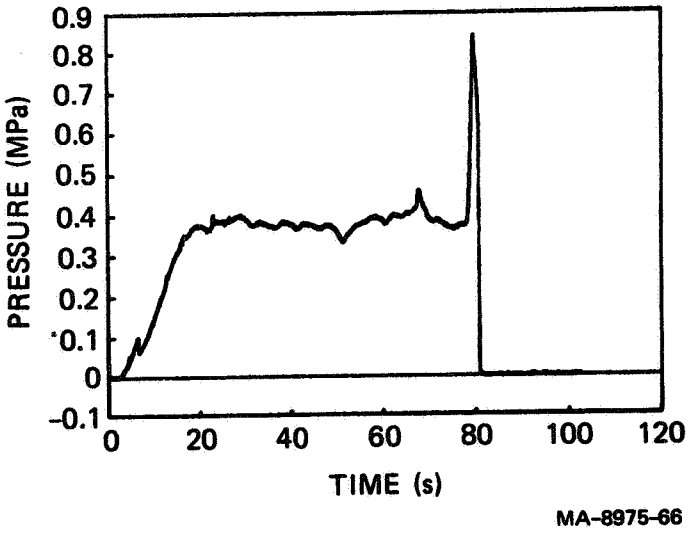

FIGURE 9 PRESSURE DROP ACROSS SEPARATION CHAMBER USED IN IMPERMEABLE EXPERIMENTS

(100,000-centistoke fluid)

The fracture tip locations X_1 and X_2 (see Figure 6) were determined by digitizing the films on a Telereadex.* The error in the values of X_1 and X_2 is estimated to be $\pm$ 2 mm. The extent of fluid penetration into the fracture could be determined from the films, and the fluid front was slightly curved. In all cases, we identified the fracture tip locations with the intersection of the curved fluid front with the x axis (see Figure 6).

The mass density ρ, Young's modulus E, and Poisson's ratio ν of PMMA have been determined using the data of Reference 17 and the fracture toughness K_{Ic} of PMMA is taken from Reference 18. These material properties are summarized below:

MATERIAL PROPERTIES OF PMMA

Density	$\rho = 1.185\ g \cdot m\ell^{-1}$
Young's modulus	$E = 3.28$ GPa
Poisson's ratio	$\nu = 0.367$
Fracture toughness	$K_{Ic} = 1.20\ MPa \cdot m^{1/2}$

The fracturing fluid used in the impermeable experiments was a Dow Corning** 200 silicone fluid with a kinematic viscosity of 100,000 centistokes. The density ρ and viscosity μ of this fluid at 25°C, as reported by Dow Corning were as follows:

---

*The Telereadex (Type 29E-29) made by Whittaker Corporation, Electronics Division, 12838 Saticoy Street, North Hollywood, California, 91605 was used in conjunction with a Graphics Tablet (Model 4956) made by Tektronix, Inc., P. O. Box 500, Beaverton, Oregon 97077.

**The Silicone fluid was made by Dow Corning Corporation, Midland, Michigan 48640.

MATERIAL PROPERTIES OF 100,000 CENTISTOKE FLUID

Density	$\rho = 0.977\ g \cdot m\ell^{-1}$
Viscosity	$\mu = 97{,}700$ cp

2.2 Main Experimental Results

In this section, the results of Experiments 25, 27, and 28 which used models 25, 27, and 28, respectively, are summarized. Figures 10 through 15, 16 through 21, 22 through 27, and Tables 3, 4, and 5 correspond to Experiments 25, 27, and 28, respectively.

Figures 10(a), 16(a), and 22(a) show Gage 56 during the prefracture. The fracture initiation pressure recorded by Gage 56 was 30.88 MPa, 27.92 MPa, and 22.53 MPa for models 25, 27, and 28, respectively. Figures 10(b), 16(b), and 22(b) show the pressures in Gages 56, 57, and 59 and Figures 10(c), 16(c), and 22(c) show the fracture width recorded by the LVDT. During the prefracture, the fracture engulfed Gage 59 but not Gage 57, which was located farther from the borehole than Gage 59. In Experiments 25 and 27, the prefracture engulfed the LVDT, but in Experiment 28, the fracture tip stopped propagating just before reaching the LVDT. Therefore, the LVDT record in Figure 22(c) is a measurement of the strain in the block instead of the fracture width. The symmetry of the prefracture is exhibited by Figures 11, 17, and 23, which compare the pressure records from Gages 58 and 59 that are located equidistant from the borehole and on opposite sides of it.

The pressure in Gage 56, the borehole pressure P_b, and the pressures at different locations in the fracture (Gages 57 and 59), recorded during the main fracture, are shown in Figures 12(a), 18(a), and 24(a). These figures show the pressure gradient in the fracture as a function of time. The late-time steep rise in the Gage 56 pressure record in Figure 24(a) and to a lesser extent in Figures 12(a) and 18(a) corresponds to the piston hitting the bottom of the separation chamber. Therefore, the records beyond this point are of no value. The fact that the pressure records in Gages 57 and 59 drop when the piston bottoms out

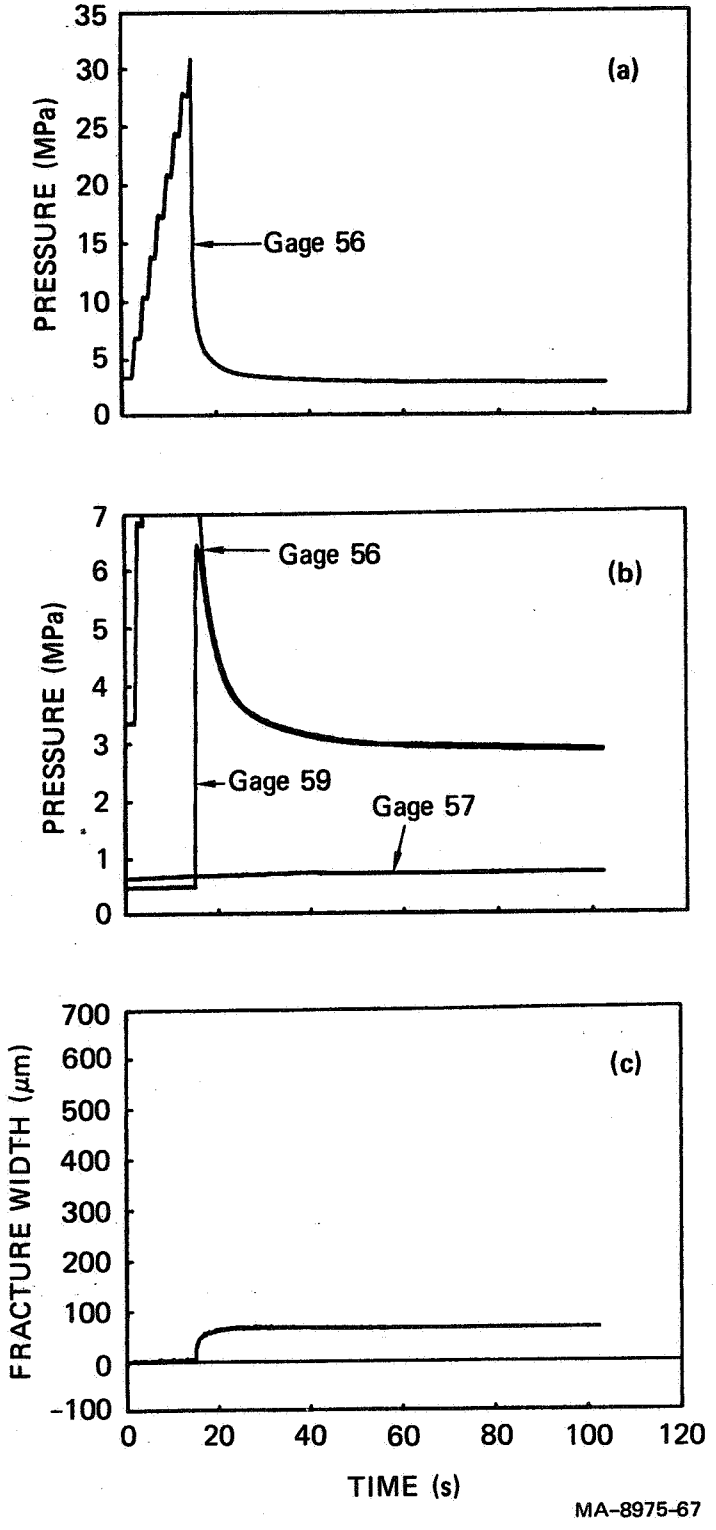

FIGURE 10 PREFRACTURE OF MODEL 25; (a) PRESSURE IN GAGE 56; (b) PRESSURES IN GAGES 56, 57, AND 59; (c) FRACTURE WIDTH

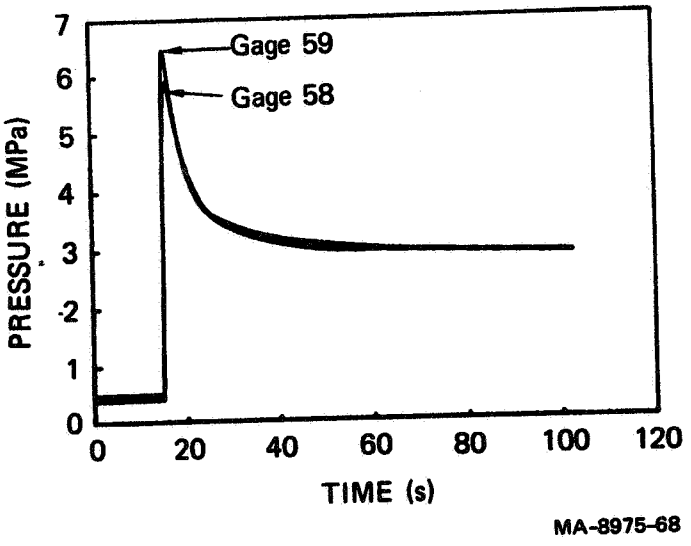

FIGURE 11 PRESSURES IN GAGES 58 AND 59 DURING THE PREFRACTURE OF MODEL 25

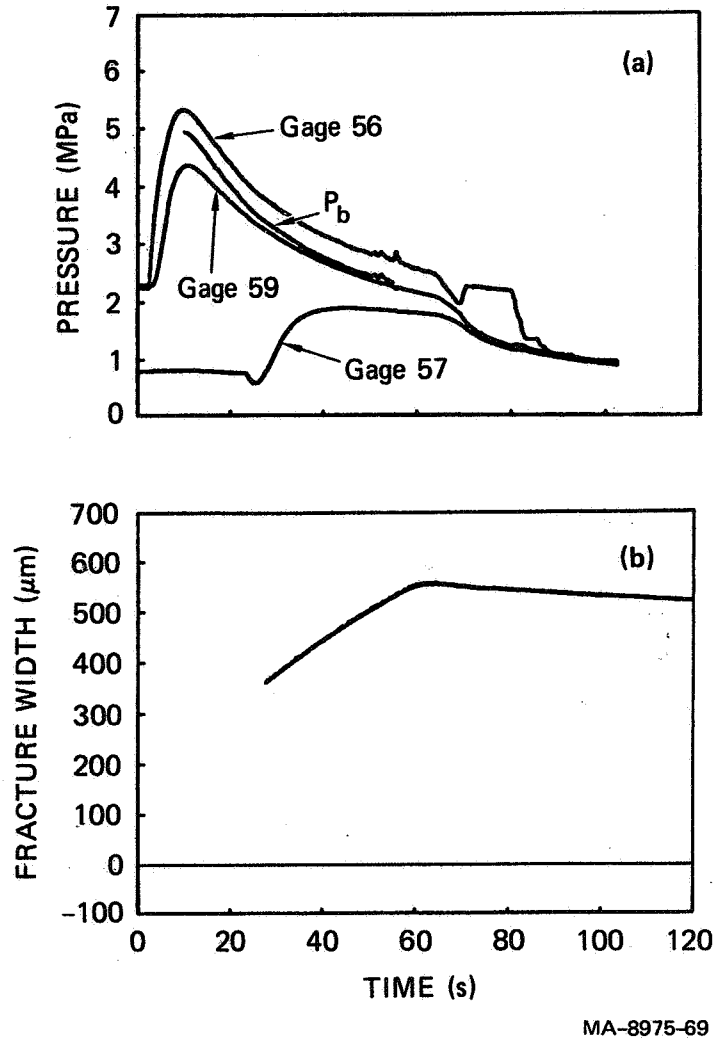

FIGURE 12 MAIN FRACTURE OF MODEL 25: (a) BOREHOLE PRESSURE P_b AND PRESSURES IN GAGES 56, 57, AND 59; (b) FRACTURE WIDTH

The time has been shifted in record (b) because the scope did not trigger properly.

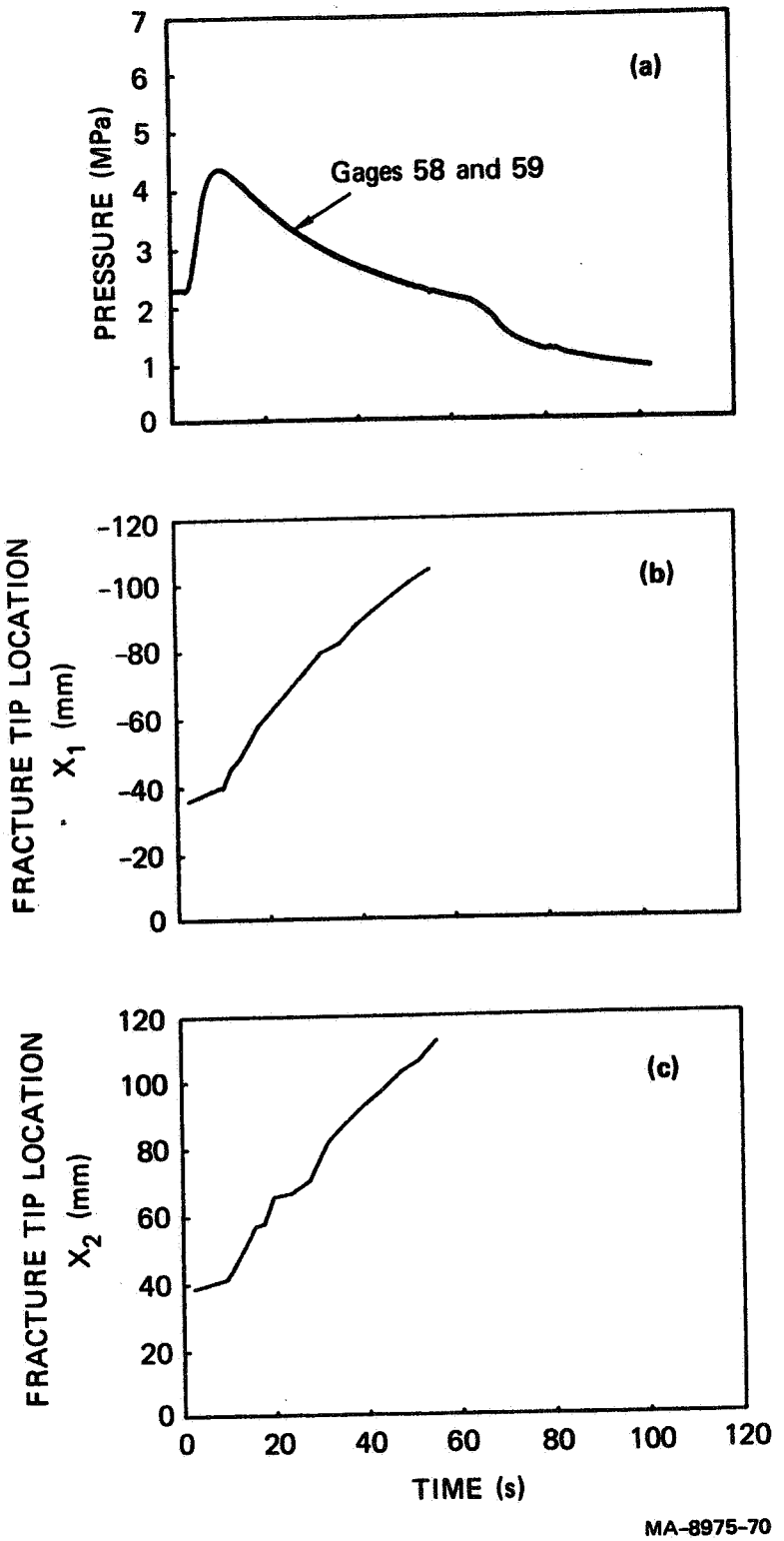

FIGURE 13 MAIN FRACTURE OF MODEL 25: (a) PRESSURES IN GAGES 58 AND 59; (b) FRACTURE TIP LOCATION X_1; (c) FRACTURE TIP LOCATION X_2

Table 3

QUANTITATIVE DATA TAKEN AT SEVERAL TIMES DURING THE MAIN FRACTURE OF MODEL 25[a] (pumping started at t = 2.45 s)

Time (s)	P_b (MPa)	Gage 56 (MPa)	Gage 57 (MPa)	Gage 58 (MPa)	Gage 59 (MPa)	LVDT (μm)	X_1 (mm)	X_2 (mm)	ℓ (mm)
2.45	-	2.26	0.797	2.293	2.295	--	-36	39	37
10.05	4.93	5.31	0.808	4.354	4.357	--	-40	42	41
13.80	4.65	5.03	0.780	4.229	4.220	--	-48	51	50
17.75	4.24	4.62	0.783	3.917	3.903	--	-58	58	58
23.70	3.68	4.06	0.719	3.496	3.476	--	-67	67	67
27.65	3.39	3.77	0.777	3.254	3.237	--	-73	71	72
31.60	3.16	3.54	1.424	3.053	3.036	--	-80	82	81
39.50	2.80	3.18	1.858	2.722	2.705	--	-88	93	90
47.35	2.51	2.89	1.889	2.471	2.457	--	-97	103	100
55.25	2.38	2.76	1.841	2.248	2.242	--	-104	112	108

[a]For error estimates see Table 2 and the discussion in section 2.1.

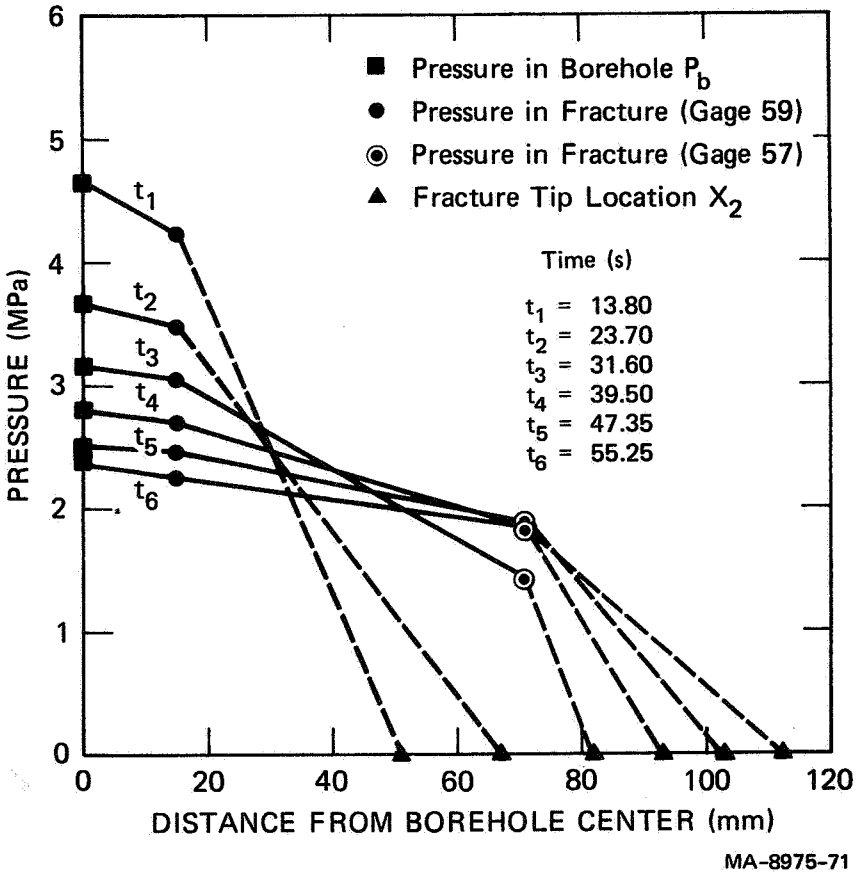

FIGURE 14 PRESSURE DISTRIBUTIONS AT SEVERAL TIMES DURING THE MAIN FRACTURE OF MODEL 25

Pumping started at t = 2.45 s.

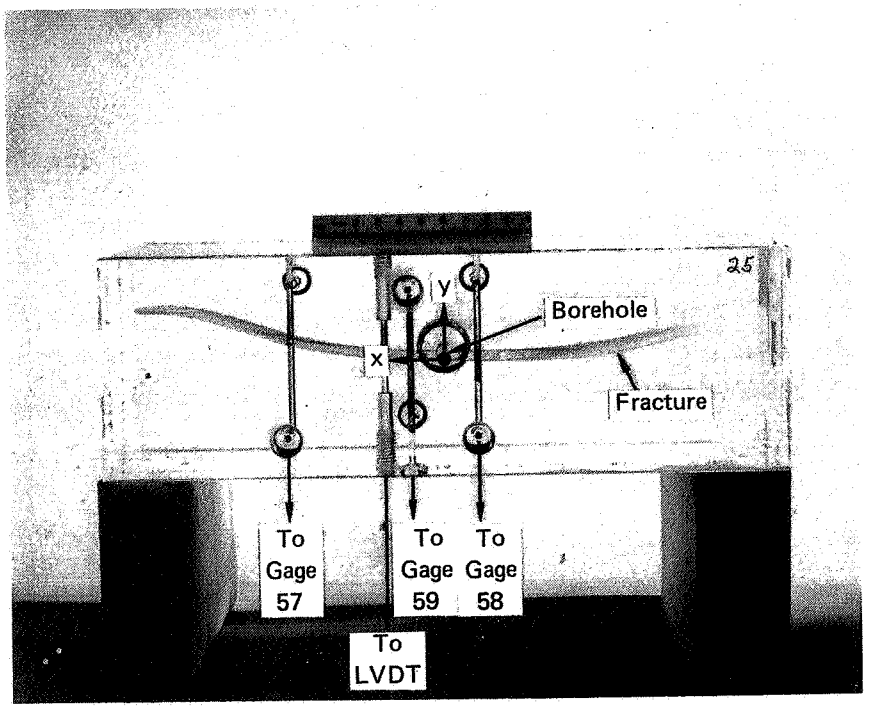

MP-8975-94

FIGURE 15 PHOTOGRAPH OF THE FRACTURE SURFACE IN MODEL 25
(viewed from the bottom)

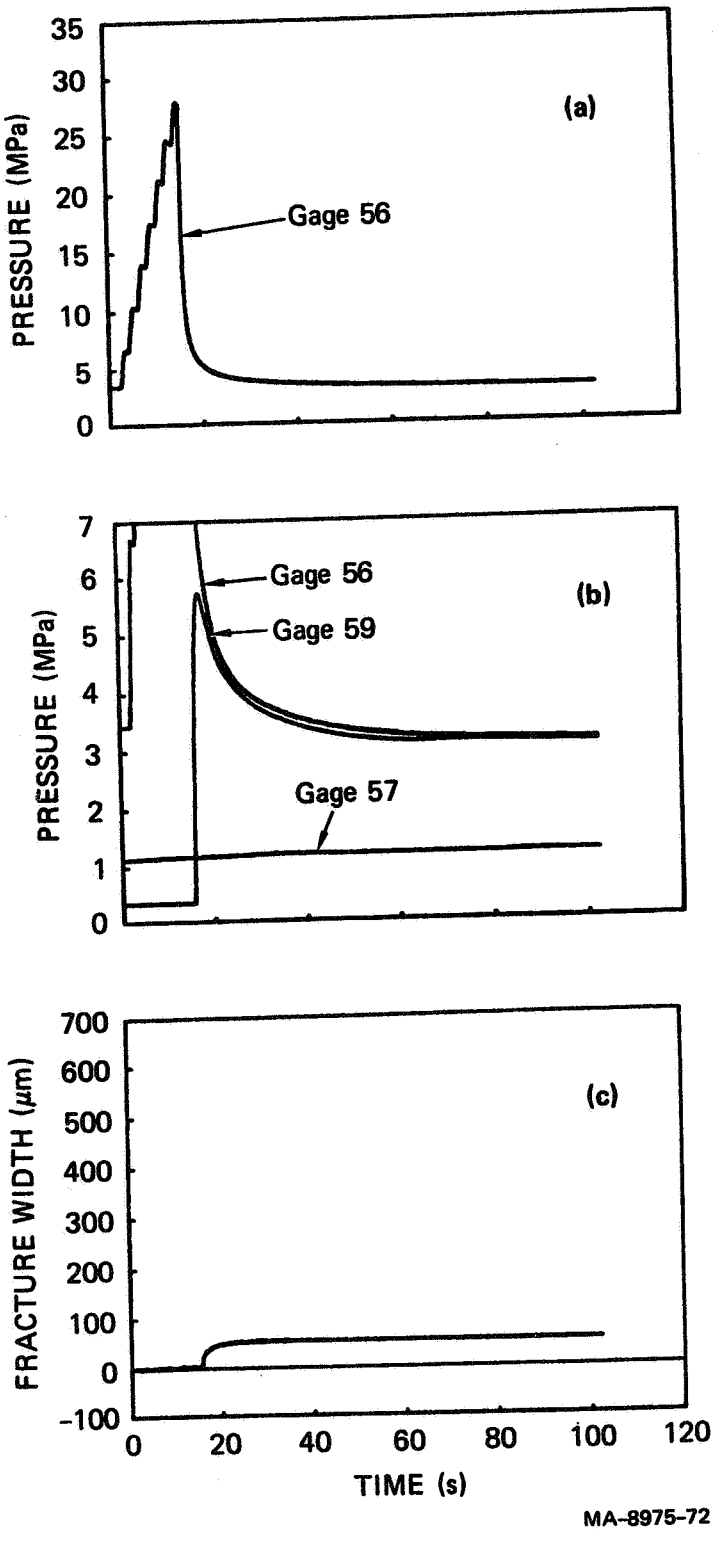

FIGURE 16 PREFRACTURE OF MODEL 27: (a) PRESSURE IN GAGE 56; (b) PRESSURES IN GAGES 56, 57, AND 59; (c) FRACTURE WIDTH

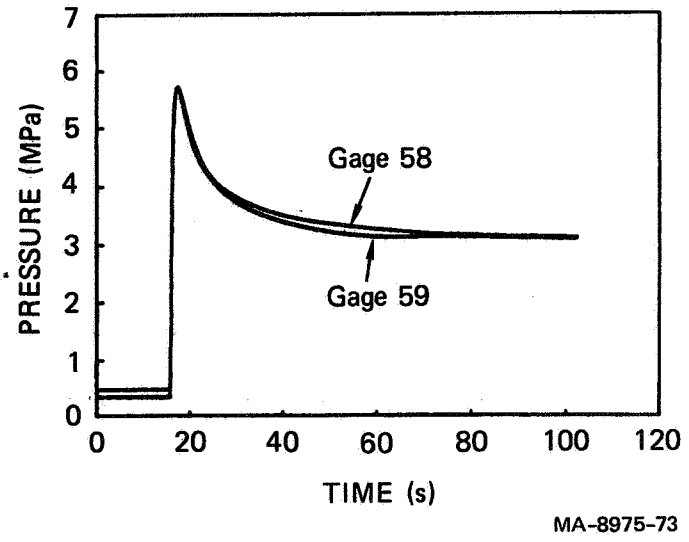

FIGURE 17 PRESSURES IN GAGES 58 AND 59 DURING THE PREFRACTURE OF MODEL 27

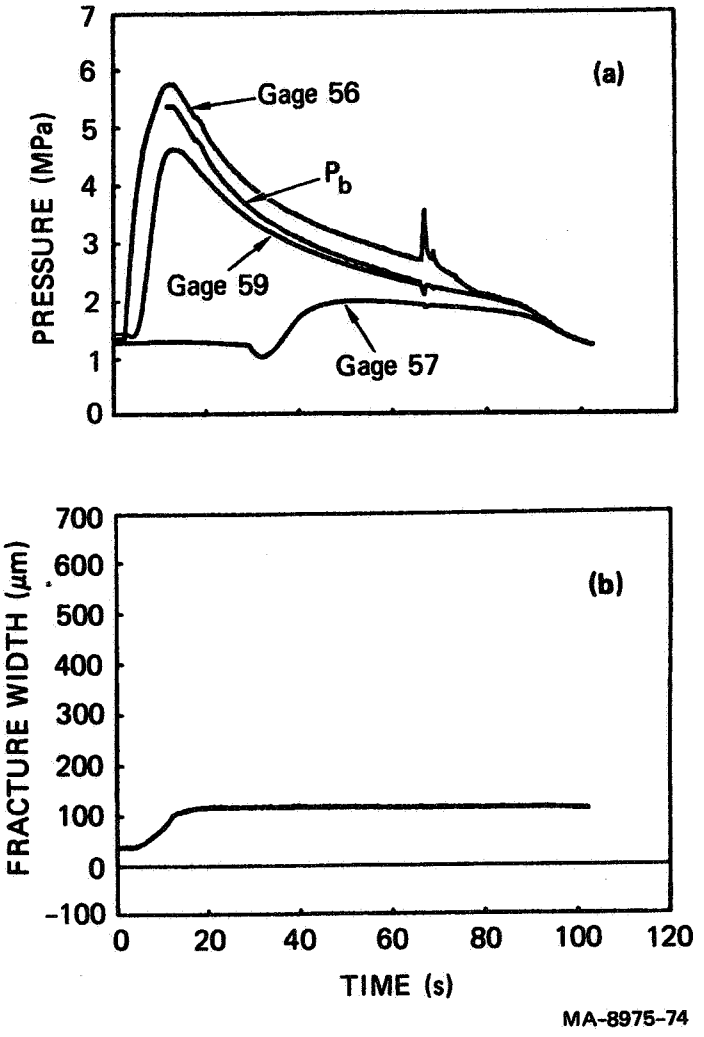

FIGURE 18 MAIN FRACTURE OF MODEL 27: (a) BOREHOLE PRESSURE P_b AND PRESSURES IN GAGES 56, 57, AND 59: (b) FRACTURE WIDTH

The record in (b) indicates that the fracture width gage broke.

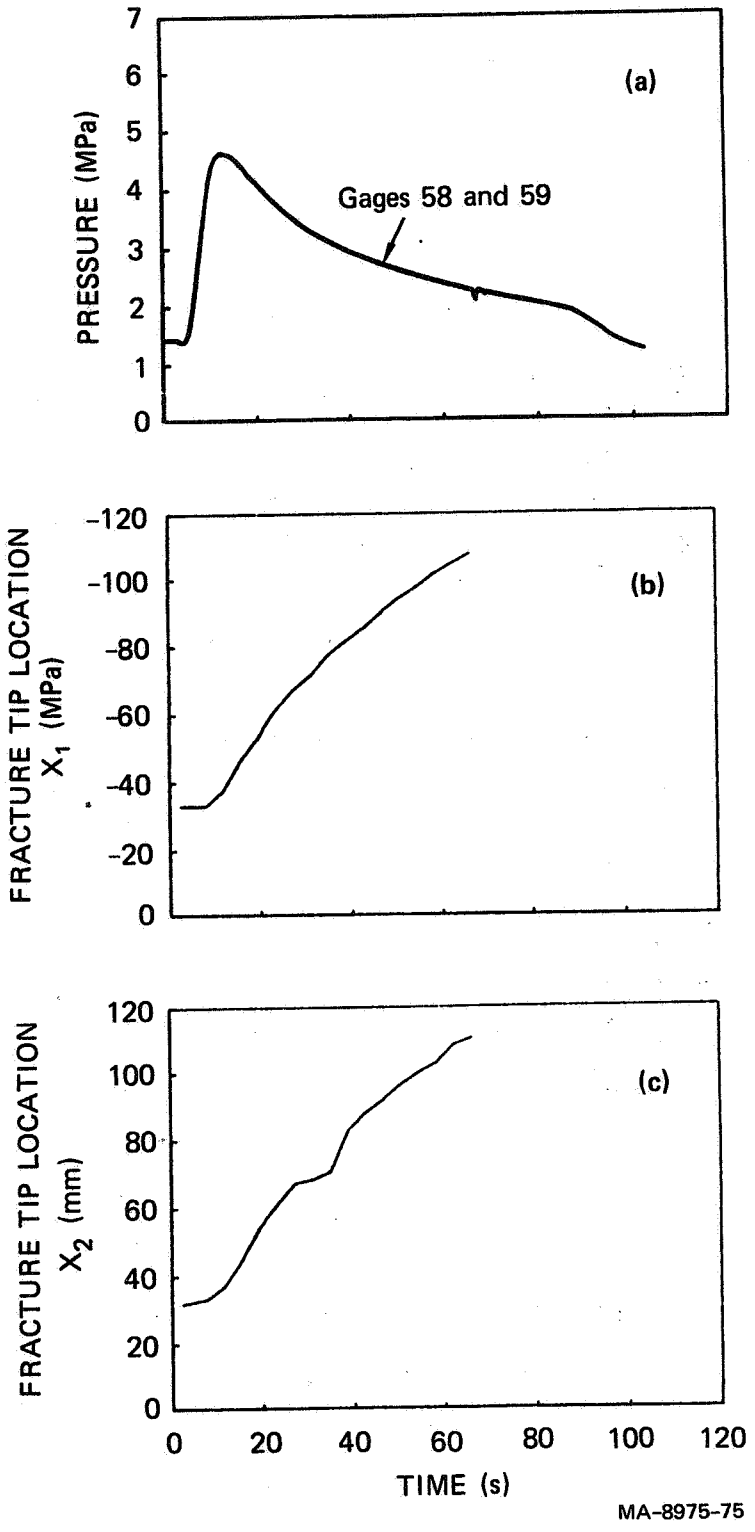

FIGURE 19 MAIN FRACTURE OF MODEL 27: (a) PRESSURES IN GAGES 58 AND 59; (b) FRACTURE TIP LOCATION X_1; (c) FRACTURE TIP LOCATION X_2

Table 4

QUANTITATIVE DATA TAKEN AT SEVERAL TIMES DURING THE MAIN FRACTURE OF MODEL 27[a] (pumping started at t = 2.45 s)

Time (s)	P_b (MPa)	Gage 56 (MPa)	Gage 57 (MPa)	Gage 58 (MPa)	Gage 59 (MPa)	LVDT (μm)	X_1 (mm)	X_2 (mm)	ℓ (mm)
2.45	-	1.35	1.278	1.432	1.440	--	-33	32	33
11.70	5.35	5.73	1.298	4.585	4.574	--	-38	37	37
15.65	5.07	5.45	1.292	4.513	4.521	--	-46	45	46
19.55	4.61	4.99	1.281	4.159	4.165	--	-53	54	54
23.45	4.34	4.52	1.264	3.827	3.833	--	-61	61	61
27.35	3.78	4.16	1.242	3.540	3.546	--	-67	67	67
35.15	3.30	4.68	1.198	3.123	3.134	--	-77	71	74
39.10	3.12	4.50	1.621	2.958	2.969	--	-82	83	82
46.90	2.82	3.20	1.961	2.699	2.710	--	-90	92	91
54.70	2.59	2.97	1.992	2.493	2.501	--	-98	100	99
66.25	2.34	2.72	1.922	2.231	2.245	--	-107	110	109

[a] For error estimates see Table 2 and the discussion in Section 2.1.

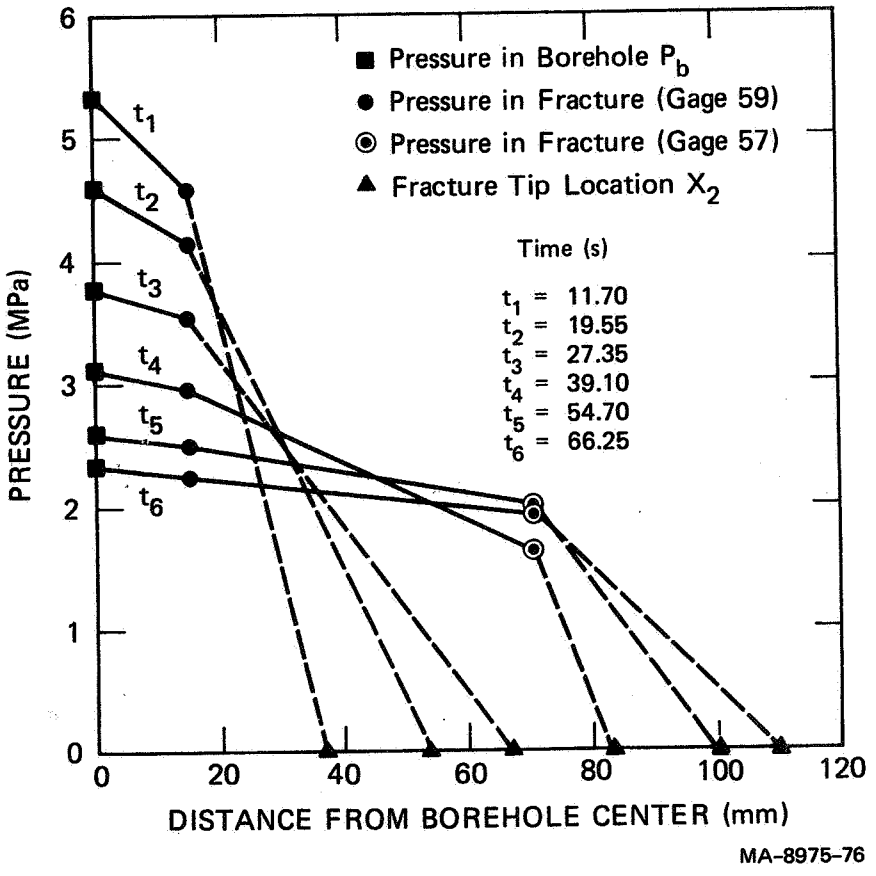

FIGURE 20 PRESSURE DISTRIBUTIONS AT SEVERAL TIMES DURING THE MAIN FRACTURE OF MODEL 27

Pumping started at t = 2.45 s.

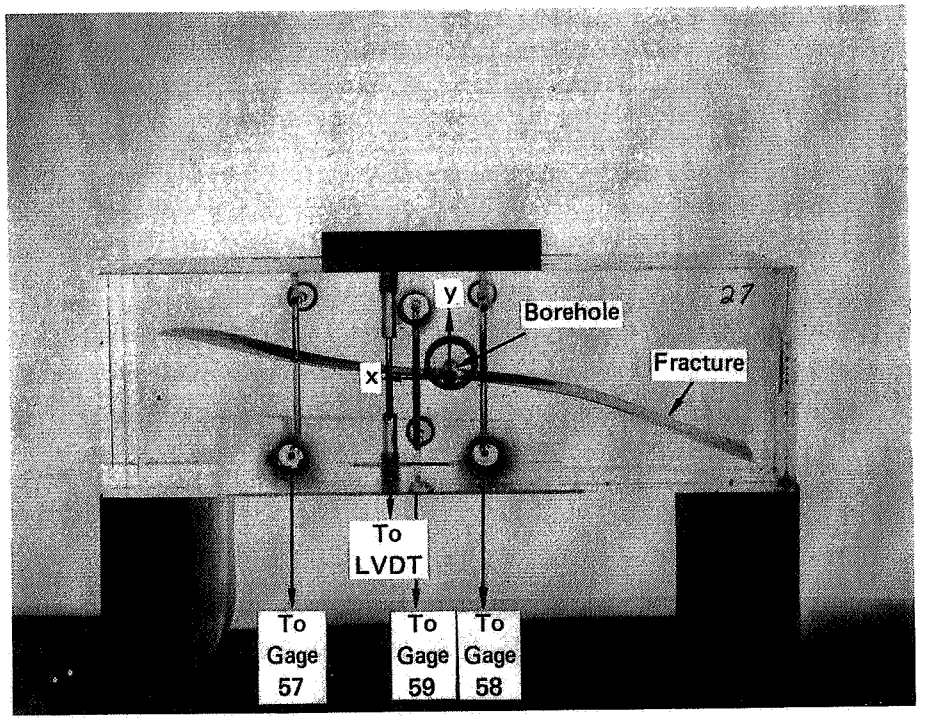

MP-8975-93

FIGURE 21 PHOTOGRAPH OF THE FRACTURE SURFACE IN MODEL 27
(viewed from the bottom)

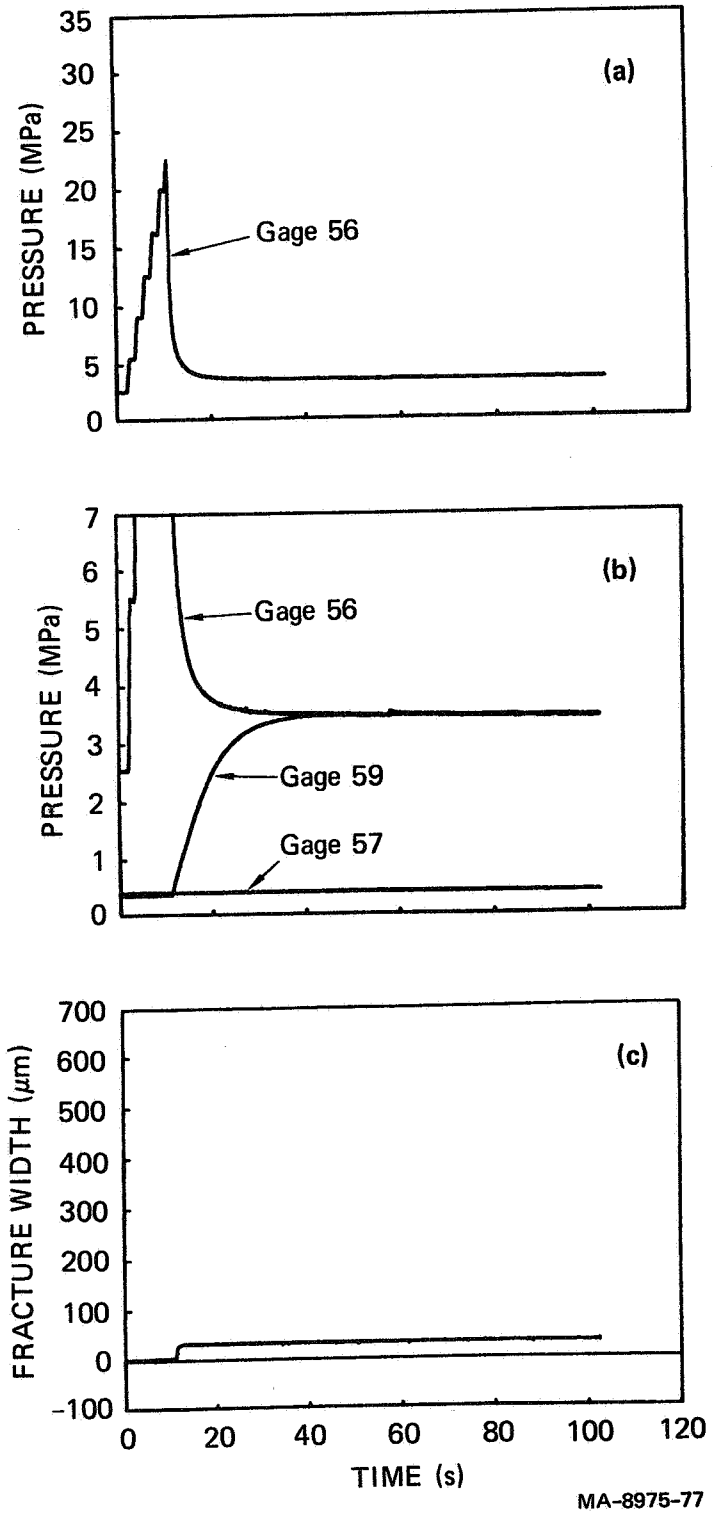

FIGURE 22 PREFRACTURE OF MODEL 28: (a) PRESSURE IN GAGE 56; (b) PRESSURES IN GAGES 56, 57, AND 59; (c) FRACTURE WIDTH

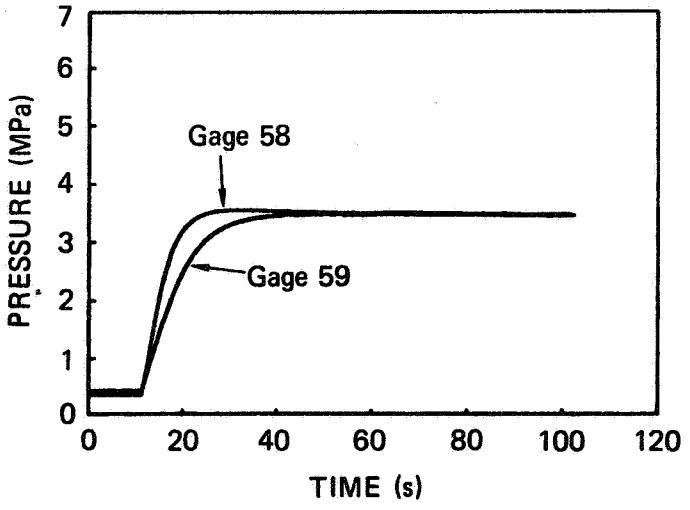

FIGURE 23 PRESSURES IN GAGES 58 AND 59 DURING THE PREFRACTURE OF MODEL 28

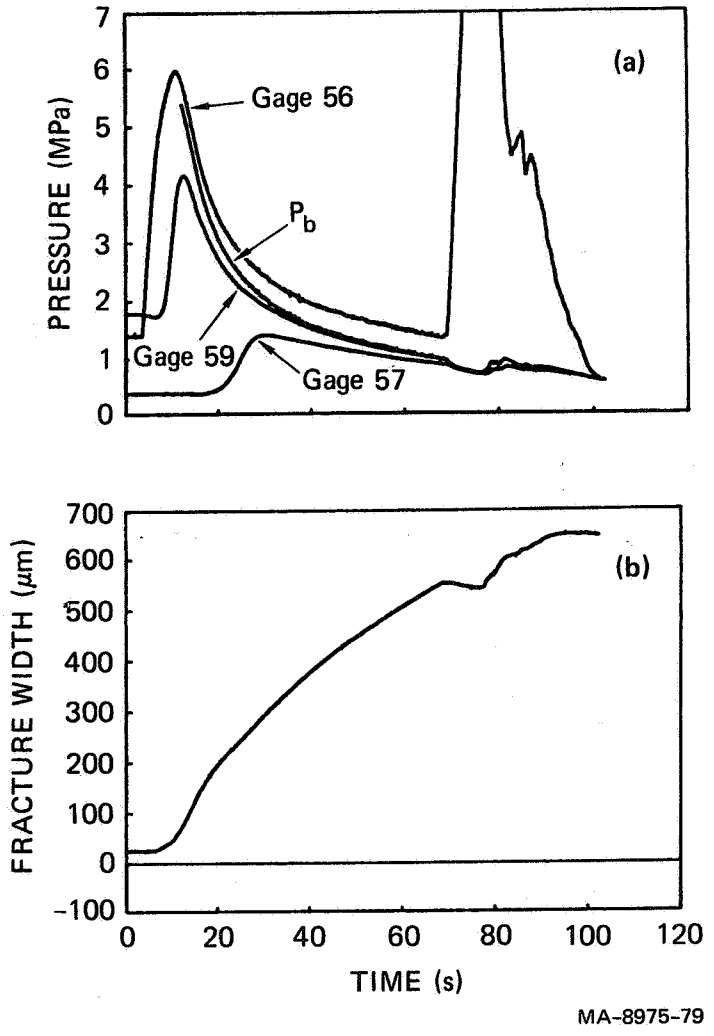

FIGURE 24 MAIN FRACTURE OF MODEL 28: (a) BOREHOLE PRESSURE P_b AND PRESSURES IN GAGES 56, 57, AND 59; (b) FRACTURE WIDTH

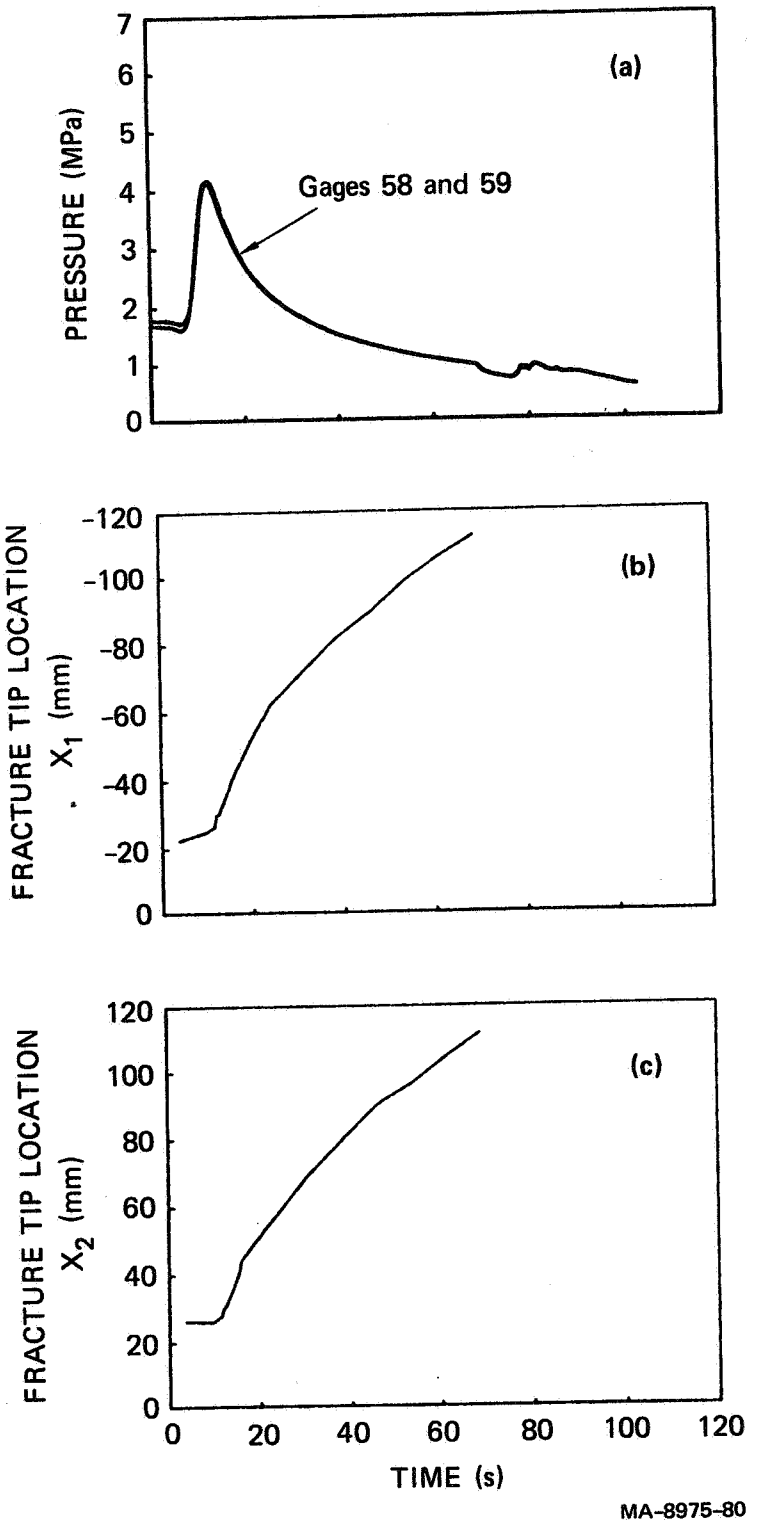

FIGURE 25 MAIN FRACTURE OF MODEL 28: (a) PRESSURE IN GAGES 58 AND 59; (b) FRACTURE TIP LOCATION X_1; (c) FRACTURE TIP LOCATION X_2

Table 5

QUANTITATIVE DATA TAKEN AT SEVERAL TIMES DURING THE MAIN FRACTURE OF MODEL 28[a] (pumping started at t = 3.70 s)

Time (s)	P_b (MPa)	Gage 56 (MPa)	Gage 57 (MPa)	Gage 58 (MPa)	Gage 59 (MPa)	LVDT (μm)	X_1 (mm)	X_2 (mm)	ℓ (mm)
3.70	-	1.64	0.371	1.677	1.766	25	-22	26	24
11.90	5.43	5.81	0.362	4.145	4.106	69	-30	30	30
12.55	5.26	5.64	0.365	4.134	4.159	78	-30	31	31
15.50	4.20	4.58	0.362	3.507	3.546	133	-40	40	40
16.05	4.01	4.39	0.359	3.381	3.432	142	-42	44	43
19.25	3.23	3.61	0.412	2.827	2.850	185	-51	50	50
24.30	2.51	2.89	0.886	2.292	2.273	236	-62	58	60
30.35	2.03	2.41	1.396	1.894	1.891	294	-71	69	70
38.50	1.61	1.99	1.279	1.557	1.560	364	-82	80	81
46.15	1.39	1.77	1.153	1.345	1.343	420	-89	90	90
53.85	1.22	1.60	1.034	1.172	1.178	470	-99	96	97
61.50	1.07	1.45	0.942	1.050	1.053	514	-106	104	105
68.90	0.97	1.35	0.861	0.949	0.953	552	-112	111	112

[a]For error estimates see Table 2 and the discussion in Section 2.1.

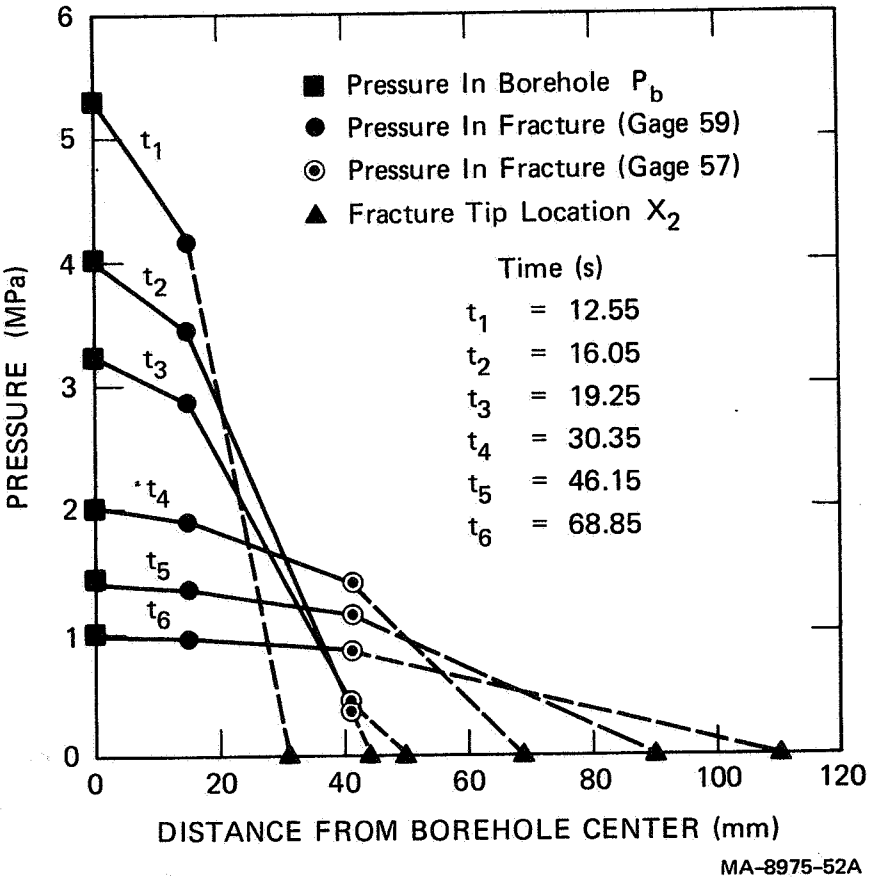

FIGURE 26 PRESSURE DISTRIBUTIONS AT SEVERAL TIMES DURING THE MAIN FRACTURE OF MODEL 28

Pumping started at t = 3.70 s.

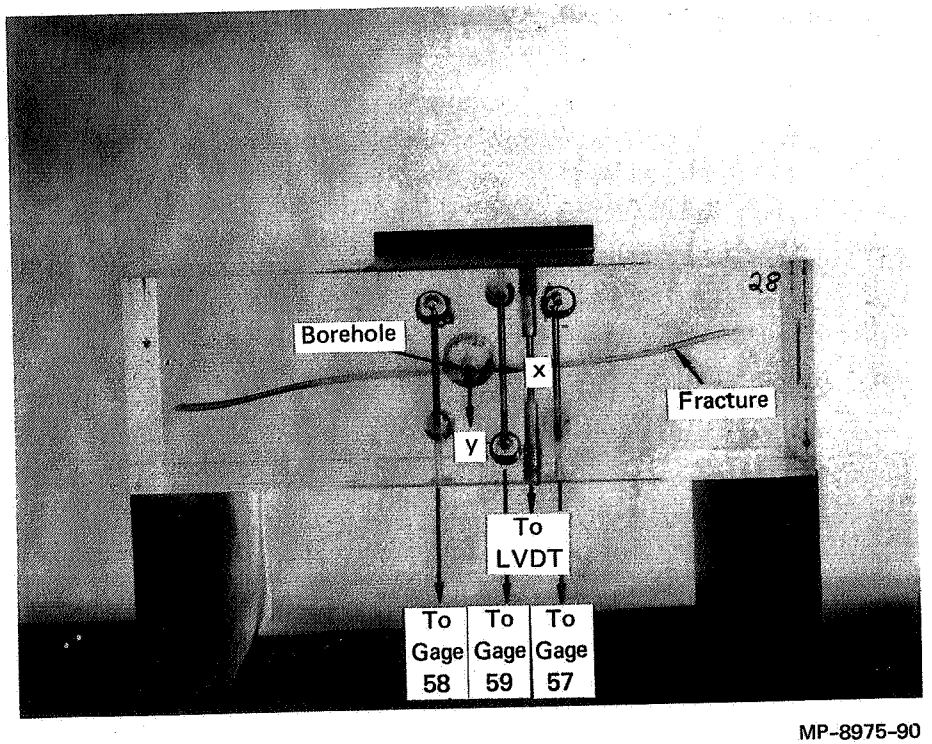

MP-8975-90

FIGURE 27 PHOTOGRAPH OF THE FRACTURE SURFACE IN MODEL 28
(viewed from the bottom)

is strong experimental evidence that these gages are actually measuring the pressure in the fracture, since we would expect the pressure to drop in the borehole and the fracture when the piston bottoms out.

Figures 12(b), 18(b), and 24(b) show the fracture width during the main fracture. The scope recording the fracture width in Experiment 25 triggered late so the time in Figure 12(b) has been shifted to impose time correlation between the peak of the LVDT record and the more dramatic pressure drop observed in the Gage 56 record. The fracture width record in Figure 18(b) does not continue to increase because the gage broke. In Experiment 28, the fracture width gage worked perfectly. In particular, we note that when the piston hit the bottom of the separation chamber, the pressure in the fracture dropped and the fracture width also decreased.

The symmetry of the main fracture is exhibited by Figures 13(a), 19(a), and 25(a), which compare the pressure records from Gages 58 and 59 that are located equidistant from the borehole and on opposite sides of it. These records show that the fracture propagated symmetrically. Fracture tip locations X_1 and X_2 were determined from the films up to the time when the piston hit the bottom of the separation chamber. The values of X_1 are plotted in Figures 13(b), 19(b), and 25(b) and those of X_2 are plotted in Figures 13(c), 19(c), and 25(c).

Tables 3, 4, and 5 summarize quantitative values for the fracture pressures, fracture width, and the fracture tip locations X_1 and X_2 for several times during the main fracture. Also included is the average fracture half-length ℓ defined by the formula

$$\ell = (X_2 - X_1)/2 \quad . \tag{2.1}$$

Furthermore, we note that pumping started at t = 2.45 s, 2.45 s, and 3.70 s in Experiments 25, 27, and 28, respectively. The first entries in these tables are the initial conditions of the main fracture because they correspond to the time the pump started. Furthermore, we note that the borehole pressure was determined only for times when the pump was

operating so no initial values are recorded in Tables 3, 4, and 5. Using the quantitative data in these tables, we constructed Figures 14, 20, and 26, which show the pressure distribution in the fracture at several times. In these figures, it has been assumed that the pressure at the fracture tip is zero. Therefore, broken lines have been used to connect the fracture tip to measured pressure values, and solid lines have been used to connect measured pressure values with other measured values. Even though the fracturing fluid is highly viscous, it appears that for later times, the fracture is fairly uniformly pressurized.

Figures 15, 21, and 27 are photographs of the fracture surfaces as viewed from the bottom of models 25, 27, and 28, respectively. Note the curved shapes of these fracture surfaces.

2.3 Interpretation and Analysis

The phenomenology experiments are briefly described in Appendix B. From this discussion, we recall that when water was used as a fracturing fluid, we obtained unstable discontinuous fracture growth and that we needed to use a highly viscous fracturing fluid to obtain quasi-static continuous fracture growth. To explain why a highly viscous fluid has a stabilizing effect on fracture propagation, we determined the critical pressure for fracture propagation associated with two different pressure distributions.* For the first pressure distribution, the fracture of half-length ℓ was uniformly pressurized with a pressure P_c so that

$$P = P_c \quad \text{for} \quad |x| \leq \ell \tag{2.2}$$

For the second pressure distribution, the fracture was uniformly pressurized with pressure P_c out to a distance a; then from $|x| = a$ to the fracture tip $|x| = \ell$, the pressure decayed linearly to zero so that

*This discussion is similar to the discussion in Reference 19.

$$P = \begin{cases} P_c & \text{for} \quad |x| \leq a \\ P_c\left(\dfrac{\ell - x}{\ell - a}\right) & \text{for} \quad a \leq |x| \leq \ell \end{cases} \tag{2.3}$$

From Reference 20, we recall that for an infinite, linearly elastic, isotropic medium in plane strain, the stress intensity factor* K_1 is given by the formula

$$K_1 = 2\left(\frac{\ell}{\pi}\right)^{1/2} \int_0^{\ell} \frac{P(x)}{(\ell^2 - x^2)^{\frac{1}{2}}}\, dx \tag{2.4}$$

At fracture initiation, the value of K_1 equals the value of the fracture toughness K_{Ic} of the material so for the pressure distribution (2.2), we have

$$\frac{P_c(\pi a)^{\frac{1}{2}}}{K_{Ic}} = f_1(\alpha) = \frac{1}{\alpha^{\frac{1}{2}}} \tag{2.5}$$

and for the pressure distribution (2.3), we have

$$\frac{P_c(\pi a)^{\frac{1}{2}}}{K_{Ic}} = f_2(\alpha) = \frac{1}{\alpha^{\frac{1}{2}} F(\alpha)} \tag{2.6}$$

*The definition of the stress intensity factor K_1 found in Reference 20 is commonly reserved for the quantity k_1, which equals $K_1/\pi^{1/2}$ [see Reference 21].

where

$$\alpha = \ell/a \quad ,$$

$$F(\alpha) = \frac{2}{\pi} \sin^{-1}\left(\frac{1}{\alpha}\right) + \frac{\left[1 - \frac{2}{\pi} \sin^{-1}\left(\frac{1}{\alpha}\right) - \frac{2}{\pi}\left(1 - \frac{1}{\alpha^2}\right)^{1/2}\right]}{1 - \frac{1}{\alpha}} \qquad (2.7)$$

The pressure distribution (2.2) associated with the function f_1 models the pressure distribution in a fracture that is pressurized with an inviscid fluid, whereas the pressure distribution (2.3) associated with the function f_2 models the pressure distribution in a fracture that is pressurized with a highly viscous fluid. For this latter case, we expect a steep pressure gradient to exist at the fracture tip at the onset of fracture propagation. Figure 28 shows plots of the functions f_1 and f_2. For the inviscid case (f_1), the critical pressure P_c decreases monotonically with increasing fracture length. This means that the fracture would tend to propagate unstably until the pressure is reduced. This fact may explain the stepping growth observed in the phenomenology experiments in which water was used as a fracturing fluid. (Recall that for constant volumetric pumping rate, the fracture inflated until the critical pressure for fracture propagation was reached, then it grew dynamically until the pressure reduced and the step process continued.) For the highly viscous case (f_2), we observe quite a different behavior because there exists a region ($\alpha < 1.66$) for which the critical pressure must increase with increasing fracture length to maintain fracture propagation. This means that the fracture propagation must be stable and therefore is controlled by the pumping rate because the fracture tip cannot advance rapidly without creating a steep pressure gradient there and without requiring an increase in pressure. This also means that since the fracture criterion is extremely sensitive to the pressure distribution near the fracture tip [e.g., the Kernal of the integral in (2.4) is square root singular at the fracture tip], a

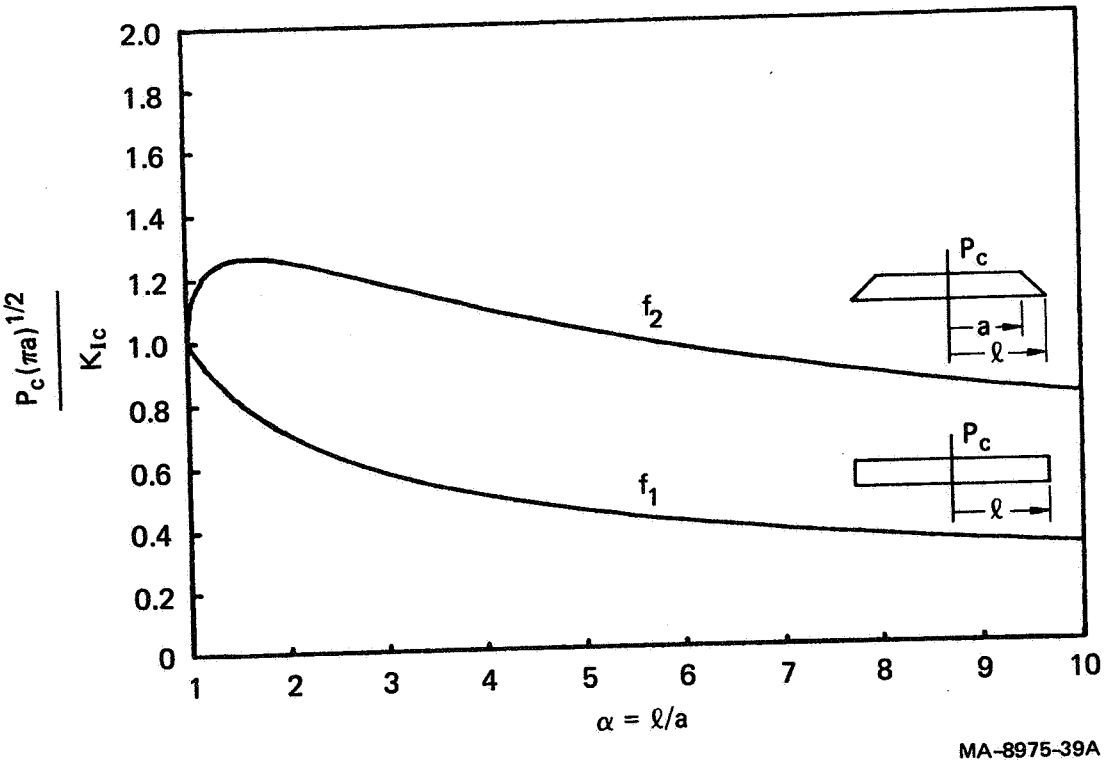

FIGURE 28 CRITICAL PRESSURE P_c [normalized by $K_{Ic}/(\pi a)^{1/2}$] ASSOCIATED WITH TWO DIFFERENT PRESSURE DISTRIBUTIONS IN A FRACTURE

successful analysis of hydraulic fracture propagation will require an accurate description of the fluid flow near the fracture tip.

The results of these experiments can be analyzed by invoking various assumptions. For example, plane strain assumptions can be made, and the analytical formulas of the solution described in Appendix A and the solutions of Nordgren and Geertsma and de Klerk can be used. Before discussing the comparison of these solutions with the experiments, we note that if one were to analyze the experiments with a three-dimensional code, it would be necessary to specify appropriate boundary conditions at the chloroform welds that compose the top and bottom interfaces of the middle layer of PMMA in the impermeable models (see Figure 5). For this reason, we sectioned PMMA models that were fractured using a low viscosity fracturing fluid (water) and two highly viscous fracturing fluids (epoxy and Dow Corning 100,000-centistoke fluid) and looked at the interfaces under a microscope. We observed that for the highly viscous fluids, the fracture tip that stopped propagating in the chloroform weld had a bulb shape that remained open after pressure was relieved in the fracture. This suggests that although the top and bottom PMMA layers of the models give support to the middle layer, plane strain conditions may still exist in horizontal planes of the middle layer. A more detailed discussion of this investigation is reported in Appendix C.

Most of the analytical or numerical analyses of hydraulic fracturing problems treat the formation as an infinite medium. To draw conclusions from the comparison of the predictions of these analyses with the experimental results, it is necessary to investigate the effect of the finite dimensions of our models. From Reference 22, p. 2.1, we recall that for an internally pressurized fracture of half-length ℓ in a specimen, in plane strain, of finite length 2b and infinite width, the critical pressure P_c for fracture initiation is given by

$$P_c = \left[\frac{K_{Ic}}{(\pi\ell)^{\frac{1}{2}}}\right]\left[\cos\frac{\pi\ell}{2b}\right]^{\frac{1}{2}} \quad \text{for} \quad \frac{\ell}{b} < 0.8 \ . \tag{2.8}$$

Also, for the same internally pressurized fracture in a specimen, in plane strain, of finite width 2h and infinite length, the critical pressure P_c is given by

$$P_c = \left[\frac{K_{Ic}}{(\pi \ell)}\right]\left[\frac{(1 - s)^{3/2}}{0.65}\right] \quad \text{for} \quad 0.5 < s \leq 1 \qquad (2.9)$$

where

$$s = \frac{\ell}{\ell + h} \quad . \qquad (2.10)$$

The formulas (2.8) and (2.9) as well as the formula (2.5) for an infinite medium have been evaluated using the dimensions 2b = 305 mm and 2h = 96 mm and the material properties of PMMA given in Section 2.1. Figure 29 shows the resulting plots of the critical pressure P_c. Clearly, the finite width of the impermeable models significantly influences the experimental results as the fracture length increases.

In the remainder of this section, we compare the results of Experiment 28 with the predictions of the solution of Appendix A and the solutions of Nordgren[4] and Geertsma and de Klerk.[6] Experiment 28 has been selected for comparison purposes rather than Experiments 25 or 27 because of the problems with the fracture width records in Experiments 25 and 27. However, before comparing theory and experiment, it is interesting to examine to what extent the impermeable experiments are reproducible. Therefore, in Figure 30, we potted the borehole pressure P_b against the fracture length for Experiments 25, 27, and 28. The results of Experiments 25 and 27 are very close to each other, whereas the results of Experiment 28 fall about 1 MPa below those of the other experiments. Most likely, the fracturing pressure measured in Experiment 28 is lower than that measured in Experiments 25 and 27 because the dimensions of model 28 were smaller than those of models 25 and 27 (see Figure 5).

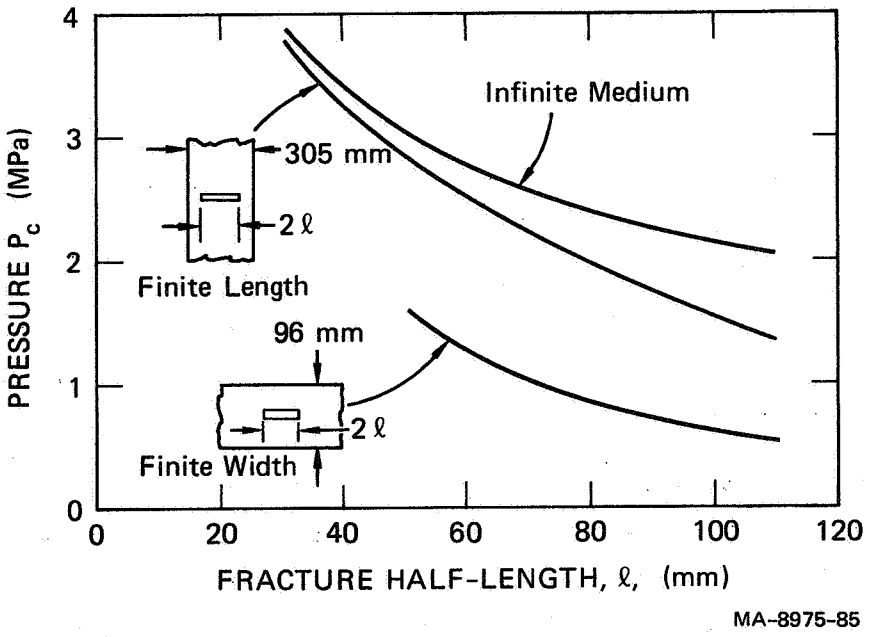

FIGURE 29 CRITICAL PRESSURE P_c ASSOCIATED WITH A FRACTURE OF HALF-LENGTH ℓ IN AN INFINITE MEDIUM, A MEDIUM OF FINITE LENGTH (305 mm) BUT INFINITE WIDTH, AND A MEDIUM OF FINITE WIDTH (96 mm) BUT INFINITE LENGTH

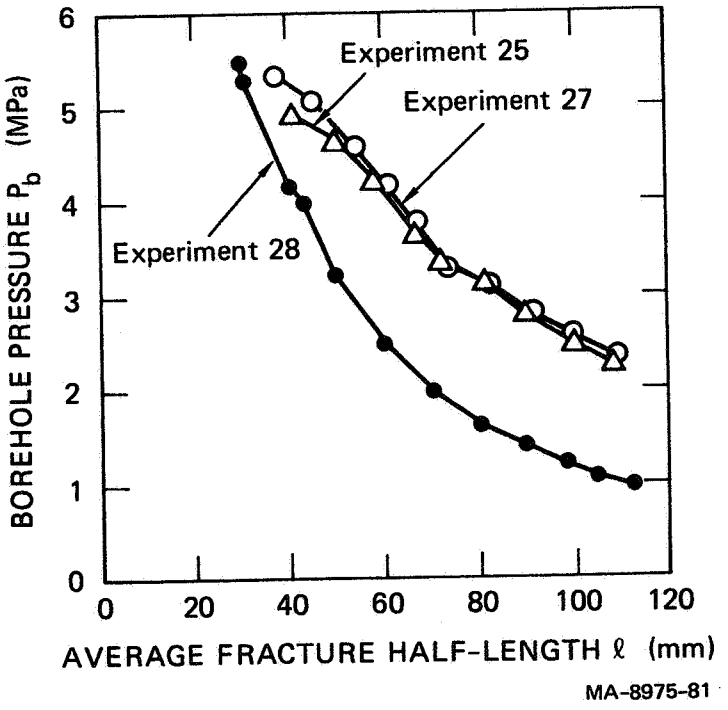

FIGURE 30 BOREHOLE PRESSURE P_b MEASURED IN EXPERIMENTS 25, 27, AND 28

To compare the results of Experiment 28 with the predictions of the present solution (Appendix A) and the solutions of Nordgren and Geertsma and de Klerk, we recall that, for the case of a two-sided fracture and no fluid leak-off, the fracture half-length ℓ, the borehole pressure P_b, and the fracture width at the borehole w_b predicted by Nordgren's solution are*

$$\ell = 0.68 \left[\frac{E\,(q/2)^3}{2(1-\nu^2)\mu\,H^4}\right]^{1/5} t^{4/5} \tag{2.11a}$$

$$P_b = 2.5 \left[\left\{\frac{E}{2(1-\nu^2)}\right\}^4 \frac{\mu\,(q/2)^2}{H^6}\right]^{1/5} t^{1/5} \tag{2.11b}$$

$$w_b = 2.5 \left[\frac{2(1-\nu^2)\,\mu\,(q/2)^2}{E\,H}\right]^{1/5} t^{1/5} \tag{2.11c}$$

and predicted by Geertsma and de Klerk's solution are

$$\ell = \left[\frac{2q}{\pi H}\left\{\frac{\pi H E}{168\,\mu q(1-\nu^2)}\right\}^{1/4}\right]^{2/3} t^{2/3} \tag{2.12a}$$

$$P_b = \left[\frac{21\,\mu\,q}{32\,\pi\,H}\left(\frac{E}{1-\nu^2}\right)^3\right]^{1/4} \ell^{-1/2} \tag{2.12b}$$

$$w_b = \left[\frac{168\,\mu\,q\,(1-\nu^2)}{\pi\,H\,E}\right]^{1/4} \ell^{1/2} \tag{2.12c}$$

where q is the volumetric flow rate and H is the height of the middle PMMA layer. In obtaining the formula for the fracture half-length ℓ in

*Since we are concerned here with a two sided fracture, q in Nordgren's formulas is replaced by q/2.

(2.12a), we have used the result [Reference 6, p. 1574, Eq. (13)] that the fracture volume V_f is given by

$$V_f = \frac{\pi}{2} H \ell w_b \tag{2.13}$$

and the fact that at any time t the fracture volume $V_f = qt$.

The formulas (2.11) and (2.12) and those of the present solution (Appendix A) were evaluated for the impermeable experiments ($q = 73.2$ mm^3/s, $\mu = 977$ Pa s and the material properties of PMMA), and the results are plotted in Figures 31, 32, and 33. Also included in these figures are the results of Experiment 28. In Figure 33, the time when the average fracture half-length measured in Experiment 28 equals 30.5 mm has been adjusted to equal the average of the times predicted by the present solution (R) and the solutions of Nordgren (N) and Geertsma and de Klerk (GK) for that value of fracture half-length.

The borehole pressures in Figure 31 show that the pressure predicted by the solution (N), which is based on plane strain in vertical planes, is considerably different than those predicted by the solutions (R) and (GK), which are based on plane strain in horizontal planes. Since the experimental results of Experiment 28 are closest to the predictions of the present solution (R), this suggests that the assumptions that the fracture is uniformly pressurized and that the formation is in plane strain in horizontal cross sections are fairly good. Furthermore, we note that including the effect of the finite size of the model would bring the theoretical results into closer agreement with the experimental results for the larger values of fracture length.

Figure 32 shows that the experimental values of fracture width are closer to the solution (R) than to the solutions (N) and (GK) for short fractures and the trend is reversed for long fractures. Taking the finite dimensions of the model into consideration, the predictions of the fracture width would increase relative to the predictions for an infinite medium. This effect would bring the theoretical predictions

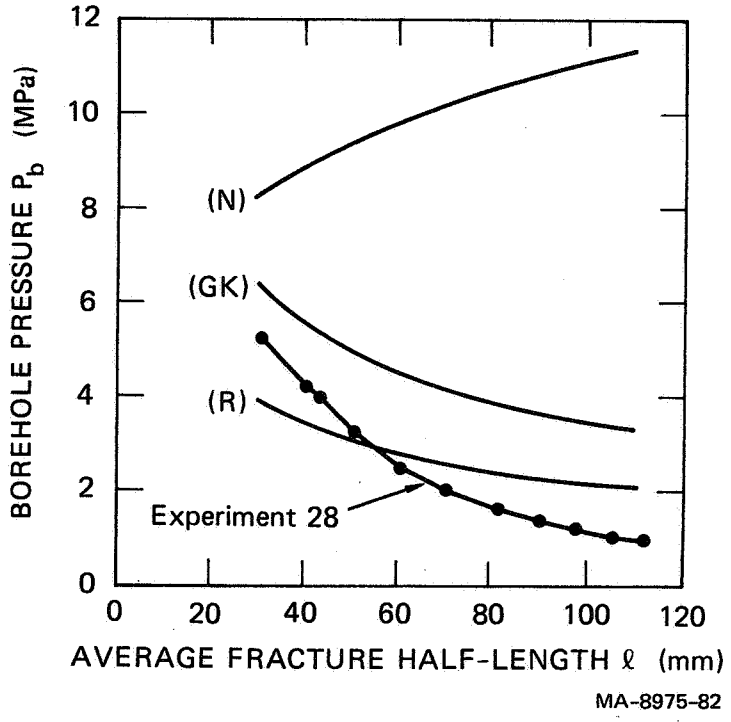

FIGURE 31 BOREHOLE PRESSURE P_b MEASURED IN EXPERIMENT 28 AND PREDICTED BY THE PRESENT SOLUTION (R) AND THE SOLUTIONS OF NORDGREN (N) AND GEERTSMA AND de KLERK (GK)

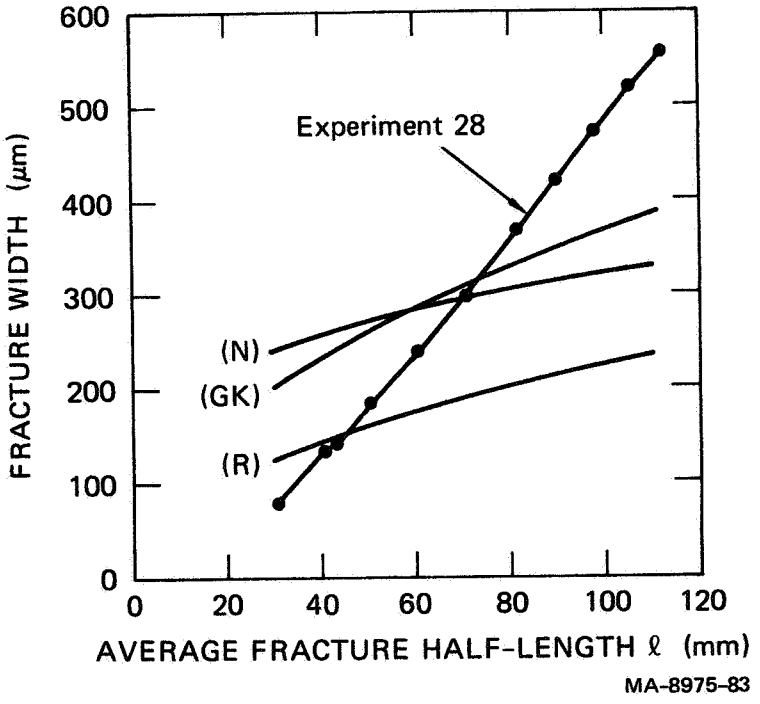

FIGURE 32 BOREHOLE FRACTURE WIDTH w_b PREDICTED BY THE PRESENT SOLUTION (R) AND THE SOLUTIONS OF NORDGREN (N) AND GEERTSMA AND de KLERK (GK)

Also included is the fracture width w measured in Experiment 28 at a location 28.5 mm from the borehole center.

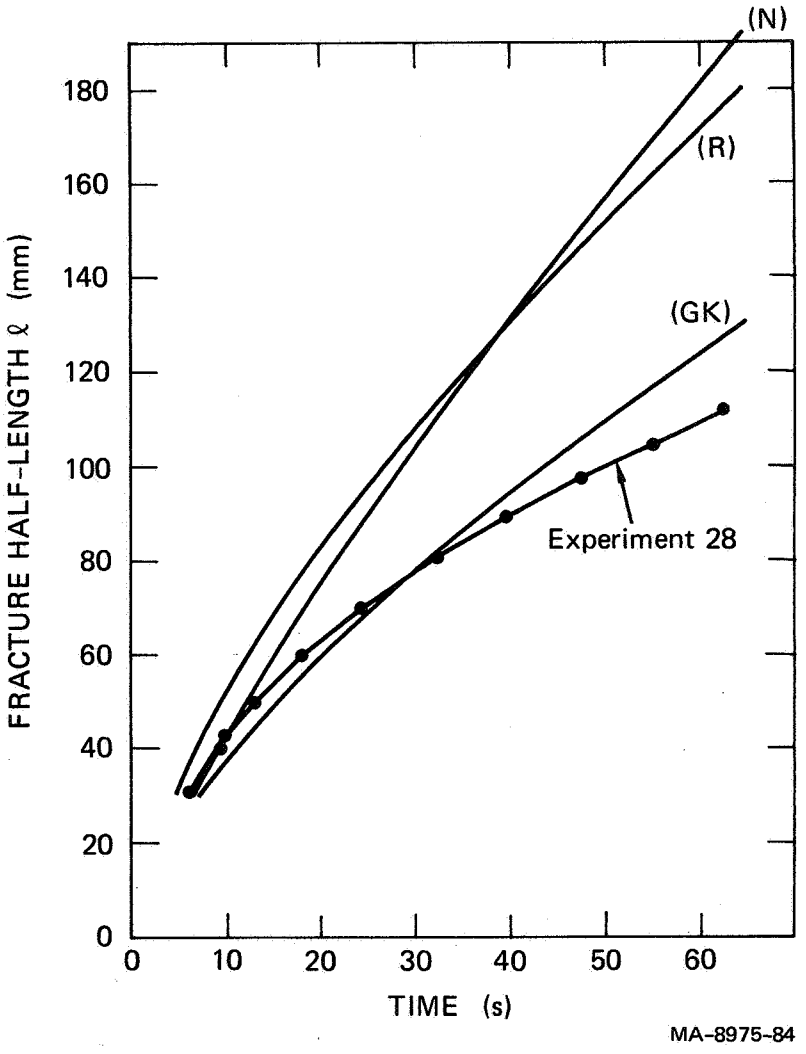

FIGURE 33 FRACTURE HALF-LENGTH MEASURED IN EXPERIMENT 28 (average value of both sides) AND PREDICTED BY THE PRESENT SOLUTION (R) AND THE SOLUTIONS OF NORDGREN (N) AND GEERTSMA AND de KLERK (GK)

The time when the average fracture half-length measured in Experiment 28 equals 30.5 mm has been adjusted to equal the average of the times predicted by the solutions (R), (N), and (GK) for that value of fracture half-length.

into better agreement with experimental results for the larger values of the fracture half-length.

From Figure 33, we observe that the prediction (GK) of the fracture half-length is in better agreement with the experimental results than the predictions (R) and (N). Again, we mention that the theoretical predictions would be brought into closer agreement with the experimental results if the finite dimensions of the model are taken into consideration.

In summary, these impermeable experiments can be modeled by assuming plane strain conditions exist in horizontal planes and that the fracture is uniformly pressurized. However, the finite size of the models should be taken into consideration to obtain good correlation between experiment and theory when the fracture length is long.

Finally, we mention that the fracture tips observed in these experiments (viewed from the front of the model) were only mildly curved (convex away from the borehole as in the sketch in Figure 6, also see Figure B2 in Appendix B) but, in particular, they were not semicircular in shape as suggested in Reference 23.

3. PERMEABLE EXPERIMENTS

3.1 Preliminary Analysis and Material Selection

Analyzing a propagating vertical hydraulic fracture in a permeable material is considerably more difficult than analyzing the fracture propagation in an impermeable material. For impermeable materials, there is no fluid leak-off so the total volume V_T of fluid pumped into the borehole creates fracture volume V_f. If the fracturing fluid is relatively inviscid the pressure distribution in the fracture is fairly uniform so linear elasticity and fracture mechanics can be used to determine the relationship between the half-length of the fracture ℓ and volume V_T of fluid pumped into the borehole. This relationship is independent of the volumetric flow rate q at which fluid is pumped into the borehole. For permeable materials, fluid leaks into the formation so knowing the volume V_T of fluid pumped into the borehole alone is not enough to determine the fracture length and width. The volume of fluid lost to the formation V_L depends on the time that the formation has been exposed to the fracturing fluid and hence depends on the pumping rate q.

Partly motivated by our need to select a material, a fracturing fluid, and a pumping rate for our experiments and partly motivated by our desire to better understand hydraulic fracturing processes, we developed a simple formula for analyzing a propagating vertical hydraulic fracture in a permeable material. Instead of specifying the functional form of the flow velocity of fluid leaking into the formation, as is done in the classical fluid leak-off model,[2] we determined the flow velocity as part of the solution by using Darcy's equation for flow in a permeable material. The results of this analysis proved to be significantly different than those of the classical fluid leak-off model, as described in Appendix A.

From this analysis, we observed that if the volume V_T of fluid pumped into the borehole is used as the independent variable instead of time, then the fracture half-length ℓ, the depth Y of fluid penetration into the formation, and the volume V_L of fluid lost to the formation depend on the pumping rate q and the viscosity of the fracturing fluid μ only through their product $q\mu$. Therefore, we could use the same pumping rate as was used in the impermeable experiments ($q = 73.2\ mm^3/s$) and merely vary the viscosity μ of the fracturing fluid to test the appropriateness of various materials.

On the basis of the analysis in Appendix A, we selected two candidate material and fluid combinations: (1) rock-matching grout 2C4 and water and (2) hydrostone and Dow Corning 200 silicone 1,000-centistoke fluid. These combinations theoretically should produce a measurable depth of fluid penetration in a reasonable time with a reasonable volume of fluid pumped. The grout was later eliminated in favor of the hydrostone because the depth of fluid penetration into the grout proved to be too small.

3.2 Experimental Procedures and Setup

The pump system used for the permeable experiments was essentially the same as that used for the impermeable experiments. Figure 34 is a photograph of the experimental setup. Because the models did not need to be prefractured in the permeable experiments, the hand pump was only used to prepressurize the pressure gages. The motor pump was used to pressurize the models by pumping at a constant volumetric pumping rate $q = 73.2\ mm^3/s$. Since most of the fluid leaked into the hydrostone model, we designed a larger separation chamber than was used in the impermeable experiments.

The borehole and separation chamber were filled with fracturing fluid, then the model was attached to the pump system and air was evacuated from the pumping fluid (water) by using a vacuum pump. The valves to the vacuum pump and water reservoir were closed to create a closed pump system. For the experiments with proppants, we mixed the proppants

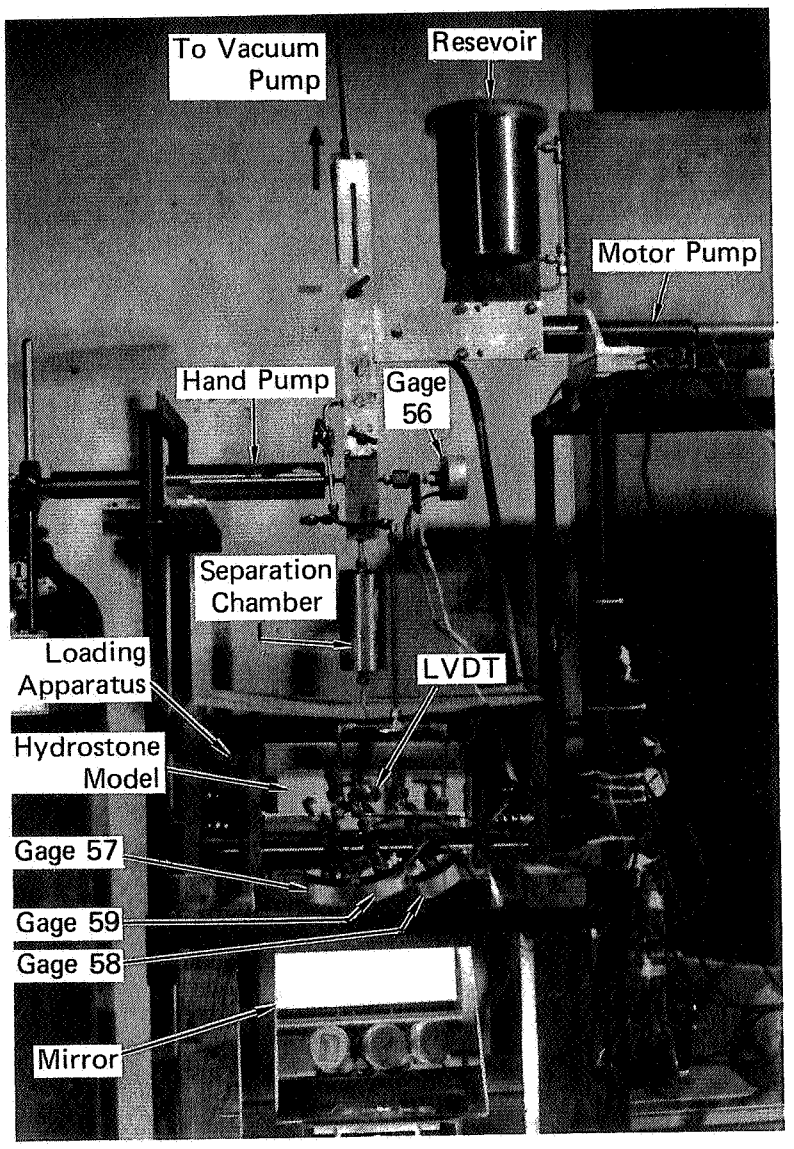

MP-8975-65

FIGURE 34 PHOTOGRAPH OF EXPERIMENTAL SETUP FOR PERMEABLE MODELS

in the fracturing fluid just before conducting the experiment to minimize the effect of settling.

The permeable models were constructed by bonding a layer of PMMA to the top and bottom of a hydrostone layer with epoxy. Figure 35 shows the dimensions of the permeable models. To maintain the direction of fracture propagation along the length of the model, we loaded the hydrostone layer with the loading apparatus shown in Figure 36. In constructing the models, the hydrostone was placed in the loading apparatus and loaded along its length with a uniaxial stress of 3.4 MPa, and then the PMMA layers were bonded in place.

Debonding of the hydrostone-PMMA interface was a problem that persisted throughout the experimental program. Experiments were conducted to determine the best bonding agent for this interface. From all the bonding agents tested, Shell Epon* 815 proved to be the best. Attempts to increase the bond strength were also made by roughening both the hydrostone and PMMA surfaces before bonding.

A borehole 6.35 mm in diameter was drilled completely through the hydrostone layer, and vertical notches 1.6 mm deep were filed into opposite sides of the borehole to initiate the fracture. A steel casing 6.35 mm OD and 3.18 mm ID with a flange was glued to the top of the borehole, and a PMMA disc was glued to the bottom of the borehole before the specimen was loaded and before the top and bottom layers of PMMA were bonded in place (see Figure 37). The flange and the disc were used to help prevent debonding of the interface.

The same Setra pressure gages that were used in the impermeable experiments were used in the permeable experiments. Pressure was measured outside the borehole (Gage 56 in Figure 37) and at three locations in the fracture (Gages 57, 58, and 59 in Figure 37). Figure 38 shows a sketch of the access holes used to measure the pressure in the fracture.

---

*The EPON RESIN 815 and curing agent Shell U were both manufactured by Shell Chemical Company.

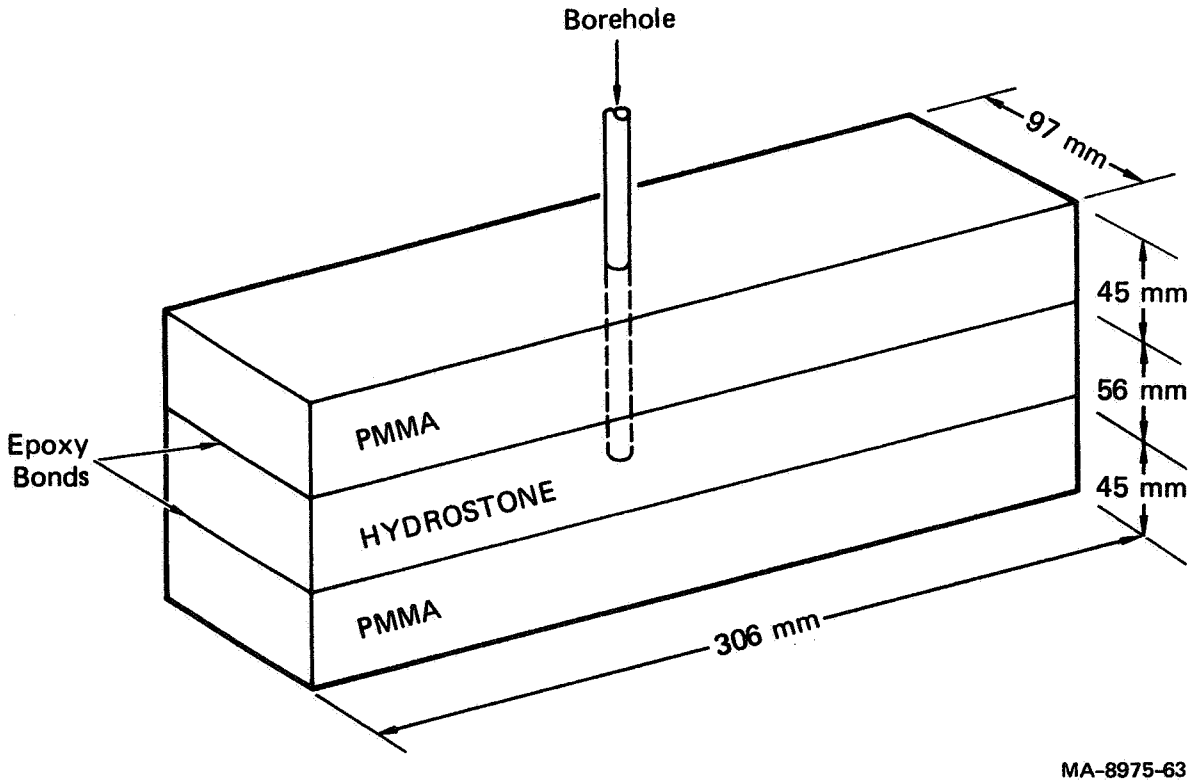

FIGURE 35 DIMENSIONS OF PERMEABLE MODELS

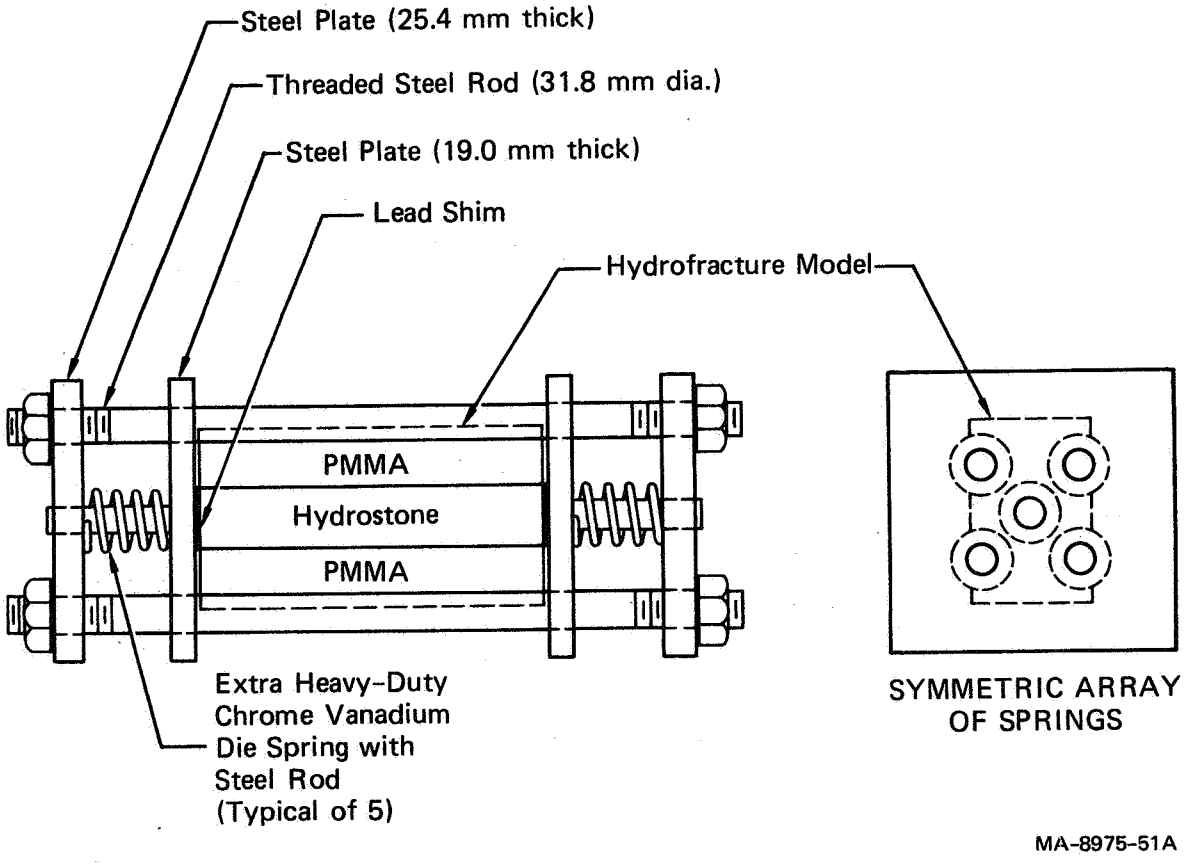

FIGURE 36 SPRING-LOADED MECHANISM FOR APPLYING AXIAL PRESTRESS TO HYDROSTONE SECTION OF MODEL

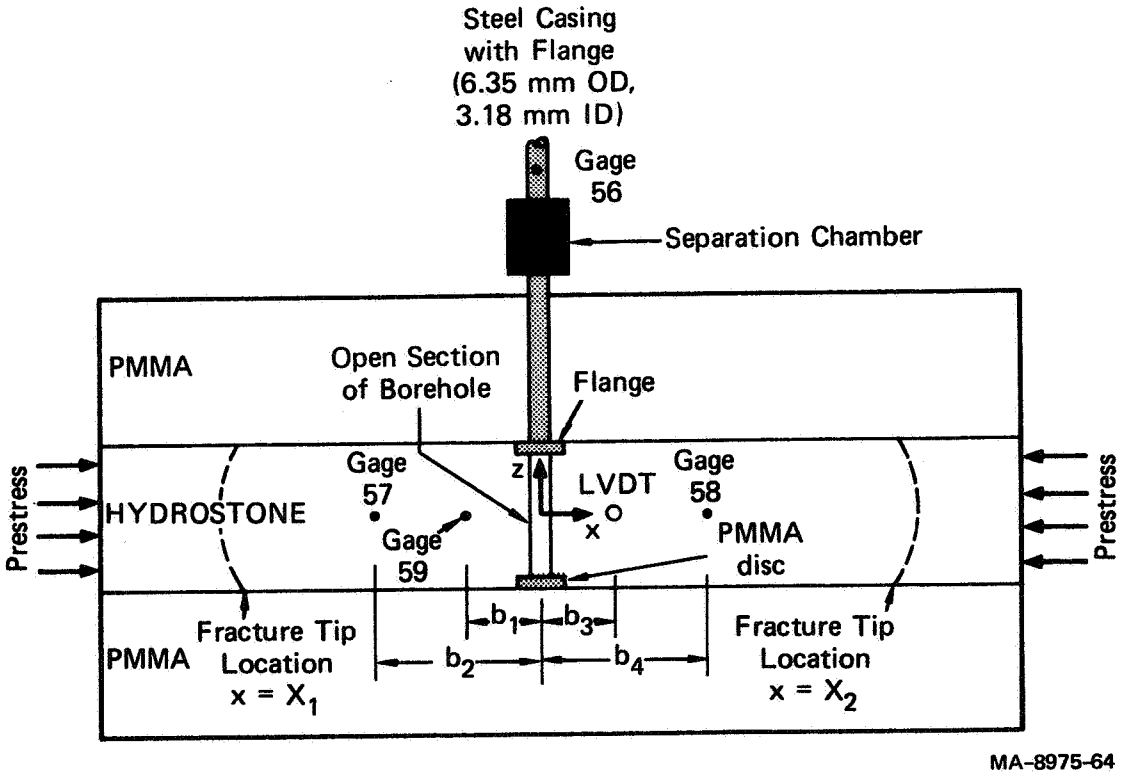

FIGURE 37 LOCATIONS OF PRESSURE GAGES 56, 57, 58, AND 59, LVDT, AND FRACTURE TIPS RELATIVE TO THE BOREHOLE IN THE PERMEABLE MODELS

The fluid leak-off from the access hole was reduced by coating the hole with shelac before the steel tube with flange was glued in place. However, the borehole was not coated with shelac. These access holes were filled with fracturing fluid, then the gages were attached and prepressurized to minimize the effect of any trapped air. In all cases, fracturing fluid free of proppants was used in the access holes. The values of the parameters (see Figure 37) that describe the gage locations in the permeable models are as follows:

$$b_1 = 20 \text{ mm}$$

$$b_2 = 45 \text{ mm}$$

$$b_3 = 10 \text{ mm}$$

$$b_4 = 45 \text{ mm}$$

The same LVDT that was used in the impermeable experiments to measure fracture width was used in the permeable experiments. Figure 37 shows the location of the LVDT. Basically, the LVDT mounting was the same as sketched in Figure 8 except that internally threaded aluminum discs were glued into the walls of the hydrostone layer to facilitate the attachment of the threaded steel bolts. The discussion in Section 2.1 of the error in the fracture width measurement caused by the compression of the PMMA also applies for hydrostone, except that the magnitude of the error is estimated to be less than 5 μm.*

A Locam motion picture camera was used to photograph the bottom PMMA-hydrostone interface through the mirror shown in Figure 34. The framing rate for the permeable experiments was 12 fps. All gages were recorded on Nicholet scopes and the digitizing unit of time was 0.5 s. Table 2 lists the RMS precision of the pressure gages and LVDT. As

---

*Recall from the footnote page 19 that the error e is less than (p/E) x 35 mm. For the permeable experiments p is less than about 3 MPa and E = 22.2 GPa so e is less than (3/22.2)(35) = 5 μm.

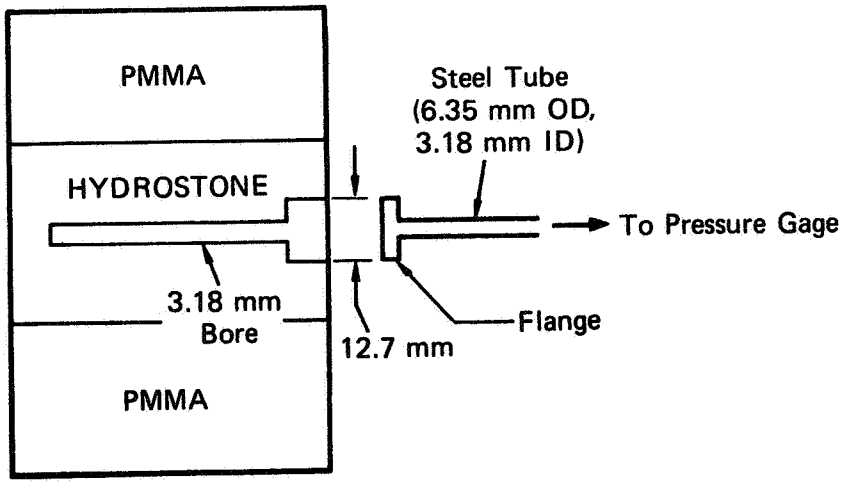

FIGURE 38 SKETCH OF ACCESS HOLE USED TO MEASURE PRESSURE IN THE FRACTURE IN THE PERMEABLE MODELS

noted above, the fracture width measurement in the permeable experiments underestimates the actual fracture width by less than 5 μm.

For the permeable experiments (both with and without proppants), the pressure drop between Gage 56 and the borehole was less than 0.07 MPa. Since this is the same order of magnitude as the error in the Gage 56 record, we have identified the pressure measured in Gage 56 with the borehole pressure P_b in presenting the permeable experimental results.

The fracture tip locations X_1 and X_2 and the fluid penetration contours were determined by digitizing the films on a telereadex. The error in the values of X_1, X_2, and the x and y coordinates of the fluid penetration contour associated with digitization is estimated to be $\pm$ 2 mm. However, since these models were photographed through the hydrostone-PMMA interface, the influence of this interface could not be eliminated. A cross section of model 41 showed that fluid penetration contours determined in this manner can be different from those associated with horizontal planes through the center of the hydrostone layer.

The hydrostone models were made by pouring a mixture of water and hydrostone* (water: hydrostone; 35:100 by weight) into a mold. The mixture was allowed to set about 16 hours, then was removed from the mold and allowed to cure in air for four weeks. To determine the material properties of the resulting mixture, we used standard techniques to measure the Young's modulus E, Poisson's ratio ν, compressive strength, tensile strength, aged density, dry density, connected porosity ϕ, permeability K, and fracture toughness K_{Ic}. The average values, number of tests, and range of values for these parameters are reported in Table 6. Differences between these values and those reported by Haimson and Fairhurst[15] may be attributed to differences in curing procedures.

---

*The hydrostone Gypsum Cement was purchased from United States Gypsum, Chicago, Illinois.

Table 6

MATERIAL PROPERTIES OF HYDROSTONE
(water: hydrostone; 35:100 by weight)

Material Property	Average Value	Number of Tests	Range of Values
Young's modulus (GPa) (compression)	22.2	16	9.4-32.3
Poisson's ratio	0.31	14	0.22-0.40
Compressive strength (MPa)	27.2	18	19.1-37.4
Tensile strength (MPa)	3.51	17	2.04-6.83
Fracture toughness ($MPa \cdot m^{\frac{1}{2}}$)	0.346	2	0.333-0.359
Aged density ($g \cdot m\ell^{-1}$)	1.66	35	1.63-1.70
Dry density ($g \cdot m\ell^{-1}$)	1.64	2	1.63-1.64
Connected porosity	0.295	6	0.290-0.302
Permeability (md)	8.3	3	7.7-8.7

Dow Corning 200 silicone fluid (1,000 centistoke) was used as the fracturing fluid in the permeable experiments (except Experiment 48 in which Dow Corning 100,000-centistoke fluid was used). The density ρ and viscosity μ of the 1,000-centistoke fluid at 25°C are as follows:

MATERIAL PROPERTIES OF 1,000 CENTISTOKE FLUID

Density	$\rho = 0.971$ g·mℓ$^{-1}$
Viscosity	$\mu = 971$ cp

Two size ranges of fly ash particles were used as the proppants. These two proppant mixes are denoted as fly ash I and fly ash II and their properties are shown below:

MATERIAL PROPERTIES OF PROPPANTS

Proppant	Average Density (g·mℓ$^{-1}$)	Range of Diameters (μm)
Fly ash I	2.46	43 to 74
Fly ash II	2.46	5 to 15

For the experiments that used proppants, we mixed 15 grams of fly ash particles with 120 mℓ of fluid. This mixture of proppants was chosen to yield a volume percentage of solid particles that is similar to that used in hydraulic fracture treatments in the field.[1] Slurry I denotes the fluid-proppant mixture that used fly ash I and slurry II denotes the mixture that used fly ash II. The densities of these slurries were computed and the viscosities measured and the results are summarized in Table 7.

Table 7

MATERIAL PROPERTIES OF FLUID-PROPPANT SLURRIES AT 26°C

	Average Density ($g \cdot m\ell^{-1}$)	Average Viscosity (cp)	Number of Tests	Range of Values (cp)
Slurry I	1.04	1056	5	1050-1060
Slurry II	1.04	1044	4	1040-1048

3.3 Main Permeable Experiments Without Proppants

In some of the permeable experiments debonding occurred at the hydrostone-PMMA interface, whereas in other experiments the fracture changed its orientation and propagated toward the front or back surfaces of the models instead of maintaining a vertical orientation. In the latter situation, the fracture reached the front or back surfaces of the model and fluid leaked out. This section summarizes the results of Experiments 41, 46, 47, 48, and 50, which used models 41, 46, 47, 48, and 50, respectively. In Experiments 41, 46, 47, and 50, Dow Corning 200 silicone fluid (1,000 centistoke) was used as a fracturing fluid, whereas in Experiment 48, Dow Corning 200 silicone fluid (100,000 centistoke) was used as a fracturing fluid. Figures 39 through 45, 46 through 49, 50 through 53, and 54 correspond to Experiments 41, 46, 47, and 50, respectively. Tables 8, 9, and 10 correspond to Experiments 41, 46, and 47, respectively.

Figures 39, 46, and 50 show the borehole pressure (Gage 56) during the fracture of the permeable models. Model 41 did not debond nor did the fracture reach the front or back surfaces of the hydrostone layer so the record is valid until the time the pump stopped (t = 631.0 s). From the movie of Experiment 46, we determined that at t = 171.0 s fluid started leaking into the bottom interface of model 46. This time correlates well with the time the borehole pressure experienced a small

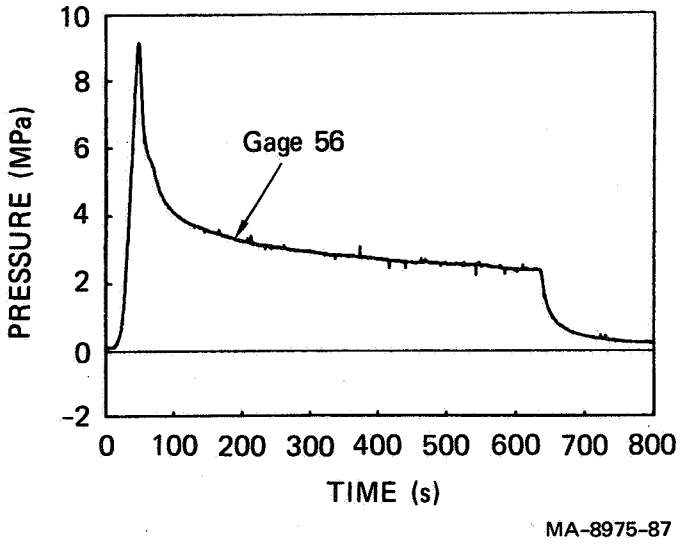

FIGURE 39 PRESSURE IN GAGE 56 DURING THE FRACTURE OF MODEL 41 (no proppants)

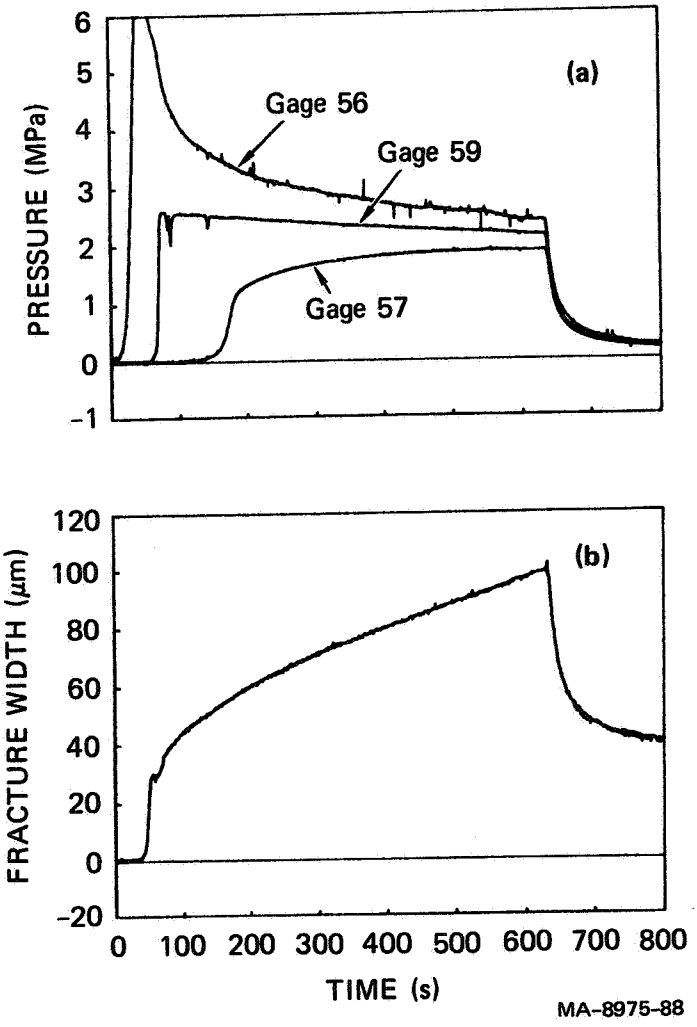

FIGURE 40 FRACTURE OF MODEL 41 (no proppants):
(a) PRESSURES IN GAGES 56, 57, and 59;
(b) FRACTURE WIDTH

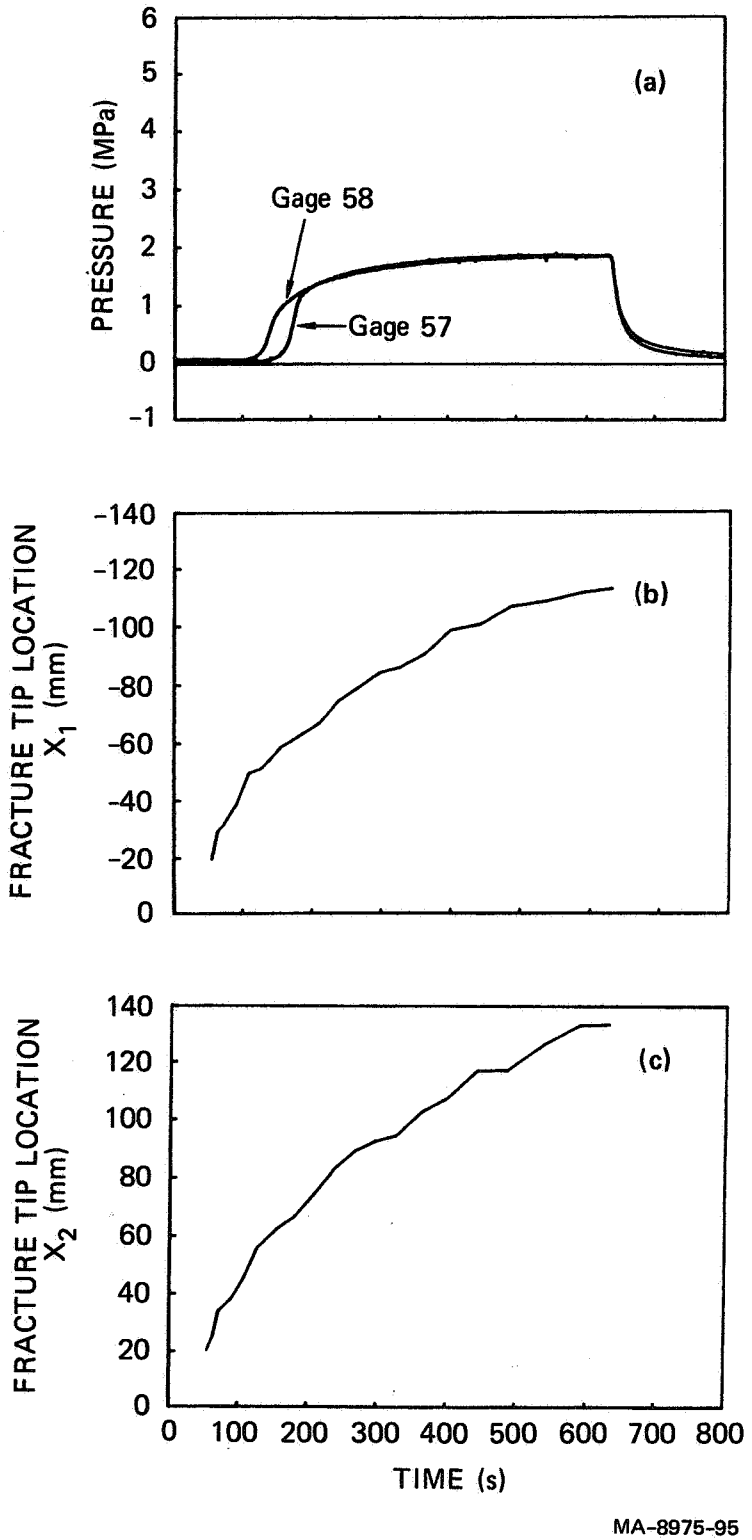

FIGURE 41 FRACTURE OF MODEL 41 (no proppants):
(a) PRESSURES IN GAGES 57 AND 58;
(b) FRACTURE TIP LOCATION X_1;
(c) FRACTURE TIP LOCATION X_2.

Table 8

QUANTITATIVE DATA TAKEN AT SEVERAL TIMES DURING THE FRACTURE OF MODEL 41[a] (pumping started at t = 10.5 s)

Time (s)	Gage 56 (MPa)	Gage 57 (MPa)	Gage 58 (MPa)	Gage 59 (MPa)	LVDT (μm)	X_1 (mm)	X_2 (mm)	ℓ (mm)
55.5	6.16	0.023	0.034	0.012	30	-20	20	20
63.5	5.70	0.023	0.048	0.166	30	-30	25	27
72.5	5.20	0.020	0.059	2.484	36	-32	34	33
91.0	4.34	0.017	0.056	2.499	42	-39	38	39
109.0	3.96	0.017	0.076	2.561	46	-50	46	48
127.0	3.75	0.040	0.203	2.543	50	-51	56	54
155.5	3.53	0.158	0.946	2.505	53	-59	62	61
181.5	3.36	1.056	1.200	2.490	57	-62	67	65
210.5	3.21	1.372	1.371	2.460	61	-67	75	71
239.5	3.11	1.500	1.484	2.428	64	-75	83	79
268.5	3.00	1.601	1.566	2.407	68	-79	89	84
297.5	2.94	1.663	1.628	2.377	70	-84	93	89
327.0	2.84	1.714	1.678	2.347	74	-86	95	90
363.5	2.79	1.771	1.735	2.324	77	-91	103	97
399.5	2.70	1.802	1.760	2.297	80	-99	107	103
443.0	2.62	1.819	1.794	2.250	84	-101	117	109
486.5	2.59	1.855	1.819	2.232	87	-107	117	112
537.5	2.55	1.875	1.844	2.199	92	-108	126	117
588.0	2.40	1.867	1.842	2.155	96	-111	133	122
631.0	2.38	1.867	1.847	2.131	99	-113	133	123

[a]For error estimates see Table 2 and the discussion in Section 3.2.

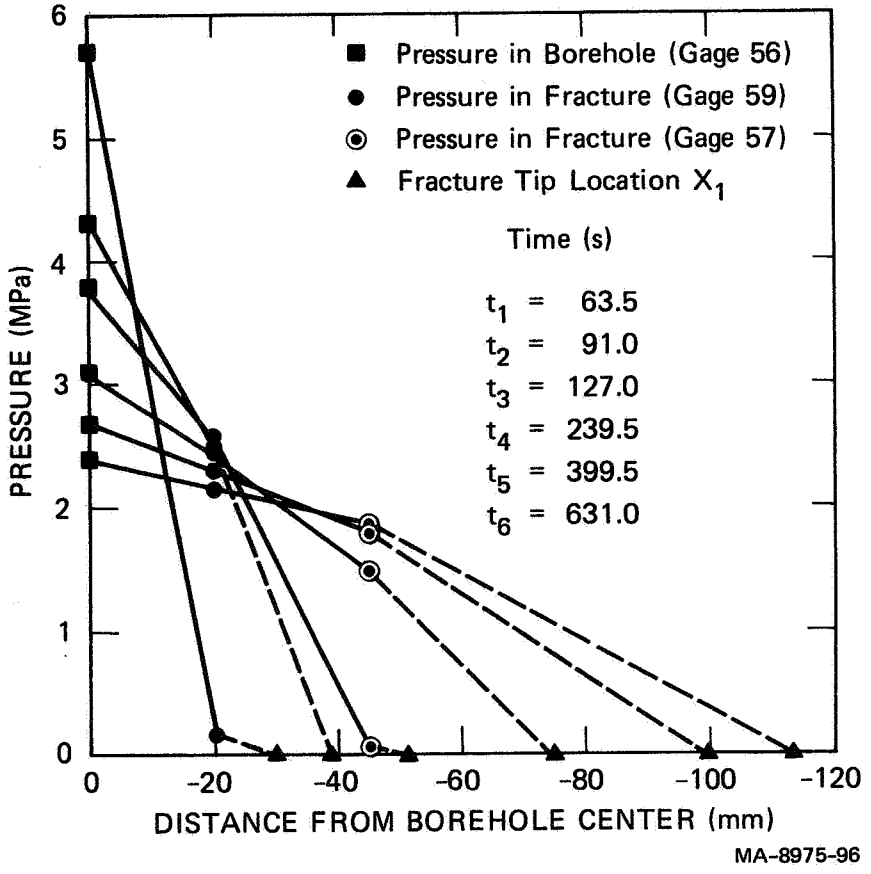

FIGURE 42 PRESSURE DISTRIBUTIONS AT SEVERAL TIMES DURING THE FRACTURE OF MODEL 41 (no proppants)

Pumping started at t = 10.5 s.

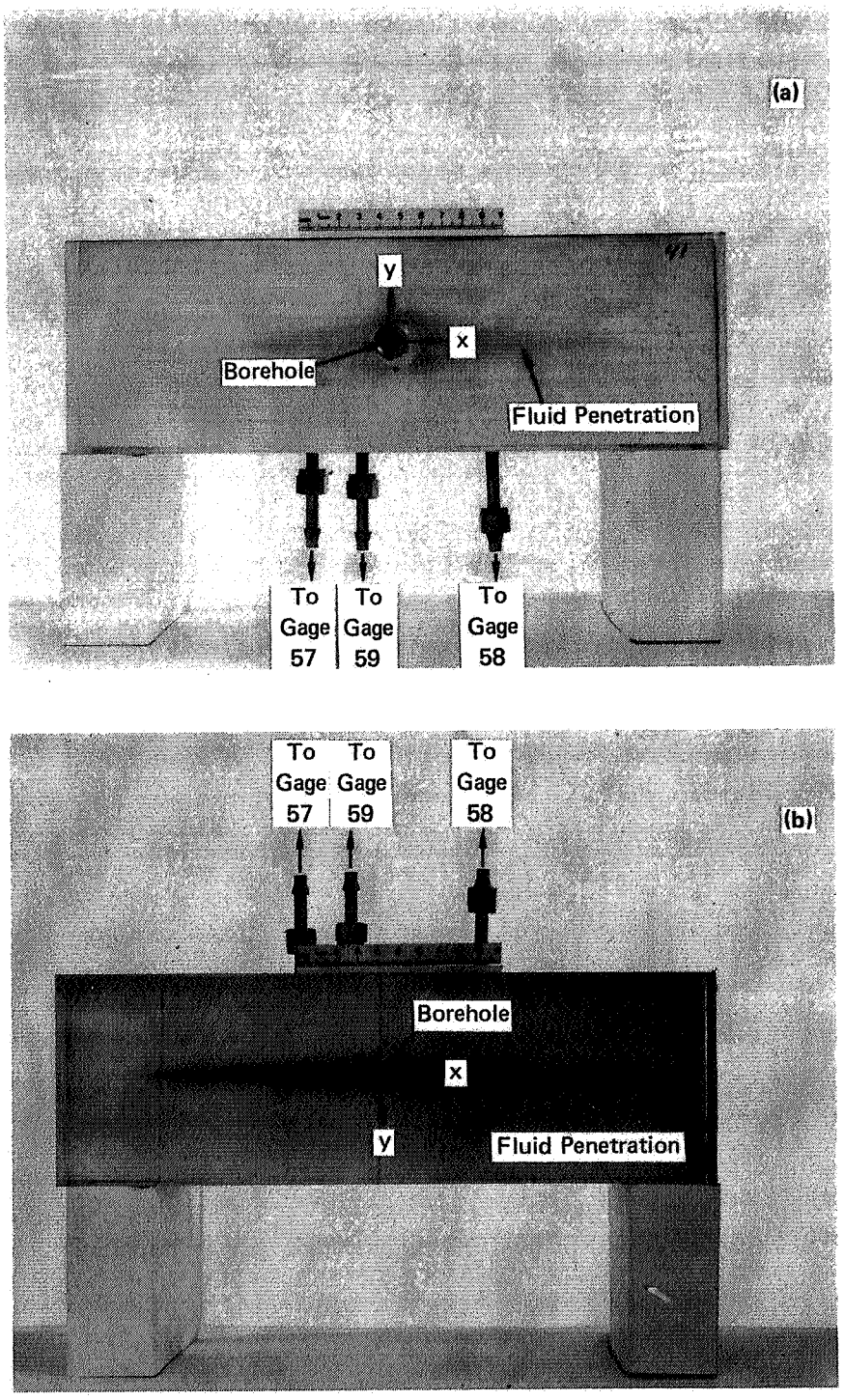

MP-8975-92

FIGURE 43 PHOTOGRAPHS OF THE FLUID PENETRATION IN MODEL 41 (no proppants) AS VIEWED FROM (a) THE TOP, AND (b) THE BOTTOM; TAKEN AFTER COMPLETION OF THE EXPERIMENT

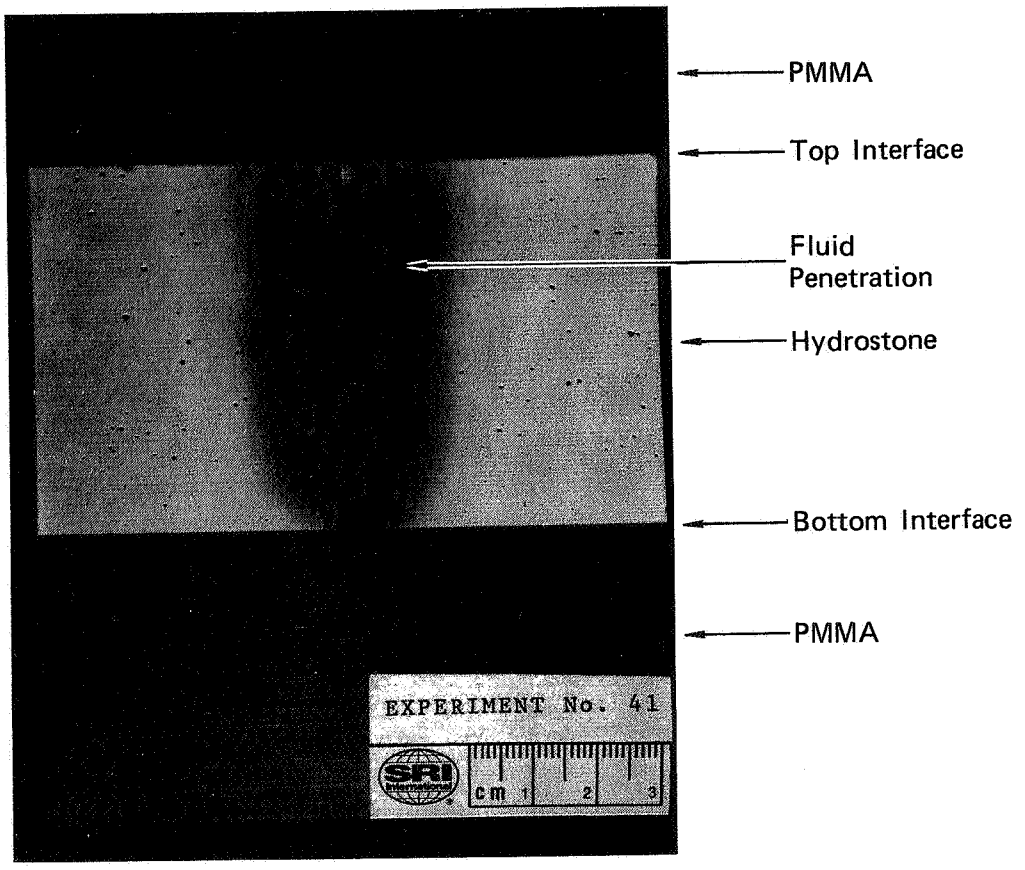

MP-8975-105

FIGURE 44 CROSS SECTION OF MODEL 41 (no proppants), THROUGH THE PLANE 4.2 mm FROM THE BOREHOLE CENTER, SHOWING THE VERTICAL VARIATION OF FLUID PENETRATION

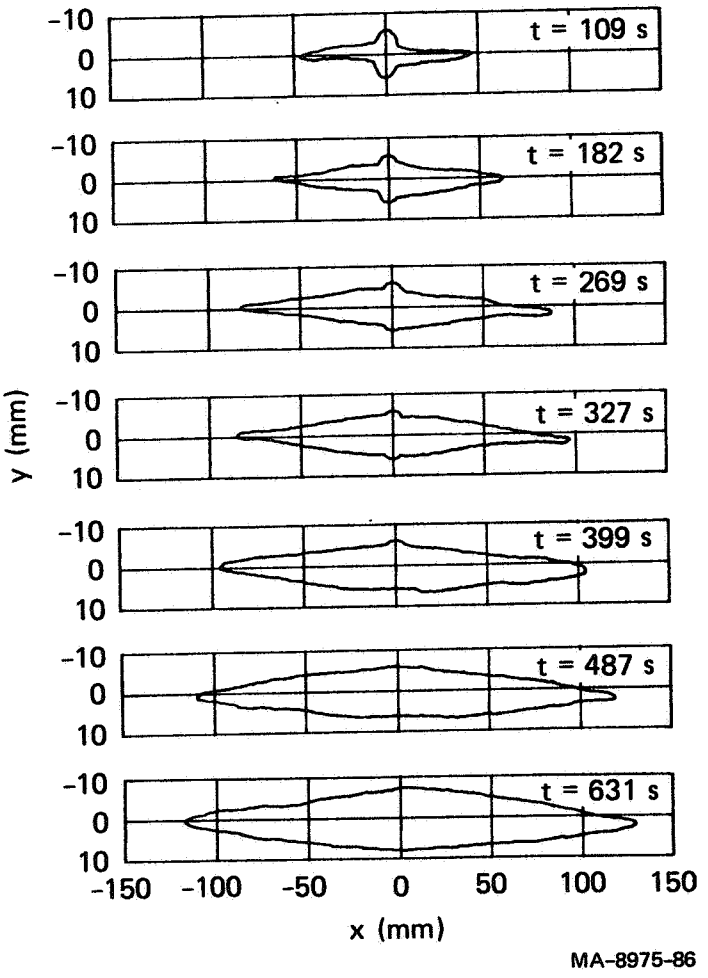

FIGURE 45 FLUID PENETRATION CONTOURS AT SEVERAL TIMES DURING THE FRACTURE OF MODEL 41 (no proppants) AS VIEWED FROM THE BOTTOM OF THE MODEL

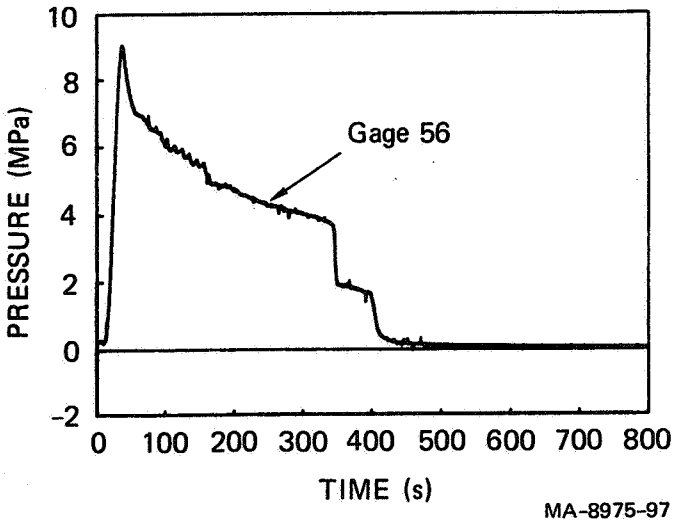

FIGURE 46 PRESSURE IN GAGE 56 DURING THE FRACTURE OF MODEL 46 (no proppants)

Table 9

QUANTITATIVE DATA TAKEN AT SEVERAL TIMES DURING THE FRACTURE OF MODEL 46[a] (pumping started at t = 11.0 s)

Time (s)	Gage 56 (MPa)	Gage 57 (MPa)	Gage 58 (MPa)	Gage 59 (MPa)	LVDT (μm)	X_1 (mm)	X_2 (mm)	ℓ (mm)
52.5	7.24	0.088	-0.017	0.142	17	- 5	14	10
69.5	6.83	0.088	-0.020	0.889	23	-18	21	19
86.5	6.48	-0.008	-0.020	3.435	28	-23	24	24
112.5	5.98	-0.008	-0.020	3.521	36	-31	30	31
138.5	5.56	-0.008	-0.023	3.746	44	-34	33	34
164.5	5.09	-0.008	-0.020	3.480	49	-40	42	41
190.5	4.84	0.003	-0.020	3.489	53	-43	44	44
225.5	4.48	1.025	-0.020	3.486	60	-43	47	45
260.0	4.25	1.940	-0.020	3.492	65	-47	57	52
294.5	4.06	2.285	-0.014	3.492	70	-52	60	56
329.5	3.82	2.451	-0.014	3.406	75	-54	66	60

[a]For error estimates see Table 2 and the discussion in Section 3.2.

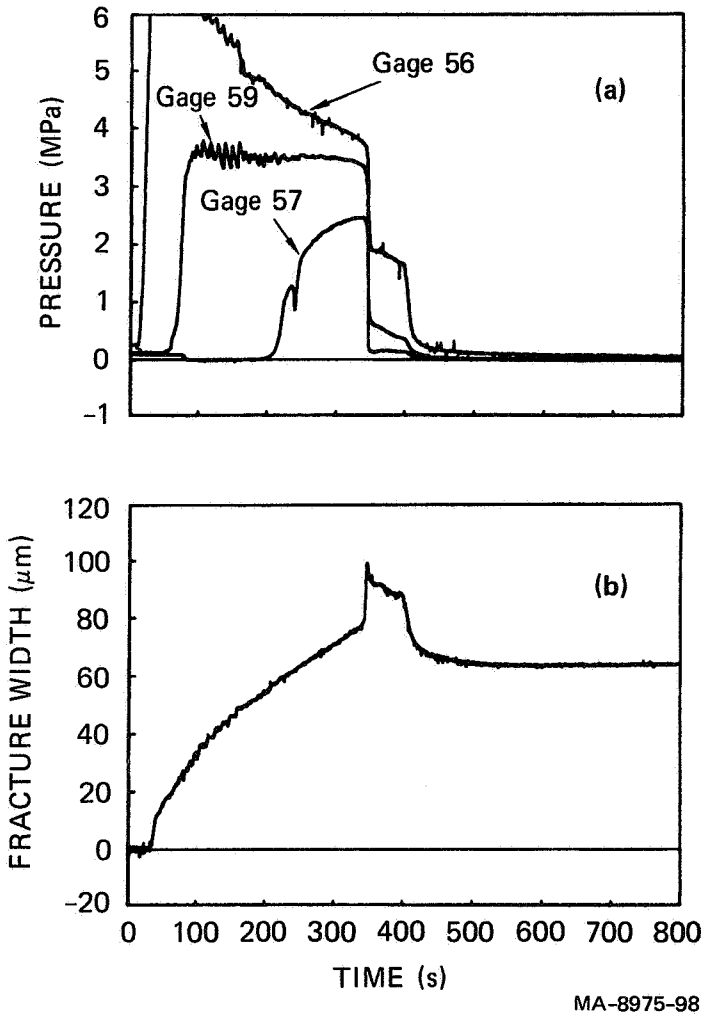

FIGURE 47 FRACTURE OF MODEL 46 (no proppants):
(a) PRESSURES IN GAGES 56, 57, AND 59;
(b) FRACTURE WIDTH.

Table 10

QUANTITATIVE DATA TAKEN AT SEVERAL TIMES
DURING THE FRACTURE OF MODEL 47[a]
(pumping started at t = 13.0 s)

Time (s)	Gage 56 (MPa)	Gage 57 (MPa)	Gage 58 (MPa)	Gage 59 (MPa)	LVDT (μm)	X_1 (mm)	X_2 (mm)	ℓ (mm)
110.5	5.59	0.059	0.011	0.545	31	-23	22	23
131.5	5.31	0.059	0.011	3.465	37	-28	27	27
158.5	4.95	0.056	0.008	3.711	43	-31	34	33
183.0	4.75	0.062	0.008	3.720	47	-34	36	35
216.5	4.57	0.167	0.025	3.690	51	-39	39	39
249.5	4.48	1.663	0.084	3.702	55	-45	45	45
274.5	4.39	2.239	0.265	3.705	57	-49	47	48
299.5	4.34	2.465	2.120	3.696	61	-51	49	50
333.0	4.17	2.615	2.489	3.586	65	-57	54	56

[a]For error estimates see Table 2 and the discussion in Section 3.2.

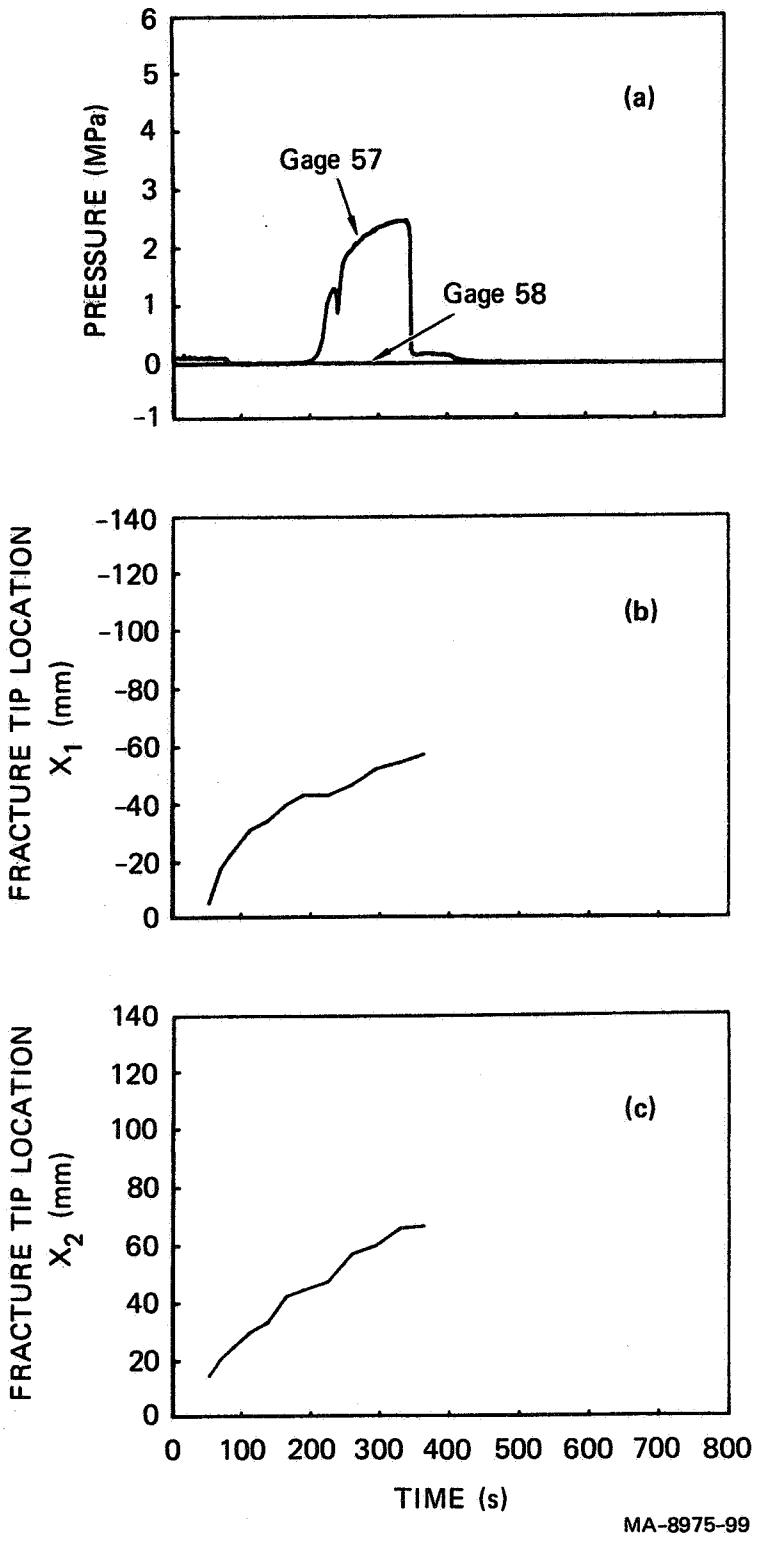

FIGURE 48 FRACTURE OF MODEL 46 (no proppants):
(a) PRESSURES IN GAGES 57 AND 58;
(b) FRACTURE TIP LOCATION X_1;
(c) FRACTURE TIP LOCATION X_2.

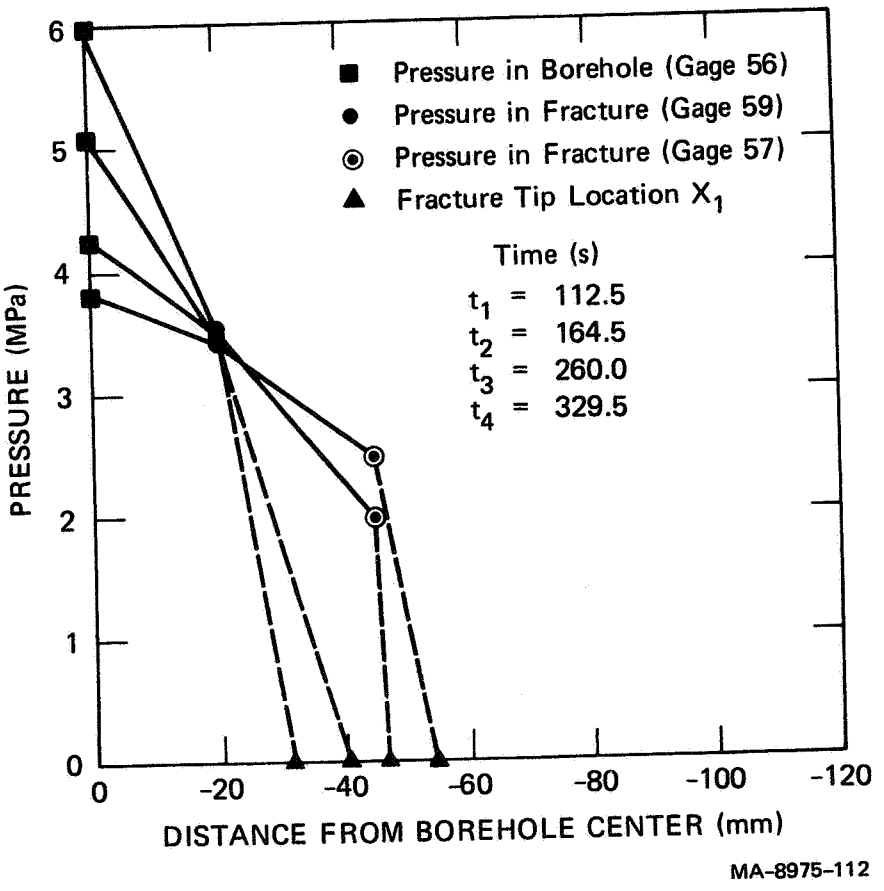

FIGURE 49 PRESSURE DISTRIBUTIONS AT SEVERAL TIMES DURING THE FRACTURE OF MODEL 46 (no proppants)

Pumping started at t = 11.0 s.

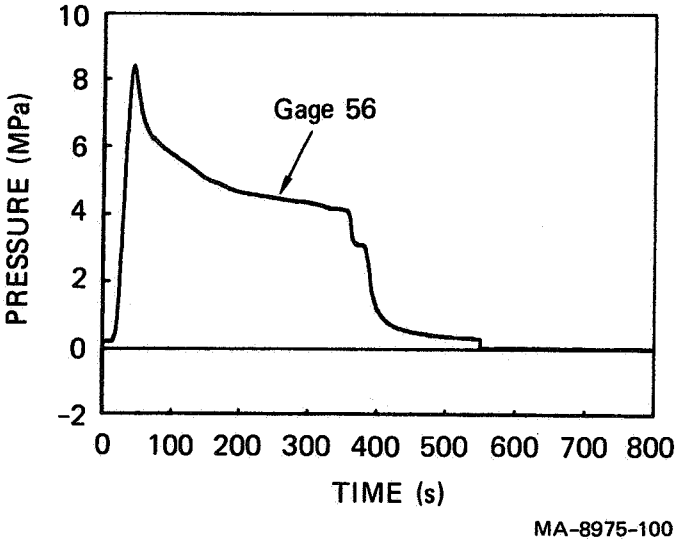

FIGURE 50 PRESSURE IN GAGE 56 DURING THE FRACTURE OF MODEL 47 (no proppants)

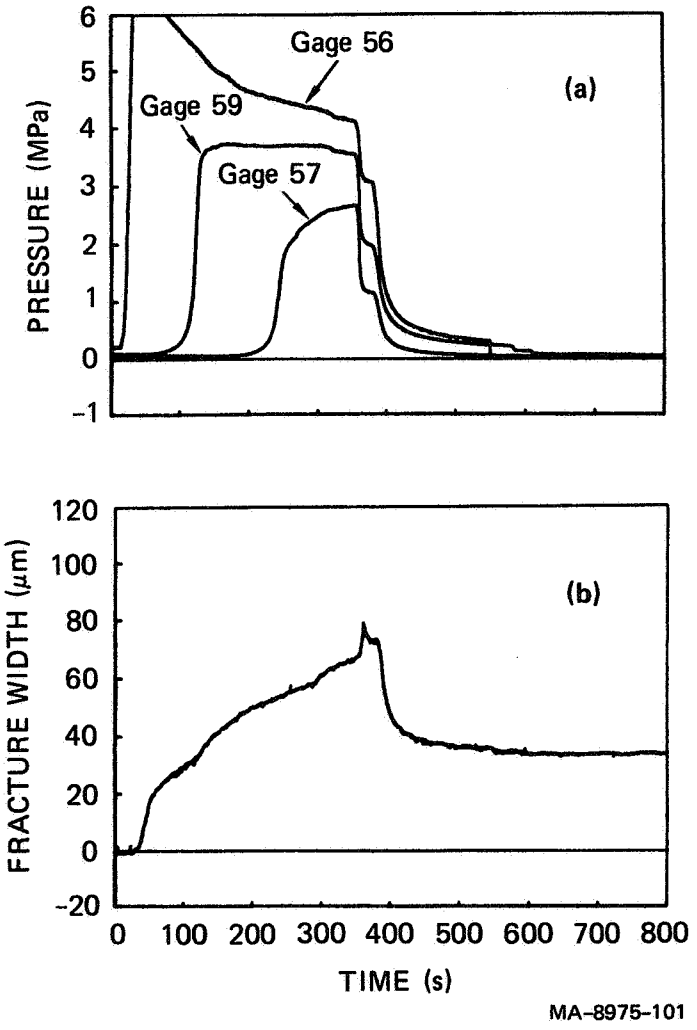

FIGURE 51 FRACTURE OF MODEL 47 (no proppants):
(a) PRESSURES IN GAGES 56, 57, AND 59;
(b) FRACTURE WIDTH.

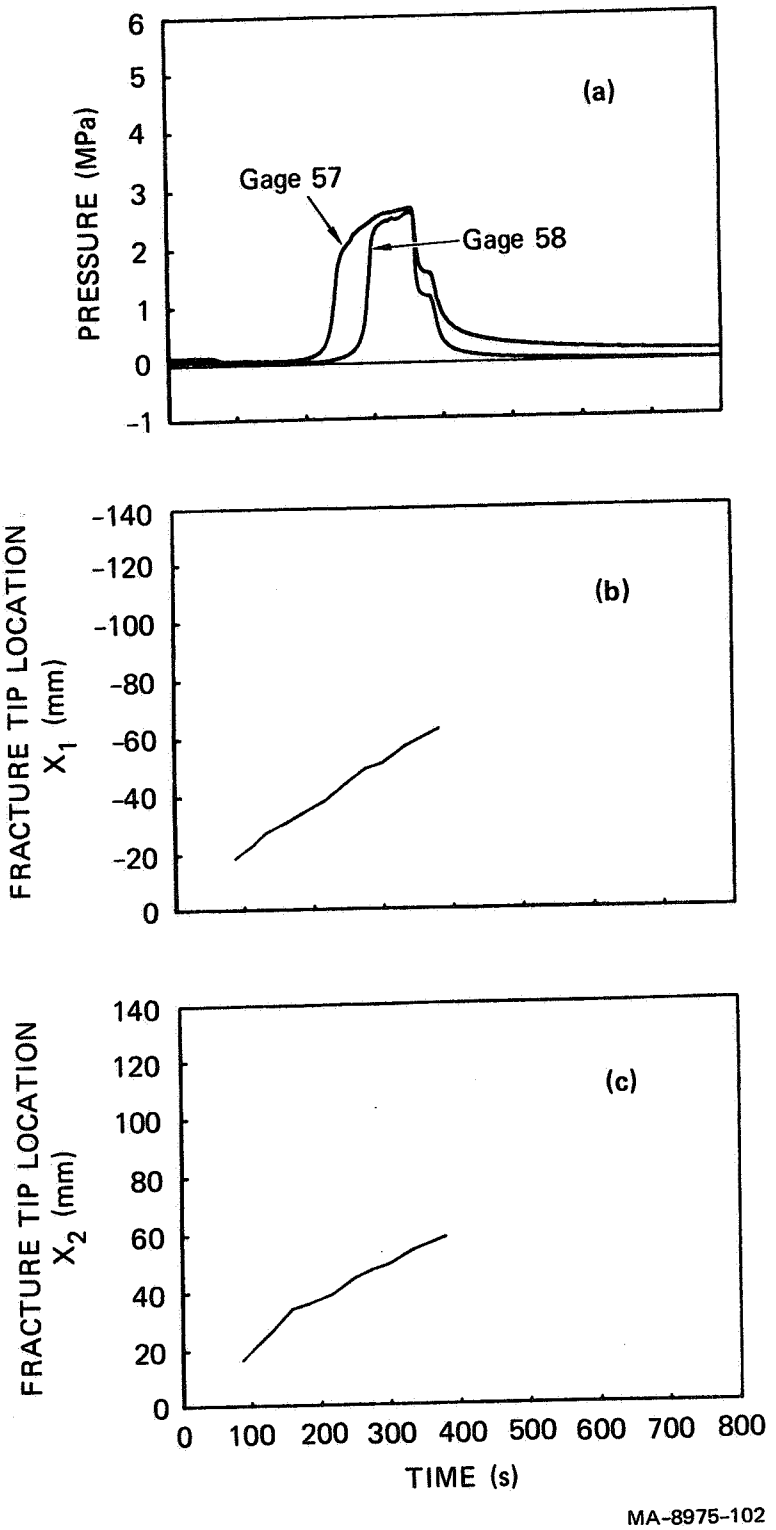

FIGURE 52 FRACTURE OF MODEL 47 (no proppants):
(a) PRESSURES IN GAGES 57 AND 58:
(b) FRACTURE TIP LOCATION X_1;
(c) FRACTURE TIP LOCATION X_2.

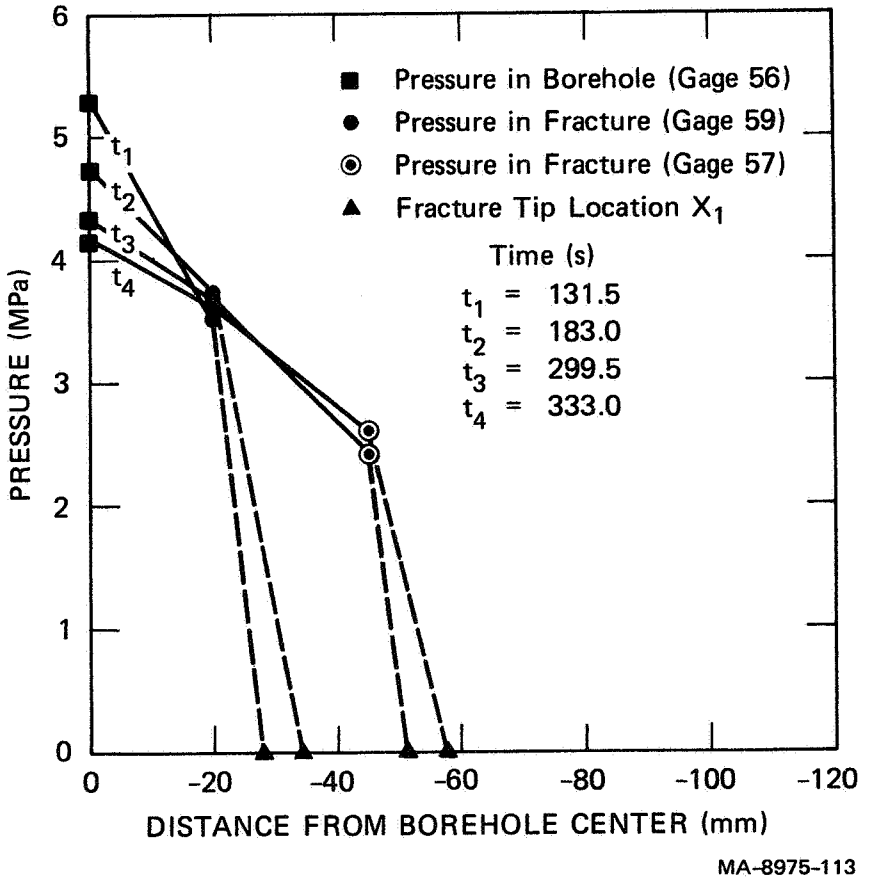

FIGURE 53 PRESSURE DISTRIBUTIONS AT SEVERAL TIMES DURING THE FRACTURE OF MODEL 47 (no proppants)

Pumping started at t = 13.0 s.

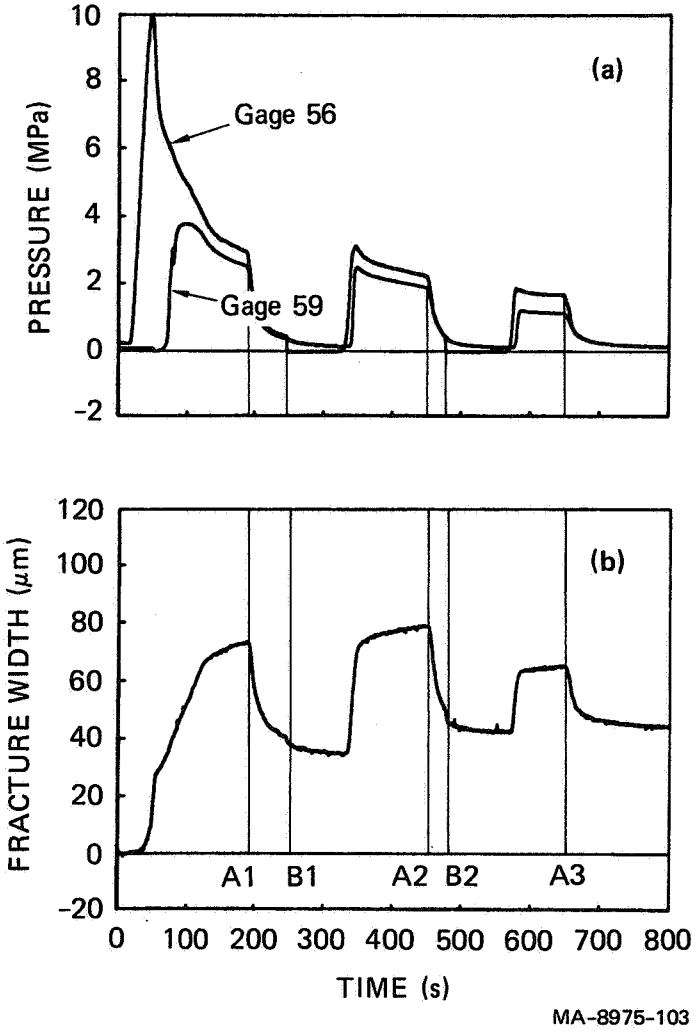

FIGURE 54 FLOW-CYCLE TREATMENT OF MODEL 50 (no proppants):

(a) PRESSURES IN GAGES 56 AND 59;
(b) FRACTURE WIDTH

Points A1, A2, and A3 denote the times when pumping was stopped and points B1 and B2 denote the times when the pressure was relieved in the borehole.

drop. Furthermore, from the movie of Experiment 46 we observed that at t = 362.0 s the fracture reaches the front face of the hydrostone. This time also correlates well with the time of the sharp drop in the borehole pressure. Model 47 did not debond but at t = 355.0 s, the fracture reached the front face of the hydrostone.

The borehole pressure (Gage 56) and the pressures at different locations in the fracture (Gages 57 and 59) are shown in Figures 40(a), 47(a), and 51(a). These figures show the pressure gradient in the fracture as a function of time. The fracture width is recorded by Figures 40(b), 47(b), and 51(b). Notice from Figures 47 and 51 that the pressure in the fracture fell sharply and the fracture width increased sharply when the fracture reached the front faces of the hydrostone. This is a strong indication that the gages were working properly.

The degree of symmetry of the fracture propagation is shown in Figures 41(a), 48(a), and 52(a) where the pressure records from Gages 57 and 58 (located equidistant from the borehole and on opposite sides of it) are compared. Another measure of the symmetry of fracture propagation can be obtained by comparing the values of the fracture tip locations X_1 and X_2 that were determined from the films. The values of X_1 are plotted in Figures 41(b), 48(b), and 52(b), and the values of X_2 are plotted in Figures 41(c), 48(c), and 52(c). In Experiment 46, there was a problem with Gage 58 because it did not record a pressure increase even when the fracture tip passed it. In Experiment 46, the fluid started leaking into the interface from the fracture tip location X_1. It is interesting to note that the flat spot in the fracture tip location record X_1 in Figure 48(b) occurs at about the same time that the film recorded the fluid leaking into the interface (t = 171.0 s).

Tables 8, 9, and 10 summarize quantitative values for the fracture pressures, fracture width, and fracture tip locations X_1 and X_2 for several times. Also included is the average fracture half-length ℓ defined by formula (2.1). Furthermore, we note that pumping started at t = 10.5 s, 11.0 s, and 13.0 s in Experiments 41, 46 and 47, respectively. Using the quantitative data in Tables 8, 9, and 10, we

constructed Figures 42, 49, and 53, which show the pressure distribution in the fracture at several times. In these figures, it has been assumed that the pressure at the fracture tip is zero. Therefore, broken lines have been used to connect the fracture tips to measured pressure values, and solid lines have been used to connect measured pressure values with other measured values.

Photographs of the fluid penetration contours in model 41 were taken after completion of the experiment. The photographs of the top and bottom surfaces of model 41 are shown in Figure 43. From Figure 43, we observe that the penetration contour at the top surface of the model is shorter and wider than the contour at the bottom surface. The vertical variation of the extent of fluid penetration was investigated by sectioning model 41 through the y-z plane located 4.2 mm from the borehole center. Figure 44 shows a photograph of this cross section. Note that in this cross section, the vertical variation of the fluid penetration is negligible except near the top and bottom hydrostone-PMMA interfaces. The fluid penetrated deeper into the hydrostone at distances away from the interface. Furthermore, the perturbation of the fluid penetration caused by the PMMA disc at the bottom of the borehole (see Figure 37) is expected to diminish at distances from the borehole.

Fluid penetration contours at several times during the fracture of model 41 were obtained from the movie of Experiment 41 and are plotted in Figure 45. For the earlier times ($t < 487$ s) the fluid penetration at the borehole ($x = o$, $y = o$) was obscured by the PMMA disc (see Figure 37) so we traced around the disc instead of interpolating the location of the fluid penetration near the borehole.

In Experiment 48, we investigated the effects of increasing the viscosity of the fracturing fluid by using Dow Corning 200 fluid (100,000 centistoke). The fracture propagated much more rapidly in Experiment 48 than in the experiments in which the 1,000-centistoke fluid was used because much less fluid leaked into the hydrostone when the highly viscous fluid was used. No quantitative data from this experiment are reported because the fracture reached the front face of

the hydrostone layer early in the experiment and because the fluid did not penetrate deeply enough to determine the fracture tip locations from the movie.

The effects of flow-cycle treatment were investigated in Experiment 50 by pressurizing the model, relieving the pressure, then repressurizing it. Figure 54(a) shows the borehole pressure (Gage 56) and the pressure in the fracture (Gage 59), while Figure 54(b) shows the corresponding fracture width. The points A1, A2, and A3 denote the times when pumping stopped and the points B1 and B2 denote the times when the pressure was momentarily relieved in the borehole. Near the end of the first pressurization, fluid began leaking into the bottom interface. At this point, we stopped pumping (Point A1), relieved the pressure (Point B1), then repressurized. Notice that on the second pressurization, the borehole pressure, pressure in the fracture, and fracture width returned to about the same values they had at the end of the first pressurization. At point A2, the pumping was again stopped and at point B2, the pressure was relieved. On the third pressurization, the borehole pressure, pressure in the fracture, and fracture width did not return to the same values they had at the end of the second pressurization because the volume of fluid leaking into the hydrostone-PMMA interface increased and the interface began to debond.

3.4 Main Permeable Experiments With Proppants

Several attempts were made to propagate a fracture with a slurry as a fracturing fluid. In Experiment 42, the borehole was filled with slurry I (described in Section 3.2) just before pressurizing the model. Figure 55(a) shows the pressure in the borehole (Gage 56) and the pressure measured at two locations in the fracture (Gages 57 and 59), and Figure 55(b) shows the fracture width. The borehole pressure was much higher than that associated with the experiments without proppants, and the pressure increased as the fracture propagated instead of decreased. Since the fracture width was between 30 and 50 μm and the minimum proppant diameter was 43 μm for fly ash I, most of the proppants must

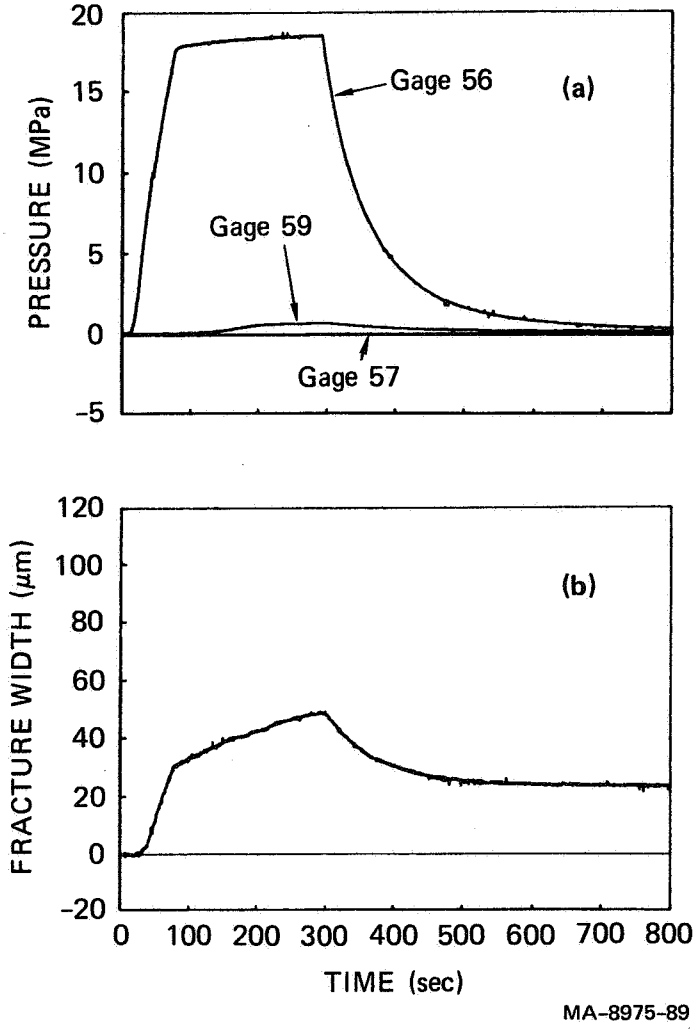

FIGURE 55 FRACTURE OF MODEL 42 (with proppants):
(a) PRESSURES IN GAGES 56, 57, AND 59;
(b) FRACTURE WIDTH.

have been screened out at the borehole. This explains the fact that the borehole pressure was high and the pressure gradient in the fracture was so steep (Gage 59 remained at a low pressure level relative to that of Gage 56).

Figure 56(a) shows that the fracture did not reach either of the Gages 57 or 58, and Figures 56(b) and 56(c) show the plots of the fracture tip locations X_1 and X_2, respectively. The fracture tip locations X_1 and X_2 were not determined for earlier times because the fracture tip was difficult to see in the film since the fluid penetration was so much less than that observed in the experiments without proppants.

Quantitative values for the fracture pressures, fracture width, and fracture tip locations X_1 and X_2 for several times are summarized in Table 11. Also, included in this table is the average fracture half-length ℓ defined by formula (2.1). Furthermore, we note that pumping started at t = 12.0 s in Experiment 42. Using the quantitative data in Table 11, we constructed Figure 57, which shows the pressure distribution in the fracture at three times. In this figure, it has been assumed that the pressure at the fracture tip is zero. Therefore, broken lines have been used to connect the fracture tips to measured pressure values, and solid lines have been used to connect measured pressure values with other measured values.

An attempt was made to study a flow-cycle treatment by letting model 42 sit overnight unpressurized and then repressurizing it in the morning (about 17 hours later). During this time, the proppants settled to the bottom of the borehole, and when the model was repressurized, the pressure reached about 35 MPa (the limit of Gage 56) without propagating the original fracture. Proppants were then removed from the borehole, and the borehole was refilled with clear fracturing fluid (1000-centistoke fluid). On repressurization, the borehole pressure rose to about 20 MPa at which time the fracture began to propagate. The pressure continued to rise to about 23 MPa, then the fracture changed its orientation and reached the front face of the hydrostone instead of maintaining a vertical orientation.

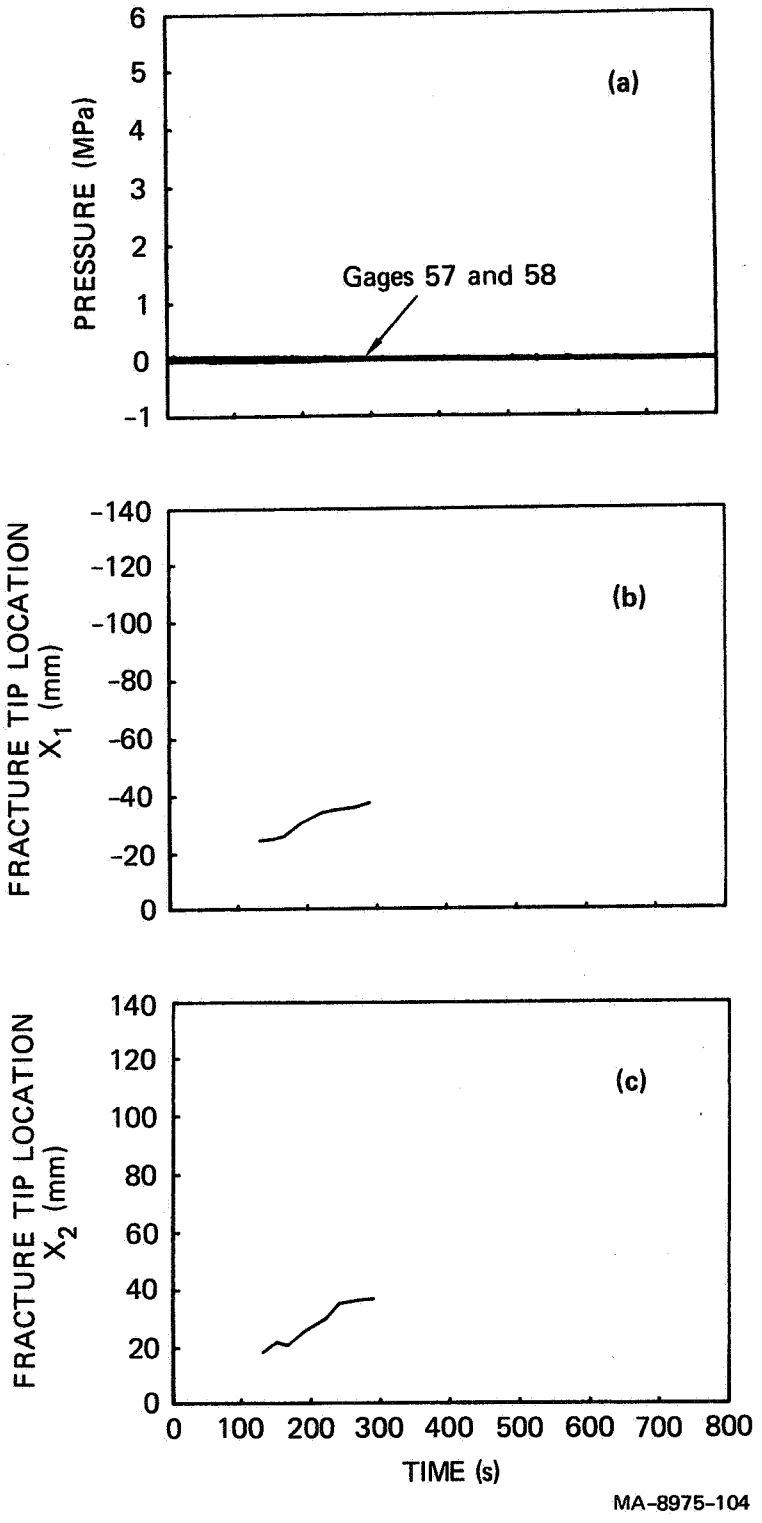

FIGURE 56 FRACTURE OF MODEL 42 (with proppants):
(a) PRESSURES IN GAGES 57 AND 58;
(b) FRACTURE TIP LOCATION X_1;
(c) FRACTURE TIP LOCATION X_2.

Table 11

QUANTITATIVE DATA TAKEN AT SEVERAL TIMES
DURING THE FRACTURE OF MODEL 42 (WITH PROPPANTS)
(pumping started at t = 12.0 s)

Time (s)	Gage 56 (MPa)	Gage 57 (MPa)	Gage 58 (MPa)	Gage 59 (MPa)	LVDT (μm)	X_1 (mm)	X_2 (mm)	ℓ (mm)
131.0	18.10	-0.011	0.062	0.169	36	-25	18	22
150.0	18.18	-0.011	0.056	0.258	38	-25	22	24
189.0	18.32	-0.008	0.051	0.531	41	-30	25	28
222.5	18.41	-0.008	0.048	0.631	44	-34	30	32
241.5	18.45	-0.008	0.048	0.655	46	-35	35	35
290.0	18.50	0.008	0.039	0.700	49	-38	37	37

[a]For error estimates see Table 2 and the discussion in Section 3.2.

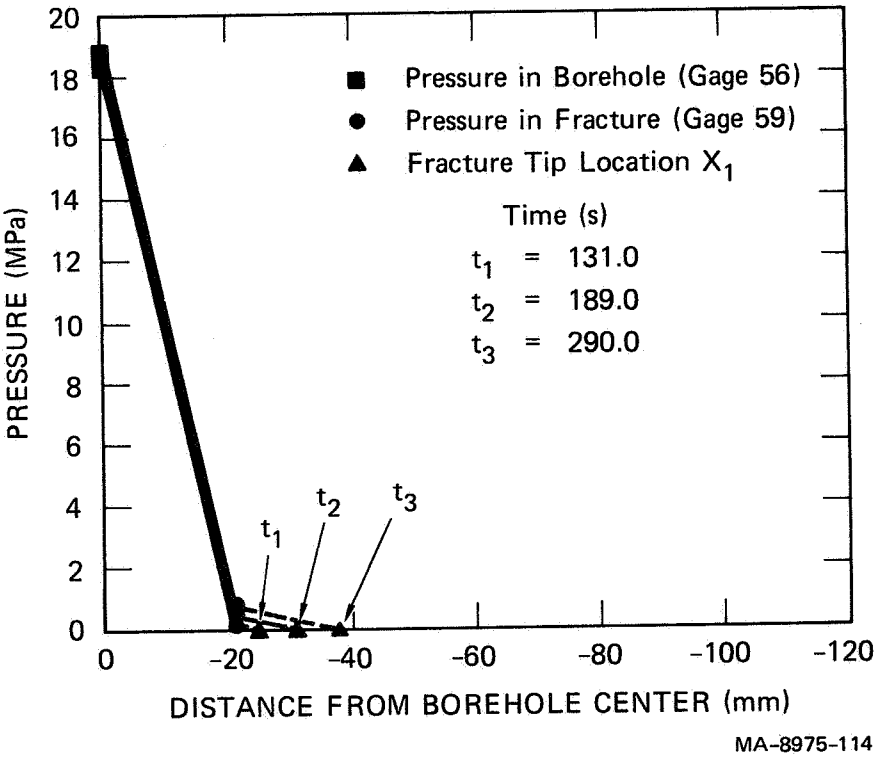

FIGURE 57 PRESSURE DISTRIBUTIONS AT SEVERAL TIMES DURING THE FRACTURE OF MODEL 42 (with proppants)

Pumping started at t = 12.0 s.

To reproduce the results of Experiment 42, we conducted Experiment 45, using model 45 and slurry I as a fracturing fluid. This time the borehole pressure rose to about 35 MPa, and a three-tipped fracture was created. Figure 58 is a photograph of the top and bottom of model 45. During the test, the borehole pressure was relieved to zero, then the model was repressurized to simulate a flow-cycle treatment. The borehole pressure returned to 35 MPa so the experiment was terminated.

Another attempt was made to study effects of proppants by using a smaller proppant size (slurry II) in Experiment 51. It was hoped that the smaller proppants would be able to enter the fracture and thus reduce the screening effect that produced the large borehole pressures observed in Experiments 42 and 45. This proved to be relatively ineffective because the borehole pressure quickly rose to about 19 MPa, then the model fractured with little vertical fracture propagation.

In another attempt to study the effects of proppants, we used a pad volume of fluid in Experiment 52 before pumping slurry II. Recall that the pad volume of fluid is the clear fracturing fluid that precedes the proppant slurry. The beginning of Experiment 52, in which clear 1,000-centistoke fluid was used as a fracturing fluid, was typical of the experiments without proppants in that the borehole pressure reached a peak of about 9.5 MPa and decayed as the fracture propagated. After propagating a vertical fracture for some distance, we relieved the pressure in the borehole and refilled the borehole with slurry II. When model 52 was repressurized with slurry II, the borehole pressure oscillated wildly between about 2 to 8 MPa, then the fracture reached the front face of the hydrostone layer.

The results of these experiments suggest that the borehole pressure and pressure gradient in the fracture are significantly greater in the experiments with proppants than in the experiments without proppants. However additional technique development will be required to maintain the vertical orientation of the fracture long enough for a sufficient quantity of proppants to be pumped into the borehole. This development

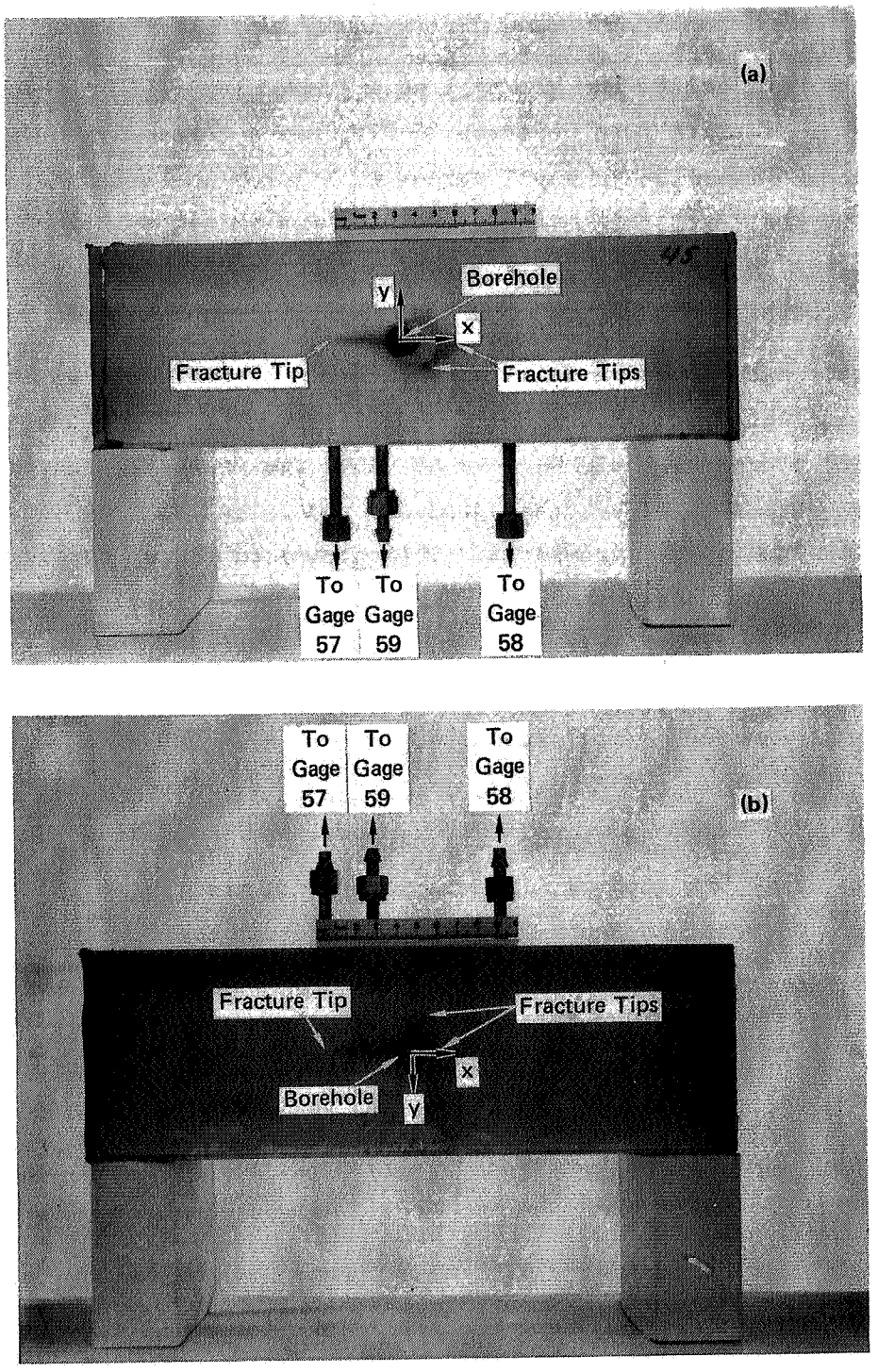

FIGURE 58 PHOTOGRAPHS OF THE THREE-TIPPED FRACTURE IN MODEL 45 (with proppants) AS VIEWED FROM (a) THE TOP, AND (b) THE BOTTOM; TAKEN AFTER COMPLETION OF THE EXPERIMENT

might require the use of larger models or even triaxial loading of the model.

3.5 Interpretation and Analysis

In this section, we compare the predictions of several simple solutions used to analyze the propagation of vertical hydraulic fractures with the experimental results reported in the last two sections. However, before comparing theory with experiment, it is interesting to compare the results of the experiments without proppants with the experiments with proppants. Figure 59 shows plots of the borehole pressure P_b versus the average fracture half-length ℓ measured in experiments without proppants (Experiments 41, 46, and 47) and Experiment 42 (with proppants). The results of the experiments without proppants lie very close together. However, the borehole pressure measured in the experiment with proppants is significantly greater than that measured in the experiments without proppants. Furthermore, the borehole pressure in the experiments with proppants increased with increasing fracture length, whereas the borehole pressure in the experiment without proppants decreased with increasing fracture length.

Using the formulas of Appendix A, the present solution (R) and the solutions of Nordgren (N) and Geertsma and de Klerk (GK) were evaluated for the hydraulic fracture treatment associated with Experiment 41. Figures 60, 61, and 62 compare the predictions of the borehole pressure P_b, the fracture width at the borehole w_b, and the average fracture half-length ℓ, respectively, with corresponding measurements taken in Experiment 41.

From Figure 60, we observe that the solutions (R) and (GK), which assume plane strain in horizontal planes, predict the trend of the borehole pressure measured in Experiment 41 (i.e., the borehole pressure decreases with increasing fracture length), whereas the solution (N), which assumes plane strain in vertical planes, predicts the opposite trend of the pressure P_b in Experiment 41 (i.e., the pressure P_b increases with increasing fracture length). Figure 61 shows that the

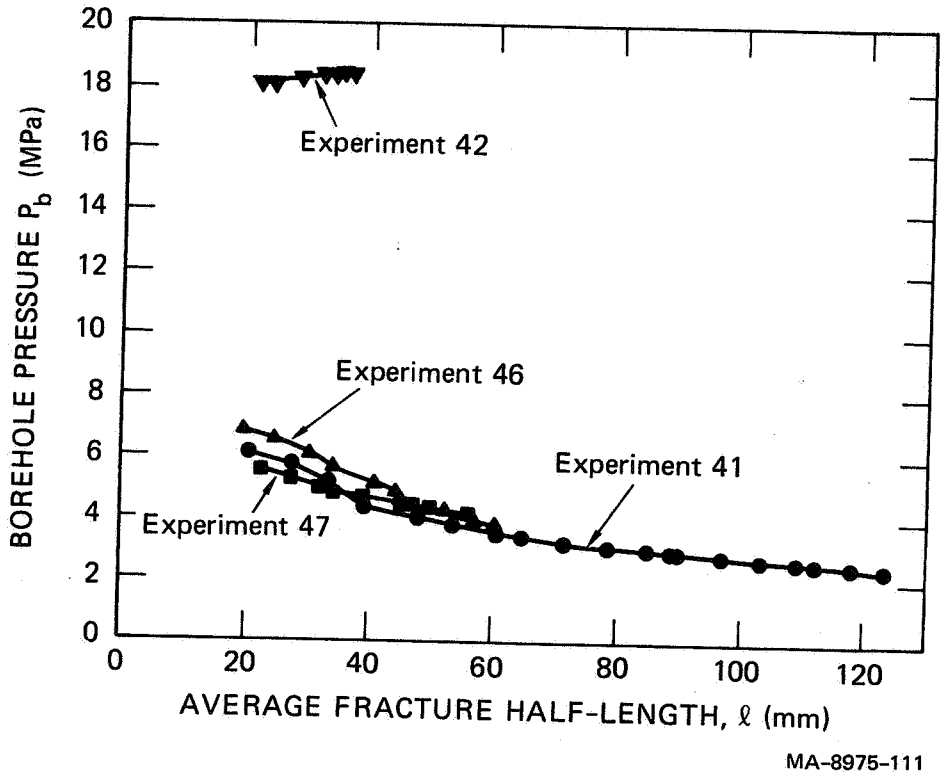

FIGURE 59 BOREHOLE PRESSURE P_b MEASURED IN EXPERIMENTS WITHOUT PROPPANTS (Experiments 41, 46, 47) AND EXPERIMENT 42 WITH PROPPANTS

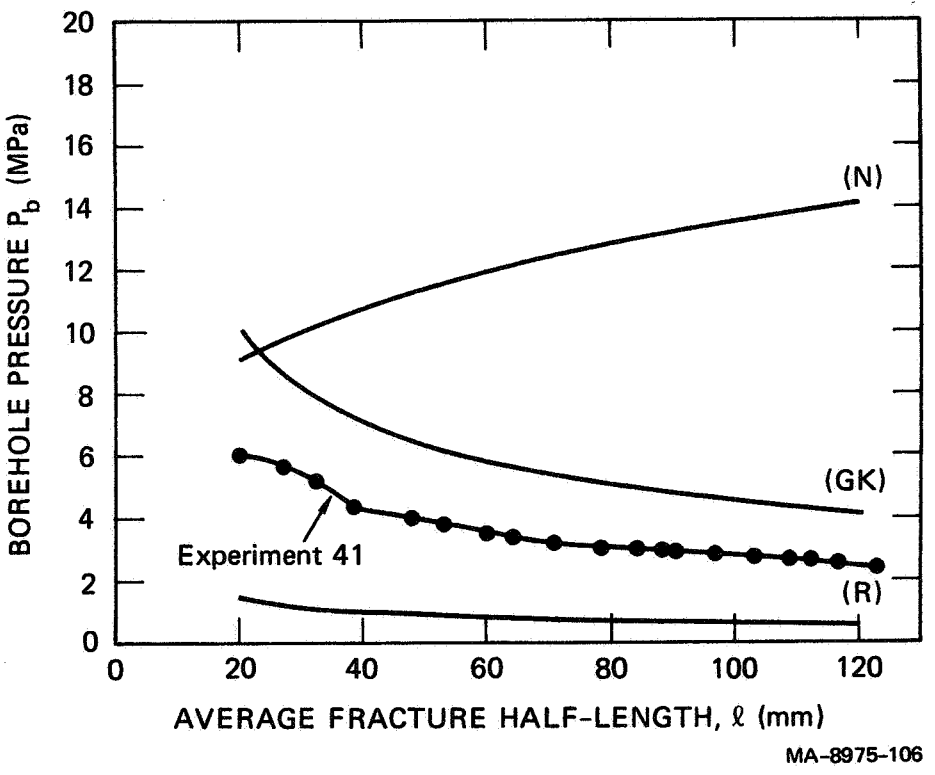

FIGURE 60 BOREHOLE PRESSURE P_b MEASURED IN EXPERIMENT 41 AND PREDICTED BY THE PRESENT SOLUTION (R) AND THE SOLUTIONS OF NORDGREN (N) AND GEERTSMA AND de KLERK (GK)

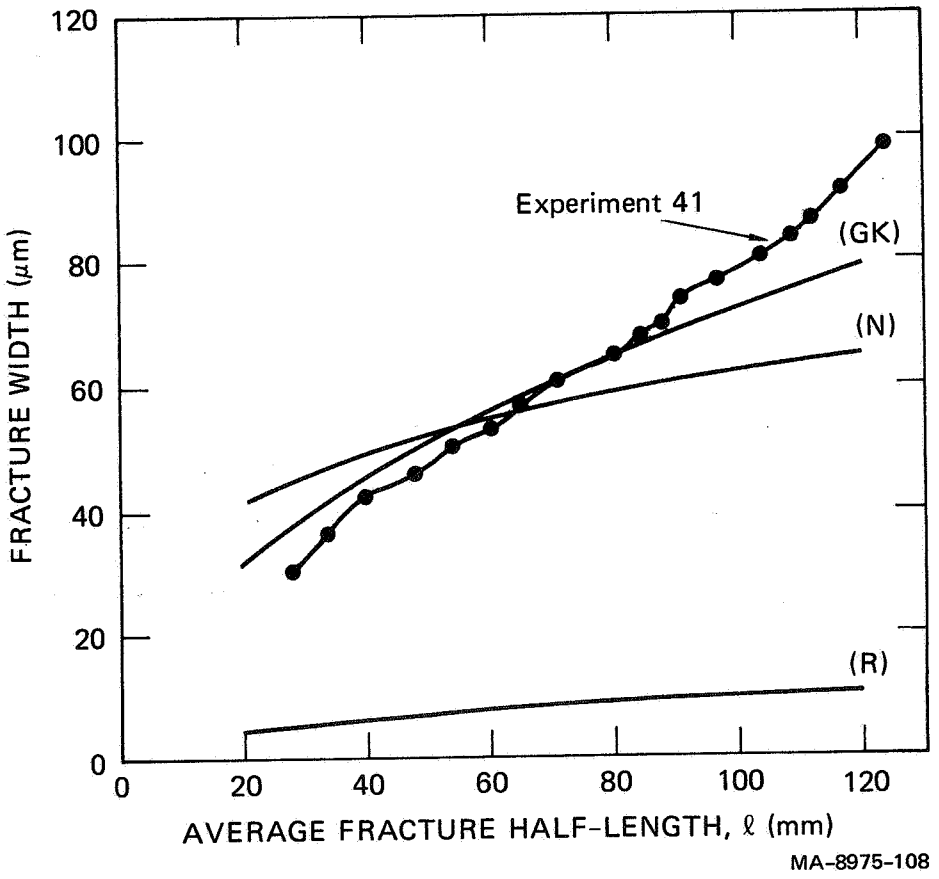

FIGURE 61 BOREHOLE FRACTURE WIDTH w_b PREDICTED BY THE PRESENT SOLUTION (R) AND THE SOLUTIONS OF NORDGREN (N) AND GEERTSMA AND de KLERK (GK)

Also included is the fracture width w measured in Experiment 41 at a location 10 mm from the borehole center.

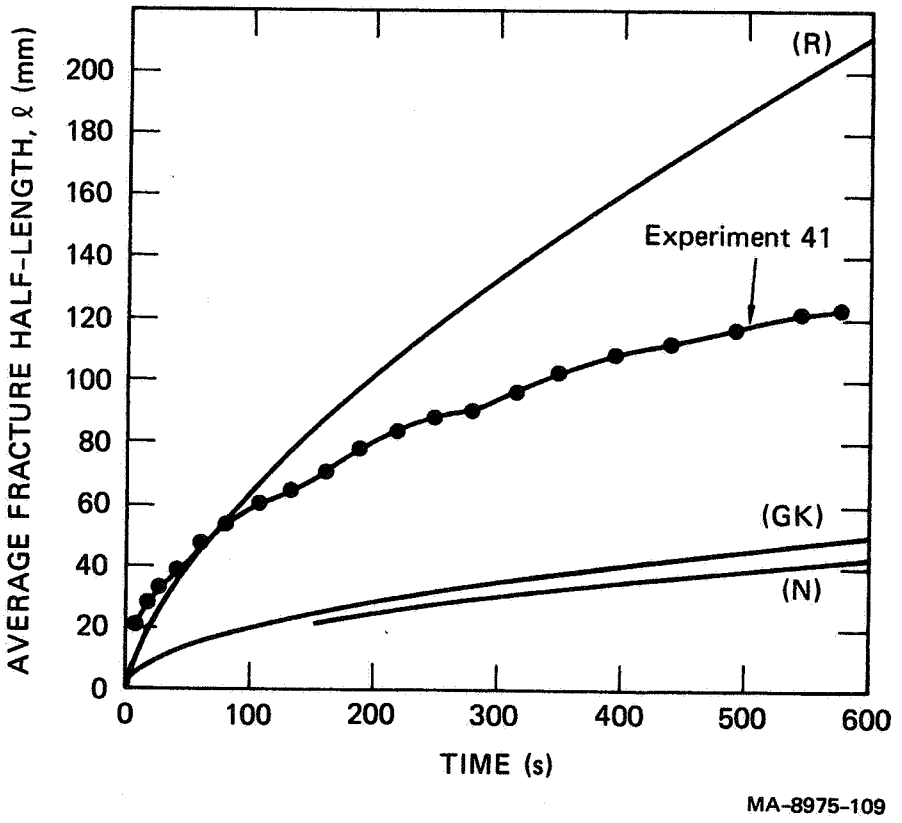

FIGURE 62 AVERAGE FRACTURE HALF-LENGTH MEASURED IN EXPERIMENT 41 AND PREDICTED BY THE PRESENT SOLUTION (R) AND THE SOLUTIONS OF NORDGREN (N) AND GEERTSMA AND de KLERK (GK)

In this graph, the zero time for Experiment 41 has been chosen to correspond to the time when fracture initiated in the actual experiment; i.e. the time t = 48.5 s when the borehole pressure (Gage 56) reached its peak value.

fracture width predicted by the solutions (N) and (GK) lie close to the experimental measurement of fracture width (at a distance 10 mm from the borehole center), but the prediction of solution (R) lies well below the experimental values. The predictions of the average fracture half-length in Figure 62 show that the solutions (GK) and (N) underestimate the measured values, whereas the solution (R) overestimates the measured values.

From Figure 60, we observe that the borehole pressure predicted by the present solution (R) is significantly lower than that measured in Experiment 41. Recall from Appendix A that in the development of the present solution (R), it is assumed that the formation is an infinite medium and that the pressure in the fracture P is spacially uniform. As discussed below, we believe that the changes caused by removing each of these assumptions are not great enough to explain the fact that the pressure measured in Experiment 41 is greater than that predicted by the present solution (R).

First, we observe from Figure 29 of Section 2.3 that including the effect of the finite dimensions of our hydrofracture model tends to reduce the value of the critical pressure for fracture extention. Therefore, this effect would tend to increase the discrepancy between the values of the borehole pressure P_b predicted by the solution (R) and measured in Experiment 41 instead of decreasing the discrepancy.

Second, the effect of a pressure gradient in the fracture will tend to increase the borehole pressure for a given fracture length and thus tend to decrease the discrepancy between theory and experiment. The magnitude of this effect can be estimated by determining the critical pressure for fracture propagation associated with a pressure distribution that decays linearly from P_b at the borehole to zero at the fracture tip. To plot the middle curve in Figure 63 (associated with a linearly pressurized fracture), we evaluated the expression (2.6) in the limit of the quantity a approaching zero. Also included in Figure 63 are the borehole pressures measured in Experiment 41 and predicted by solution (R) associated with a uniformly pressurized fracture. From

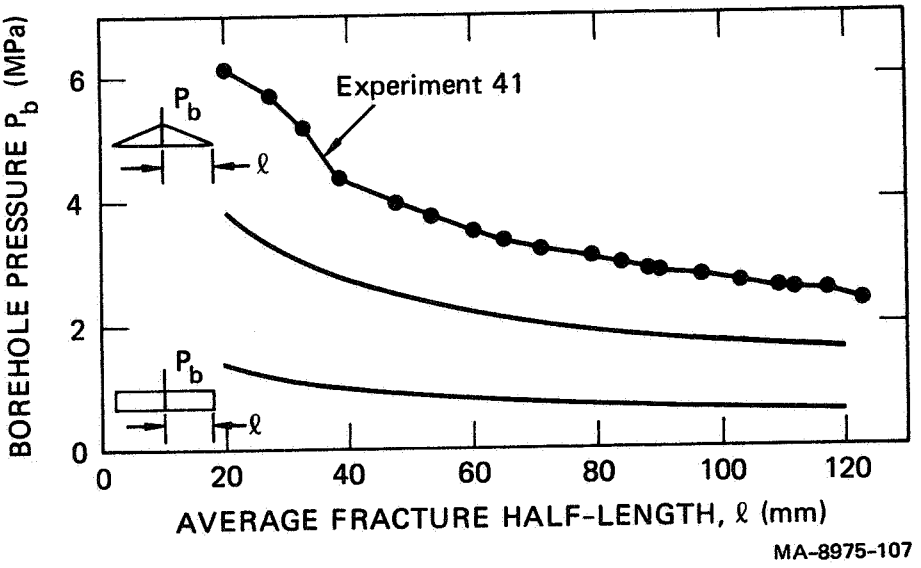

FIGURE 63 BOREHOLE PRESSURE P_b MEASURED IN EXPERIMENTS 41 AND PREDICTED FOR FRACTURES PRESSURIZED BY UNIFORM AND LINEAR PRESSURE DISTRIBUTIONS

Figure 63, we observe that even when viscous effects of the fluid are modeled by considering a linearly decaying pressure distribution in the fracture, the borehole pressure predicted is still less than that observed in the experiment.* Therefore, the difference between theory and experiment must be caused by some physical process that has not been modeled by the present solution.

To explain the discrepancy between the solution (R) and Experiment 41, we recall from Appendix A that the stress intensity factor for an internally pressurized fracture in a permeable material is assumed to be the same as that associated with an internally pressurized fracture in an impermeable material with the same mechanical properties as the permeable material. In particular, it has been assumed that the stress intensity factor K_1 is given by

$$K_1 = (P_b - P_o)\ (\pi \ell)^{1/2} \tag{3.1}$$

where P_b is the pressure in the fracture,** P_o is the in situ hydrostatic pressure in the formation, and ℓ is the fracture half-length. During fracture propagation, K_1 is equated with the fracture toughness K_{Ic} of the permeable formation. The formula (3.1) neglects the fact that the stress distribution in the formation material near the fracture is different when the formation has been penetrated by pressurized fracturing fluid than when no fluid penetration is possible. Since the borehole pressure in Experiment 41 is significantly greater than that predicted by the solution (R), we may conclude that the value of the stress intensity factor associated with an internally pressurized

---

*From Figure 42, we observe that for the larger values of fracture half-length, the pressure gradient in the fracture is less steep than that associated with a pressure distribution that decays linearly from P_b at the borehole to zero at the fracture tip.

**In Appendix A, the pressure in the fracture P was specified to be uniform so the borehole pressure $P_b = P$.

fracture in a permeable material that has been penetrated by fracturing fluid is significantly less than the value given by (3.1).

It is expected that the magnitude of the effect of fluid penetration on the value of the stress intensity factor will diminish as the depth of fluid penetration Y into the formation decreases relative to the fracture half-length ℓ. Letting Y_b be the depth of fluid penetration at the borehole, it may be shown from equation (20b) of Appendix A that the ratio Y_b/ℓ is unbounded for $\ell = 0$ and decreases as ℓ increases. Therefore, the effect of fluid penetration on the value of the stress intensity factor may be significant for short fracture half-lengths ℓ even when the formation is relatively impermeable. Some work has been done to analyze elastic porous media;[24,25,26] however, further work is required to quantify this effect and to assess whether this effect must be theoretically modeled to accurately predict the long fracture lengths associated with hydraulic fracture treatments in the field.

Having discussed reasons why the borehole pressure predicted by the solution (R) lies below the experimental results, we note that if the borehole pressure in (R) were increased, the fracture width would be increased, the rate of fluid penetration would be increased, and the curve in Figure 62 for the average fracture half-length would be lowered bringing the results into better agreement with the experiments.

Finally, in Figure 64, we compare the fluid penetration contour measured in Experiment 41 when the average fracture half-length $\ell = 123$ mm with the contour predicted by the present solution for the same value of ℓ. The fact that the present solution underestimates the depth of fluid penetration at the PMMA-hydrostone interface,* relative to the experiment, is consistent with the fact that the solution also underestimates the value of the pressure in the fracture, relative to the experiment.

---

*Recall that the depth of fluid penetration is vertically uniform in the present solution but not in the experiments because boundary effects at the PMMA-interface influenced the fluid penetration in the experiments.

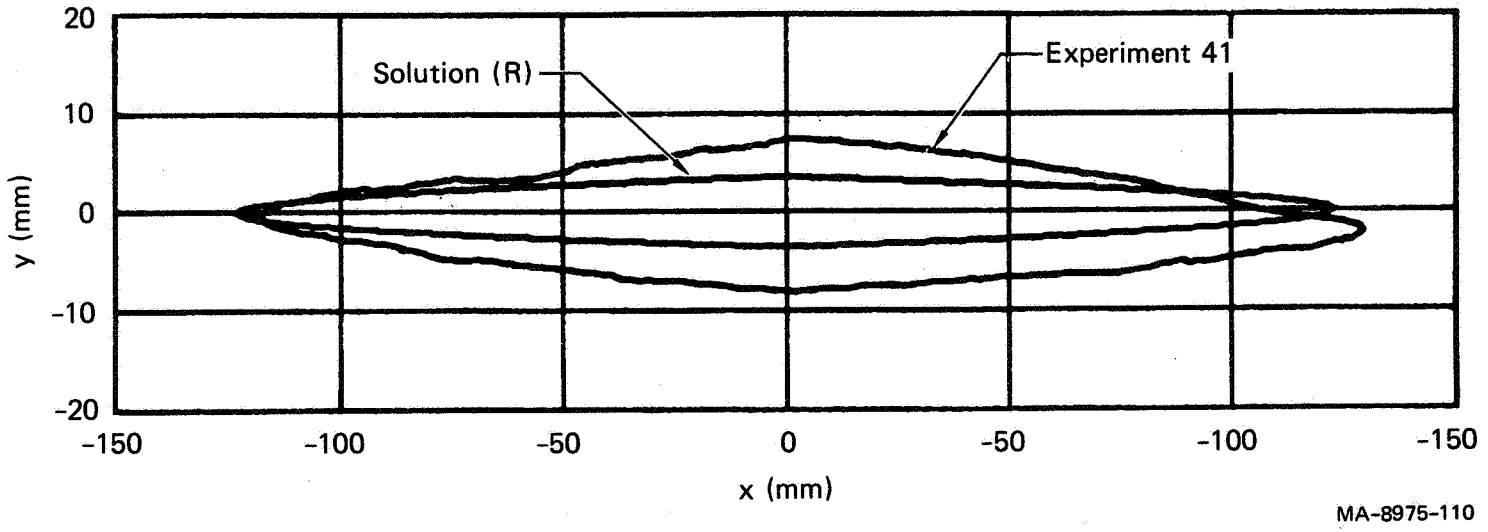

FIGURE 64 PENETRATION CONTOURS FOR THE AVERAGE FRACTURE HALF-LENGTH ℓ = 123 mm MEASURED IN EXPERIMENT 41 AND PREDICTED BY THE PRESENT SOLUTION (R)

REFERENCES

1. Howard, G. C. and Fast, C. R.: Hydraulic Fracturing, Vol. II, Fracturing Monograph Series, Society of Petroleum Engineers, Dallas (1970).

2. Carter, R. D.: "Derivation of the General Equation for Estimating the Extent of the Fractured Area," Appendix to: "Optimum Fluid Characteristics for Fracture Extension," by Howard, G. C., and Fast, C. R., Drill. and Prod. Prac., API (1957) 261-270.

3. Perkins, T. K. and Kern, L. R.: "Width of Hydraulic Fractures," J. Pet. Tech. (September 1969) 937-949.

4. Nordgren, R. P.: "Propagation of a Vertical Hydraulic Fracture," Soc. Pet. Eng. J. (August 1972) 306-314.

5. Khristianovic, S. A. and Zheltov, Y. P.: "Formation of Vertical Fractures by Means of Highly Viscous Liquid," in Proc. Fourth World Pet. Cong., Rome (1955), Sec. II, 579-586.

6. Geertsma, J. and de Klerk, F.: "A Rapid Method of Predicting Width and Extent of Hydraulically Induced Fractures," J. Pet. Tech. (December 1969) 1571-1581.

7. Daneshy, A. A.: "On the Design of Vertical Hydraulic Fractures," J. Pet. Tech. (January 1973) 83-97.

8. Geertsma, J. and Haafkens, R.: "A Comparison of the Theories for Predicting Width and Extent of Vertical Hydraulically Induced Fractures," Journal of Energy Resources Technology, ASME, 101 (1979).

9. Hagoort, J., Weatherill, B. D., and Settari, A.: "Modeling the Propagation of Waterflood-Induced Hydraulic Fractures," Soc. Pet. Eng. J. (August 1980) 293-303.

10. Settari, A.: "Simulation of Hydraulic Fracture Processes," Soc. Pet. Eng. J. (December 1980) 487-500.

11. van Domselaar, H. R. and Visser, W.: "Proppant Concentration in and Final Shape of Fractures Generated by Viscous Gels," Soc. Pet. Eng. J. (December 1974) 531-536.

12. Novotny, E. J.: "Proppant Transport," paper SPE 6813 presented at SPE 52nd Annual Fall Technical Conference, Denver, Colorado, October 9-12, 1977.

13. Daneshy, A. A.: "Numerical Solution of Sand Transport in Hydraulic Fracturing," J. Pet. Tech. (January 1978) 132-140.

14. Clark, P. E. and Quadir, J. A.: "Prop Transport in Hydraulic Fractures: A Critical Review of Particle Settling Velocity Equations," paper SPE/DOE 9866 presented at the 1981 SPE/DOE Low Permeability Symposium, Denver, Colorado, May 22-29, 1981.

15. Haimson, B. and Fairhurst, C.: "Hydraulic Fracturing in Porous-Permeable Materials," J. Pet. Tech. (July 1969) 811-817.

16. Sievert, J. A., Wahl, H. A., Clark, P. E., and Harkin, M. W.: "Prop Transport in a Large Vertical Model," paper SPE/DOE 9865 presented at the 1981 SPE/DOE Low Permeability Symposium, Denver, Colorado, May 27-29, 1981.

17. Stephens, D. R., Heard, H. C., and Schock, R. N.: "High-Pressure Mechanical Properties of Polymethylmethacrylate," Lawrence Livermore Laboratory Technical Report (UCID-16007) (March 30, 1972).

18. Marshall, G. P. and Williams, J. G.: "The Correlation of Fracture Data for PMMA," J. of Materials Science, 8 (1973) 138-140.

19. Cizek, J. C. and Florence, A. L.: "Laboratory Studies of Containment in Underground Nuclear Tests," SRI International Final Report for Project PYU-5958, SRI International, Menlo Park, California (January 1979).

20. Sneddon, I. N. and Lowengrub, M.: Crack Problems in the Classical Theory of Elasticity, John Wiley and Sons, New York (1969).

21. Sih, G. C.: Handbook of Stress-Intensity Factors, Institute of Fracture and Solid Mechanics, Lehigh University, Bethlehem, Pennsylvania (1973).

22. Tada, H., Paris, P. C., and Irwin, G. R.: The Stress Analysis of Cracks Handbook, Del Research Corporation, St. Louis, Missouri (1973).

23. Advani, S. H., Shuck, L. Z., Chang, H. Y., and Gangarao, H. V.: "Analytical and Experimental Investigations on Induced Fracturing of Reservoir Rock," ASME Paper No. 76-Pet-8 (1976).

24. Biot, M. A.: "General Theory of Three-Dimensional Consolidation," J. Appl. Physics, 12 (February 1941) 155-164.

25. Rice, J. R. and Cleary, M. P.: "Some Basic Stress Diffusion Solutions for Fluid-Saturated Elastic Porous Media with Compressible Constituents," Reviews of Geophysics and Space Physics, 14 (May 1976) 227-241.

26. Hagoort, J.: "Hydraulic Fracturing Pressures In Permeable Subsurface Layers," SPE paper 7710 (1978).

Appendix A

ON FLUID LEAK-OFF DURING PROPAGATION OF A VERTICAL HYDRAULIC FRACTURE

This appendix is a copy of a paper that has been submitted for publication. Therefore, the figures, table, and references of the paper should not be confused with those in the main body of this final report.

ON FLUID LEAK-OFF DURING PROPAGATION OF A VERTICAL HYDRAULIC FRACTURE

M. B. Rubin
Research Engineer
Engineering Mechanics Dept.
Poulter Laboratory
SRI International
Menlo Park, CA 94025

ABSTRACT

The classical fluid leak-off model is reexamined, and the problem of determining the extent and width of a propagating vertical hydraulic fracture in an infinite medium is solved, assuming that plane strain conditions exist in horizontal planes. The time dependent fracture width and fluid pressure are determined by assuming that the fracture is uniformly pressurized and that linear elastic fracture mechanics applies. The formation is taken to be permeable in the direction normal to the fracture plane, and the flow velocity of fluid penetrating the formation is determined as part of the solution instead of being specified as it is in the classical fluid leak-off model. A closed-form solution is obtained that shows that the functional form of the flow velocity is significantly different from the form usually specified. Furthermore, this solution is extremely easy to use for designing hydraulic fracture treatments.

Introduction

Hydraulic fracturing techniques are commonly used to stimulate the production of oil and gas from saturated rock formations. Even when the fracture geometry is simplified considerably and the fracture is modeled as a vertical fracture, the problem of determining the fracture extent and width is formidable. Therefore, certain assumptions must be made to obtain a solution. The main objectives of this paper are to reexamine the classical fluid leak-off model and to derive a simple formula for analyzing a propagating vertical fracture.

Here we consider the propagation of a vertical hydraulic fraction in an infinite permeable formation. Letting x, y, z be a fixed set of Cartesian coordinates, the fracture is oriented so that the fracture surface lies in the x-z plane, with x being the coordinate along the length of the fracture, y being the coordinate normal to the fracture surface, and z being the vertical coordinate (see Figure 1). The borehole is modeled as a line source of fluid along the $x = 0$, $y = 0$ line, and the effects of gravity are neglected. For later reference, the major assumptions underlying the analysis of this paper are summarized below:

(A1) The formation is modeled as a homogeneous, isotropic, linearly elastic solid of infinite extent.

(A2) The fracture propagates continuously and symmetrically about the $x = 0$, $y = 0$ line, and it has a half-length $\ell(t)$.

(A3) The fracture height H is constant.

(A4) Plane strain conditions exist in horizontal planes.

(A5) Linear elastic fracture mechanics is valid, and the fracture extends when the value of the stress intensity factor reaches that of the fracture toughness K_{Ic} of the formation material.

(A6) The pressure p(t) applied to the fracture faces is spatially uniform.

(A7) The fracturing fluid is incompressible.*

*The effects of the compressibility of the formation fluid that initially occupies the pore space of the formation is considered later in the text.

(A8) The volumetric injection rate of fluid into the borehole is constant.

(A9) Darcy's law applies, and the formation is permeable only to flow normal to the fracture plane (i.e., in the y direction only).

This paper concentrates on the implementation of assumption (A9). In the present solution, Darcy's law is used to determine the flow velocity of fluid penetrating the formation. More commonly, researchers specify the functional form of the flow velocity instead of determining it directly. It will be shown that the form of the flow velocity of the present solution is significantly different from the form that is specified in the classical fluid leak-off model.[1] Because the predictions of fracture extent and width depend strongly on the amount of fluid lost to the formation, differences in the functional forms of the flow velocity can be significant.

The problem of a propagating vertical hydraulic fracture has been analyzed by many researchers, and the subject has been extensively reviewed in a monograph on hydraulic fracturing by Howard and Fast.[2] The classical solution was obtained by Carter[1] by assuming that the fracture width and fracturing pressure are both constant. To analyze fluid leak-off, Carter[1] specified the flow velocity to be inversely proportional to the square root of the time that a given location of the fracture is exposed to fracturing fluid, the proportionality constant being the fluid-loss coefficient. Others later reformulated the problem by relaxing some of the restrictions associated with the classical solution, but most of them who included fluid leak-off continued to specify the flow velocity in the form taken by Carter.[1] Broadly speaking, these researchers can be separated into two groups: those who assume that plane strain conditions exist in vertical planes and those who assume that plane conditions exist in horizontal planes. Perkins and Kern[3] and Nordgren[4] are included in the first group, and Khristianovic and Zheltov,[5] Geertsma and de Klerk[6] and

Daneshy[7] are included in the second group. Those in the first group neglect the fracture mechanics of the fracture tip, whereas those in the second group include it. Furthermore, all of them relax the assumption (A6) and analyze viscous effects on the pressure distribution along the length of the fracture. These solutions have been compared by Geertsma and Haafkens.[8]

Those authors mentioned above who have included leak-off in their models have used the classical fluid leak-off model[1] and have specified the functional form of the flow velocity.* Recently, however, Hagoort, Weatherill, and Settari[9] have developed a computer program to model the propagation of waterflood-induced hydraulic fractures that does not use the classical leak-off model. Settari[10] has applied a similar computer program to study hydraulic fracture treatments in which the fluid leak-off is not as high as that associated with waterfloods. In these programs, fluid leak-off is determined by using a two-dimensional form of Darcy's law for compressible fluids, and no specification is made for the functional form of the flow velocity. In this respect, their leak-off model is similar to the model presented in this paper.

The next section describes the fluid leak-off model used in this paper and considers two important cases. For Case I, the formation fluid that initially occupies the pore space of the formation is very compressible, whereas for Case II, the formation fluid is only slightly compressible. In the following section, the basic equations are recorded and a simple closed-form solution for Case I is derived that is exact within the context of assumptions (A1) through (A9). Next, an approximate analysis of Case II is given. Examples are then considered to examine the quantitative effects of varying the volumetric injection rate of fluid, the fracturing fluid viscosity, and the compressibility of the formation fluid. Finally, the present solution is compared quantitatively with those of Carter,[1] Nordgren,[4] and Geertsma and de Klerk.[6]

*It is not clear exactly what form the flow velocity takes in Daneshy's[7] computer program.

Fluid Leak-Off Model

To describe the fluid leak-off model used in this paper, let us focus attention on a vertical cross section (x = constant) through the fracture (see the shaded cross section in Figure 1). Figure 2(a) schematically shows the fluid penetration in a typical y-z plane. The actual formation has a permeability K and is saturated with formation fluid. At location x along the fracture and at time t, the pressure in the fracture (fracture-formation interface pressure) is denoted by $p(x,t)$, the depth of penetration of the fracturing fluid into the formation is denoted by* $Y(x,t)$, and the pressure at the interface of the fracturing fluid and the formation fluid (fracturing fluid-formation fluid interface pressure) is denoted by $p_1(x,t)$. Furthermore, it is assumed that initially the in situ stress in the formation is hydrostatic and that far away from the fracture the pressure in the formation fluid is a constant, p_o.

In general, the fracturing fluid can have different mechanical properties than the formation fluid, so the problem of determining the extent of penetration of the fracturing fluid can be complicated. Two important cases naturally arise and will be analyzed separately.

Case I: For this case, the formation fluid is very compressible, so the resistance of the formation to penetration of the fracturing fluid is negligibly affected by the presence of the formation fluid, and the pressure p_1 can be adequately approximated by the constant p_o.

Case II: For this case, the formation fluid is only slightly compressible, so it significantly restricts the penetration of the fracturing fluid, and the pressure p_1 cannot be accurately represented by the constant p_o.

Two special cases have been considered in the literature[2] where the problem of fluid penetration can be solved exactly.

*Here, we are assuming that the fracturing fluid and formation fluid are imiscible.

Special Case 1: For this case, the fracturing fluid is incompressible, the formation fluid is very compressible, and the pressure p in the fracture is constant. It follows from Darcy's law for incompressible fluids that the flow velocity v may be represented in the form

$$v = \frac{C_I}{(t - \tau)^{\frac{1}{2}}} \quad , \quad C_I = \left[\frac{\phi K (p - p_o)}{2\mu}\right]^{\frac{1}{2}} \quad , \qquad (1a,b)$$

where C_I is the fluid-loss coefficient for this case, τ is the time when the fracturing fluid first reaches the given location x in the formation, ϕ is the constant* connected porosity of the formation, and μ is the viscosity of the fracturing fluid.

Special Case 2: For this case, the fracturing fluid and formation fluid are both only slightly compressible, they have the same mechanical properties, and the pressure p in the fracture is constant. Using Darcy's law for slightly compressible fluids, it can be shown that the flow velocity may be represented in the form

$$v = \frac{C_{II}}{(t - \tau)^{\frac{1}{2}}} \quad , \quad C_{II} = (p - p_o)\left[\frac{\phi K c_f}{\pi \mu_f}\right]^{\frac{1}{2}} \quad , \qquad (2a,b)$$

where C_{II} is the fluid-loss coefficient for this case and c_f and μ_f are, respectively, the compressibility and viscosity of the formation fluid.

In the classical solution by Carter,[1] the pressure p was assumed constant, so the specification of the flow velocity v in the form (1) or (2) was consistent with Darcy's law. However, subsequent authors[4,6] specified the flow velocity in the form (1) or (2) even when the pressure p was not constant. It is, therefore, possible that Darcy's law is not satisfied in these cases. In particular, it will be shown that, in the present solution, the pressure p is not constant and Darcy's law demands that the flow velocity have a functional form significantly different from the forms (1) or (2).

*The effect of the compressibility of the formation on the value of the connected porosity ϕ is assumed negligible.

Here we are interested in analyzing both Case I and Case II described above. Within the context of the assumptions of this paper, we will develop an exact closed-form solution for Case I. The solution for the more complicated Case II will be approximated by reformulating the problem to take advantage of the simplifications associated with Case I. We, therefore, choose to model the actual formation, which has permeability K and is saturated with a general formation fluid, with a model formation that has an effective permeability K_{eff} and is saturated with a very compressible formation fluid (see Figure 2b). The fracturing fluid is taken to be incompressible for both Cases I and II, and the effective permeability K_{eff} is specified so that the model formation offers the "same" resistance to penetration of fracturing fluid as the actual formation. For Case I, the actual formation fluid is very compressible, so the effective permeability K_{eff} is equal to the actual permeability K without approximation. Hence

$$K_{eff} = K \qquad \text{for Case I} \quad . \tag{3}$$

For Case II, the actual formation fluid is only slightly compressible and the specification of K_{eff} is more complicated. The details of this specification are described in a later section.

Basic Equations and Solution

Assuming that the effective pressure $p - p_o$ is the pressure that causes fracture initiation,* we may recall, from Sneddon and Lowengrub,[11] the expressions for the stress intensity factor† K_1 and the fracture width w and write

*This assumption neglects the effect on the formation of the pressure distribution in the fracturing fluid that has penetrated the formation. It is expected that this effect is small when the depth of penetration Y is small.

†The definition of the stress intensity factor K_1 found in Sneddon and Lowengrub[11] is commonly reserved for the quantity k_1, which equals $K_1/(\pi)^{\frac{1}{2}}$ [see Sih, Ref. 12].

$$p - p_o = \frac{K_{Ic}}{[\pi\, \ell(t)]^{\frac{1}{2}}} \tag{4a}$$

$$w = \frac{4(1 - \nu^2)K_{Ic}}{E[\pi\, \ell(t)]^{\frac{1}{2}}} [\ell^2(t) - x^2]^{\frac{1}{2}} \quad \text{for} \quad |x| \leq \ell(t) \quad , \tag{4b}$$

where E is Young's modulus, ν is Poisson's ratio, and assumption (A5) has been used to equate K_1 with the fracture toughness K_{Ic} during fracture propagation.

Furthermore, we may use the symmetry properties of our problem and confine attention to the quarter space $x \geq 0$, $y \geq 0$. It follows from (4b) and the assumtion (A3) that the fracture volume V_f is determined by the expressions

$$V_f = 2H \int_o^{\ell} w(x,t)dx \quad , \tag{5a}$$

$$V_f(t) = \left[\frac{2H(1 - \nu^2)K_{Ic}\, \pi^{\frac{1}{2}}}{E}\right] [\ell(t)]^{3/2} \quad . \tag{5b}$$

Thus, using linear elastic fracture mechanics, we have deduced expressions relating the effective pressure $p - p_o$, the fracture volume V_f, and the half-length $\ell(t)$ of a continuously propagating fracture.

Next, we use Darcy's law for one-dimensional flow (see Ref. 13, p. 59) and express the mean flow velocity v of fluid penetrating the formation in the form

$$v = \begin{cases} -\left(\dfrac{K_{eff}}{\mu}\right) \dfrac{\partial P}{\partial y}\bigg|_{y=0} & \text{for} \quad |x| < \ell \\ 0 & \text{for} \quad |x| \geq \ell \end{cases} \tag{6}$$

where P is the pressure in the fracturing fluid that has penetrated the formation and K_{eff} is the effective permeability of the model formation. Since the fracturing fluid is taken to be incompressible, the flow velocity v may also be expressed in terms of the connected porosity ϕ and the depth of penetration Y(x,t) through the equation

$$v = \phi \frac{\partial Y}{\partial t} \quad . \tag{7}$$

In addition, the reduced form of the continuity equation for flow of an incompressible fluid through a permeable material becomes [see Ref. 13, p.70]

$$\frac{\partial^2 P}{\partial y^2} = 0 \quad . \tag{8}$$

At the interface of the fracture with the formation, the pressure P equals the pressure p in the fracture, and at the interface of the fracturing fluid and the formation fluid, the pressure P equals* p_o. Therefore, integrating (8) subject to the boundary conditions

$$P = p \quad \text{at} \quad y = 0 \quad , \tag{9a}$$

$$P = p_o \quad \text{at} \quad y = Y(x,t) \tag{9b}$$

we may write

$$\frac{\partial P}{\partial y} = - \frac{p - p_o}{Y} \tag{10}$$

Now with the help of (4a), (7), and (10), the equation (6) may be re-written in the form

$$\frac{\partial}{\partial t}\left[\frac{1}{2}\phi Y^2\right] = \left[\frac{K_{eff}\, K_{Ic}}{\mu\, \pi^{\frac{1}{2}}}\right] [\ell(t)]^{-\frac{1}{2}} \quad \text{for} \quad |x| < \ell \quad . \tag{11}$$

*Recall that the formation fluid in the model formation is very compressible, so the pressure p_1 can be approximated by the constant p_o.

For the region ahead of and including the fracture tip, we impose the condition that the fluid does not penetrate the formation. Hence, we require

$$Y = 0 \quad \text{for} \quad |x| \geq \ell(t) \quad . \tag{12}$$

It follows from (7) and (12) that equation (6) is satisfied for $|x| \geq \ell$.

Since the fracture is assumed to propagate continuously, we can parameterize the fracturing process by using either time t or the fracture half-length $\ell(t)$. Consequently, by introducing the function τ to be the inverse of the function ℓ such that

$$\ell(t) = \lambda \quad \text{when} \quad t = \tau(\lambda) \quad , \tag{13}$$

equation (11) may be integrated to yield

$$Y(x,t) = \left[\frac{2K_{eff} K_{Ic}}{\mu\phi\pi^{\frac{1}{2}}} \int_{|x|}^{\ell(t)} \lambda^{-\frac{1}{2}} \frac{d\tau}{d\lambda} \, d\lambda \right]^{\frac{1}{2}} \quad \text{for} \quad |x| \leq \ell(t) \quad , \tag{14}$$

where in obtaining (14), we used the condition (12) for $|x| = \ell$. Recalling that the expression Y given by (14) represents the extent of fluid penetration into each face of the formation, the total volume $V_L(t)$ of fracturing fluid lost to the formation is given by

$$V_L(t) = 4H\phi \int_0^{\ell(t)} Y(x,t) \, dx \quad . \tag{15}$$

Because the volumetric flow rate q of fluid into the fracture is assumed to be constant, the total volume $V_T(t)$ of fluid pumped into the borehole may be expressed as

$$V_T(t) = qt \quad . \tag{16}$$

It follows from the incompressibility of the fracturing fluid that the equation

$$V_T(t) = V_L(t) + V_f(t) \tag{17}$$

represents the global form of the conservation of mass of the fracturing fluid.

In view of the expressions (5b), (15), and (16), equation (17) represents an integral equation for determining the function $\ell(t)$. When the formation is impermeable and there is no fluid leak-off, the function $\ell(t)$ may be written in the simple form

$$\ell(t) = (at)^{2/3} = (\bar{a}\, V_T)^{2/3} \quad , \quad a = \bar{a}q \tag{18a,b}$$

where a and $\bar{a}$ are constants determined by equation (17). When the formation is permeable and fluid leak-off is included, it can be shown that the integral equation (17) also admits the solution (18a). To determine the value of the constant $\bar{a}$ for this case, we first use (18a) and write the inverse function $\tau(\lambda)$ defined in (13) in the form

$$\tau(\lambda) = \left(\frac{1}{\bar{a}q}\right)\lambda^{3/2} \quad . \tag{19}$$

Then with the help of (5b), (14), (15), (18), and (19), the results*

$$V_f = \left[\frac{2H(1-\nu^2)\bar{a}\, K_{Ic}\, \pi^{\frac{1}{2}}}{E}\right](qt) \quad , \tag{20a}$$

$$Y = \left[\frac{3K_{eff}\, K_{Ic}}{q\mu\, \phi\, \bar{a}\, \pi^{\frac{1}{2}}}\right]^{\frac{1}{2}} [\ell - |x|]^{\frac{1}{2}} \quad \text{for} \quad |x| \le \ell \quad , \tag{20b}$$

$$V_L = 8H\left[\frac{\phi\, \bar{a}\, K_{eff}\, K_{Ic}}{3q\, \mu\, \pi^{\frac{1}{2}}}\right]^{\frac{1}{2}}(qt) \quad , \tag{20c}$$

*The quantity $V_T = qt$ has been factored out of the expressions for V_f and V_L for later convenience.

may be deduced. Substitution of (16), (20a), and (20c) into (17) yields the quadratic equation

$$a_2 \bar{a} + a_1 \bar{a}^{-\frac{1}{2}} - 1 = 0 \tag{21}$$

where

$$a_1 = 8H \left[\frac{\phi K_{eff} K_{Ic}}{3q \mu \pi^{\frac{1}{2}}} \right]^{\frac{1}{2}} , \tag{22a}$$

$$a_2 = \left[\frac{2H(1 - \nu^2) K_{Ic} \pi^{\frac{1}{2}}}{E} \right] . \tag{22b}$$

Since $\bar{a}^{-\frac{1}{2}}$ must be positive, the solution of (21) may be written as

$$\bar{a} = \left[\frac{- a_1 + (a_1^2 + 4 a_2)^{\frac{1}{2}}}{2 a_2} \right]^2 . \tag{23}$$

Once the quantities

$$\{E, \nu, K_{Ic}, K_{eff}, \phi, H, q, \mu\} \tag{24}$$

are specified, the constant $\bar{a}$ may be determined from the simple expression (23) and the quantities $\ell(t)$, V_f, Y, and V_L can be determined using expressions (18) and (20). It is interesting to note that this solution predicts that the ratio of the volume of fluid lost to the formation $V_L(t)$ to the total volume of fluid pumped into the borehole $V_T(t)$ is independent of time and is given by

$$\frac{V_L}{V_T} = 8H \left[\frac{\phi \bar{a} K_{eff} K_{Ic}}{3q \mu \pi^{\frac{1}{2}}} \right]^{\frac{1}{2}} = a_1 \bar{a}^{-\frac{1}{2}} . \tag{25}$$

The fluid leak-off ratio V_L/V_T of the classical solution[1] is a function of time. Additional discussion of this point is given later in the text.

Recall now from our previous discussion that most authors specify the flow velocity v in the forms (1a) or (2a). We emphasize that, in the present analysis, the flow velocity is not specified but is determined as part of the solution. In particular, we may use (7), (18), (19), and (20b) to conclude that

$$v = (\bar{a}\, q)^{1/3} \left(\frac{\phi\, K_{eff}\, K_{Ic}}{3q\, \mu\, \bar{a}\, \pi^{\frac{1}{2}}} \right)^{\frac{1}{2}} (t^{2/3} - \tau^{2/3})^{-\frac{1}{2}}\, t^{-1/3} \quad . \tag{26}$$

It is obvious that expression (26) is quite different from expressions (1a) or (2a) associated with the classical fluid leak-off model. This is not surprising since, in the present solution, the effective pressure $p - p_o$ is a function of time, whereas in the special cases 1 and 2 described previously the effective pressure was taken to be constant.

An Approximate Analysis When the Formation Fluid is Only Slightly Compressible

In a previous section, we discussed Case I where the formation fluid was very compressible and Case II where the formation fluid was only slightly compressible by considering a model formation with an effective permeability K_{eff} that was saturated with a very compressible fluid. For Case I, K_{eff} is equal to the actual permeability K of the formation (see Eq. 3) and a simple closed-form solution can be obtained. For Case II, the actual problem is considerably more complicated and is treated here only in an approximate manner.

Basically, we specify the permeability K_{eff} of the model formation by requiring the model formation to have the "same" resistance to fluid penetration as the actual formation that is saturated with a slightly compressible fluid. To elaborate, we consider two problems. For the first problem, we derive an expression for the flow velocity of the incompressible fracturing fluid penetrating the model formation under the action of a constant effective pressure $p - p_o$. For the second problem, we derive an expression for the flow velocity of a slightly compressible fluid penetrating the actual formation (which is saturated with the same

slightly compressible fluid) under the action of the same constant effective pressure. Then the value of K_{eff} is specified by equating the expressions for the flow velocities associated with these two problems. The expression for the flow velocity of the first problem is given by (1) with K replaced by K_{eff}, and the expression for the second problem is given by (2). It follows that the effective permeability K_{eff} is specified by the equation

$$K_{eff} = \left(\frac{2\mu \ c_f \ \Delta p_{avg}}{\pi \ \mu_f} \right) K \qquad \text{for Case II} \quad , \tag{27}$$

where we have replaced $p - p_o$ with the length average* effective pressure Δp_{avg} associated with the hydraulic fracture treatment under consideration. In particular, if we consider a fracture treatment with a final fracture half-length L, we may use (4a) to calculate Δp_{avg} from the formula

$$\Delta p_{avg} = \frac{1}{L} \int_o^L \frac{K_{Ic}}{(\pi \ \lambda)^{\frac{1}{2}}} \ d\lambda = \frac{2K_{Ic}}{(\pi \ L)^{\frac{1}{2}}} \quad . \tag{28}$$

The solution for Case II is determined by first specifying values for the quantities (24) as well as the final fracture half-length L and the formation fluid properties c_f, μ_f. Then the effective permeability K_{eff} can be calculated using formulas (27) and (28), and the solution is obtained just as in Case I.

Examples

To examine some of the basic features of the present solution, we consider examples of hydraulic fracturing treatments that differ by variations in the injection rate q, the fracturing fluid viscosity μ, the permeability K of the formation, and the formation fluid compressibility c_f. For this purpose, let us consider a formation of shale with typical material properties specified by

*Alternatively, the time average effective pressure could be used but this is not done for later convenience.

$$E = 3.45 \times 10^{10} \text{ Pa}$$

$$\nu = 0.2$$

$$K_{Ic} = 1.21 \times 10^{6} \text{ Pa-m}^{\frac{1}{2}} \qquad (29)$$

$$K = 100 \text{ μd} = 9.87 \times 10^{-17} \text{ m}^2$$

$$\phi = 0.05$$

where the symbols Pa, m, and μd stand for Pascal, meter, and microdarcy, respectively. The fracture height H and final fracture half-length L are taken to be

$$H = 50 \text{ m} \qquad (30)$$

$$L = 150 \text{ m} \quad .$$

As a standard for comparison, let us consider a hydraulic fracturing treatment for which*

$$q = 2 \text{ bbl/min} = 5.30 \times 10^{-3} \text{ m}^3 \text{ s}^{-1} \qquad (31)$$

$$\mu = 1 \text{ cp} = 1 \times 10^{-3} \text{ Pa-s} \quad .$$

Inspection of formulas (16), (18a), (20), (22), (23), and (25) reveals that, when V_T is taken to be the independent variable instead of time t, the quantities $\bar{a}$, ℓ, V_f, Y, V_L, and V_L/V_T depend on the variables q and μ only through the product qμ. It follows that increasing the flow rate q and holding the viscosity μ constant has the same effect as increasing μ by the same factor and holding q constant.

Examples have been considered that examine the effect of varying the parameters q, μ, K, and c_f. Table 1 lists various specifications of these

*The formulas of this paper require all quantities to be expressed in a consistent set of units. Therefore, for calculational purposes, we have chosen to express all quantities in SI units. However, for the convenience of the reader, we record (in the text and in Table 1) the values of volume, volumetric flow rate, viscosity, and permeability in terms of their more common units bbl, bbl/min, cp and μd, respectively.

Table 1

PARAMETERS CHARACTERIZING THE SOLUTIONS PRESENTED IN FIGURES 3 AND 4

	q(bbl/min)	μ(cp)	K(μd)	c_f(Pa^{-1})	K_{eff} (μd)	$\bar{a}$($m^{-3/2}$)	V_L/V_T	$\bar{L}$ (m)
Curve	Case I							
3A,4A	2	1	100	-	100	22.20	0.8675	150
3B	10	1	100	-	100	60.36	0.6398	292
3C	20	1	100	-	100	80.19	0.5214	353
3B	2	5	100	-	100	60.36	0.6398	292
3C	2	10	100	-	100	80.19	0.5214	353
4D	2	1	0	-	0	167.6	0	577
	Case II							
4B	2	1	100	4.4×10^{-7}	3.1	110.3	0.3417	437
4C	2	1	100	4.4×10^{-9}	3.1×10^{-2}	160.7	0.04124	561

parameters* as well as the values of $\bar{a}$, V_L/V_T, and the final fracture half-length $\bar{L}$ associated with pumping a total volume V_T of 520.5 bbl. This value of V_T corresponds to the volume of fluid required to create the fracture associated with our standard for comparison, curve 3A.

For Case I (very compressible formation fluid), the value of K_{eff} is given by expression (3). Solutions of ℓ versus V_T are presented in Figure 3 to show the effect of varying the flow rate q or the fracturing fluid viscosity μ. Increasing either q or μ has the effect of decreasing the ratio V_L/V_T (see Table 1) that characterizes the relative amount of fluid lost to the formation and in turn has the effect of increasing the fracture length associated with a specified value V_T of total volume pumped into the formation.

For Case II (slightly compressible formation fluid), K_{eff} is given by the expression (27). Solutions† of ℓ verses V_T are presented in Figure 4 to show the effect of varying the formation fluid compressibility c_f. Two values of c_f were considered: one value corresponds to a formation fluid that is 100 times more compressible than water (curve 4B), and the other value equals the compressibility of water (curve 4C). For comparison purposes, we have also included in Figure 4 the solution of ℓ verses V_T associated with an impermeable formation (curve 4D). The solutions presented in Figure 4 and Table 1 show that for a given value of V_T, the fracture half-length ℓ increases as the compressibility of the formation fluid decreases. Furthermore, Figure 4 shows that the formation that is saturated with water behaves nearly like an impermeable formation for the hydraulic fracture treatment considered.

---

*The various combinations of parameters in Table 1 are labeled as, say, curve 3A to denote that the solution associated with these parameters is plotted in Figure 3 as curve 3A.

†For these calculations, the formation fluid viscosity μ_f was set equal to the fracturing fluid viscosity μ.

Quantitative Comparison With Other Solutions

The relevant formulas required to make predictions using the solutions of Carter,[1] Nordgren[4] and Geertsma and de Klerk[6] are summarized in the appendix. From the formulas (A-1), we observe that values must be specified for the average fracture width w_{avg}, the average effective pressure Δp_{avg} and the fluid-loss coefficient C before Carter's solution can be evaluated. This means that an appeal must be made to some solution that can predict values for these quantities. Here, we choose to use the present solution. The value of Δp_{avg} is specified by using equation (28) which determines the average effective pressure associated with propagating a fracture of half-length L. To determine a value for the average fracture width, w_{avg}, associated with the same fracture, we substitute the expression (4b) into the integral

$$w_{avg} = \frac{1}{L} \int_0^L \frac{1}{\ell} \int_0^{\ell} w \, dx \, d\ell \tag{32}$$

and obtain the expression

$$w_{avg} = \left[\frac{2(1 - \nu^2) \, K_{Ic} \, \pi^{\frac{1}{2}}}{3E} \right] L^{\frac{1}{2}} \quad . \tag{33}$$

Recall that, in the present solution, the effective pressure $p - p_o$ is a function of time, so the fluid-loss coefficient that is determined by the usual expressions (1b) or (2b) would not be constant. Since the fluid-loss coefficient C is generally taken to be constant, we identify C with C_I given by expression (1b) in which $p - p_o$ is replaced by the average effective pressure Δp_{avg} associated with propagating a fracture of half-length L. Hence, we specify the fluid-loss coefficient C by the formula

$$C = \left[\frac{\phi \, K \, \Delta p_{avg}}{2\mu} \right]^{\frac{1}{2}} \quad . \tag{34}$$

In evaluating Carter's solution, the quantities Δp_{avg} and w_{avg} are determined by (28) and (33), respectively, and the fluid-loss coefficient is determined by (34).

In contrast with Carter's solution, it is possible to evaluate the solutions of Nordgren[4] and Geertsma and de Klerk[6] without appealing to predictions from another solution. This may be done by calculating the average effective pressure Δp_{avg}, for a fracture of half-length L, directly from the formulas (A-2c) and (A-3c). Hence, for Nordgren's solution we obtain*

$$\Delta p_{avg} = \frac{16}{5}\left[\frac{E^3 \mu (q/2)}{4 \pi^2 (1-\nu^2)^3 H^4}\right]^{1/4} L^{1/4} \tag{35}$$

and for the solution of Geertsma and de Klerk, we obtain

$$\Delta p_{avg} = 2\left[\frac{21 \mu q}{32 \pi H}\left(\frac{E}{1-\nu^2}\right)^3\right]^{1/4} L^{-1/2} \quad . \tag{36}$$

The fluid-loss coefficient C used in each of these solutions is evaluated by substituting the expressions (35) and (36), respectively, into the formula (34). The resulting values of C will not be the same since the expressions (35) and (36) are not identical.

The present solution and those of Carter,[1] Nordgren,[4] and Geertsma and de Klerk[6] were evaluated for the hydraulic fracture treatment associated with the specifications (29), (30), and (31) (curve 3A in Table 1).

---

*Recall that Δp_{avg} has been defined as the length average so that $\Delta p_{avg} = \frac{1}{L}\int_0^L (p_b - p_o) d\ell$. Alternatively, the time average effective pressure could be used but this would be very inconvenient to evaulate for the solution of Geertsma and de Klerk unless the function for fracture half-length ℓ (A-3a) is approximated by taking the limit as ζ becomes large. Further, we note that the expression (35) was obtained using the formulas (A-2) even though Nordgren's solution is not valid for short times and hence short fracture lengths.

Figures 5 through 8 show graphically the major differences between the present solution and the other solutions. Figure 5 compares predictions of the fracture half-length ℓ, and Figure 6 compares predictions of the fracture width at the borehole* w_b. Figure 7 compares predictions of the effective borehole pressure† $p_b - p_o$. Figure 8 compares the leak-off ratio V_L/V_T associated with the present solution and that of Carter.[1] Since Nordgren's solution is not valid for short times, we have not plotted it in Figures 5, 6, and 7 for small values of V_T.

Using the formulas recorded in the Appendix, it can be shown that for large values of V_T (or large times), the functional form for the fracture half-length ℓ predicted by the solutions of Carter (C) and Geertsma and de Klerk (GK) approach the form predicted by the solution of Nordgren (N). If we denote this limiting functional form of ℓ by ℓ_∞, then expression (A-2a) can be rewritten as

$$\ell_\infty = \left[\frac{q^{\frac{1}{2}}}{2\pi\ C\ H} \right] V_T^{\frac{1}{2}} \tag{37}$$

where equation (16) has been used.

Figure 5 shows that for large values of V_T, the values of ℓ predicted by the solutions (C), (GK), and (N) are different. This is partly because the value of the fluid-loss coefficient C associated with each of the solutions is different and partly because the solution (GK) has not attained the limiting value (37). More important, Figure 5 shows that for large values of V_T, the present solution (R) predicts a larger value of ℓ than either of the solutions (C), (N), or (GK). In particular, we may use (18a) and (37) to conclude that the ratio of the fracture half-length ℓ predicted by the present solution to the limiting value ℓ_∞ given by the expression (37) may be expressed in the form

---

*For the present solution, w_b is given by the expression (4b) evaluated at $x = 0$.

†In the present solution, the pressure p is uniform in the fracture so the borehole pressure $p_b = p$.

$$\frac{\ell}{\ell_\infty} = \left[\frac{2\pi\ C\ H\ \bar{a}^{2/3}}{q^{\frac{1}{2}}}\right] V_T^{1/6} \quad . \tag{38}$$

It follows from (38) that the differences between the predictions of the present solution and the other solutions can be significant and, in particular, the differences in the values for ℓ increase with increasing values of V_T.

Figure 6 shows that for large values of V_T, the fracture width at the borehole predicted by the solutions (R), (N), and (GK) is larger than that predicted by the solution (C). This is because the fracture geometry is not rectangular as is assumed in the solution (C).

Figure 7 shows the effect of including the fracture mechanics of the fracture tip in the analysis of the problem. Curves (R) and (GK) include this effect and show that the borehole pressure decreases with increasing V_T (or increasing fracture length). Curves (C) and (N) exclude this effect. Consequently, the borehole pressure p_b predicted by the solution* (N) is significantly different from that predicted by the solutions (R) and (GK). In particular, the solution (N) predicts that the pressure increases (rather than decreases) with increasing V_T. Since the borehole pressure can be measured during a hydraulic fracture treatment, it may be possible to conduct experiments to determine conditions when the solutions (R) and (GK) are more accurate than the solution (N) and vice versa.

Recall from our previous discussion that the fluid leak-off model used in developing the present solution is considerably different from the classical model used by Carter.[1] Since the equation representing the continuity of fracturing fluid is used to determine the fracture

*In the solution (C), the borehole pressure is assumed to be constant.

length, differences in fluid leak-off models can significantly affect the prediction of fracture length. Figure 8 compares the prediction of the classical solution (C) with that of the present solution (R) for the ratio of the volume lost to the formation V_L to the total volume V_T pumped into the formation. The classical solution predicts that the fluid-loss ratio V_L/V_T increases from zero to unity as V_T increases, whereas the present solution predicts that this ratio remains constant. It follows that, for large values of V_T, the present solution predicts a larger value of the fracture volume V_f than is predicted by the classical theory. This fact may partially explain the result of Figure 5 that, for large values of V_T, the present theory predicts a larger fracture length than predicted by the other solutions.

Summary

We have reexamined the classical fluid leak-off model,[1] which specifies a functional form for the flow velocity of fluid leaking off into the formation, and have obtained a simple closed-form solution of the problem of a propagating vertical hydraulic fracture. Using Darcy's law for flow in a permeable formation, we determined the functional form for the flow velocity as part of the solution of the problem instead of specifying it. The functional form of the flow velocity of the present solution is very different from the form specified in the classical fluid leak-off model. This difference significantly affects the predictions of the volume of fluid lost to the formation, the fracture volume, and the length of the fracture.

NOMENCLATURE

a	constant (defined in Eq. 18a)
a_1	constant (defined in Eq. 22a)
a_2	constant (defined in Eq. 22b)
$\bar{a}$	constant (determined by Eq. 23)

c_f	compressibility of the formation fluid
C	fluid-loss coefficient
C_I	fluid-loss coefficient (defined in Eq. 1)
C_{II}	fluid-loss coefficient (defined in Eq. 2)
E	Young's modulus
H	vertical height of fracture
k_1	stress intensity factor (equal to $K_1/\pi^{\frac{1}{2}}$)
K	permeability of the actual formation
K_{eff}	permeability of the model formation
K_1	stress intensity factor
K_{Ic}	fracture toughness of the formation
ℓ	fracture half-length
ℓ_∞	fracture half-length predicted by Nordgren
L	final value of the fracture half-length
$\bar{L}$	final fracture half-length associated with pumping a total volume V_T of 520.5 bbl
p	pressure in fracture
$p - p_o$	effective pressure causing fracture propagation
$\bar{p}$	pressure defined by Geertsma and de Klerk
p_o	in situ hydrostatic pressure
p_1	fracturing fluid-formation fluid interface pressure
p_b	borehole pressure
p_w	pressure defined by Geertsma and de Klerk
P	pressure in fracturing fluid that has penetrated the formation
q	volumetric injection rate
t	time

v	mean flow velocity of fluid into formation
V_f	volume of fracture
V_L	volume of fluid lost to formation
V_T	total volume of fluid pumped into formation
w	fracture width
w_{avg}	average fracture width (defined in Eq. 33)
w_b	fracture width at borehole
w_{we}	final fracture width at borehole (defined in Eq. A-5)
x, y, z	Cartesian coordinates (see Figure 1)
Y	depth of penetration of fracturing fluid into formation
λ	dummy variable
Δp_{avg}	average pressure in fracture (defined in Eq. 28)
ζ	variable (defined in Eq. A-4b)
μ	viscosity of fracturing fluid
μ_f	viscosity of formation fluid
ν	Poisson's ratio
ξ	variable (defined in Eq. A-4a)
τ	arrival time of fracture tip to location x
ϕ	connected porosity of formation

ACKNOWLEDGMENT

The results reported here were obtained in the course of research supported by the U.S. Department of Energy under Contract AC-21-79MC11597, with SRI International.

REFERENCES

1. Carter, R. D.: "Derivation of the General Equation for Estimating the Extent of the Fractured Area," Appendix to: "Optimum Fluid Characteristics for Fracture Extension," by Howard, G. C., and Fast, C. R., Drill. and Prod. Prac., API (1957) 261-270.

2. Howard, G. C. and Fast, C. R.: Hydraulic Fracturing, Vol. II, Fracturing Monograph Series, Society of Petroleum Engineers, Dallas (1970).

3. Perkins, T. K. and Kern, L. R.: "Width of Hydraulic Fractures," J. Pet. Tech. (September 1961) 937-949.

4. Nordgren, R. P.: "Propagation of a Vertical Hydraulic Fracture," Soc. Pet. Eng. J. (August 1972) 306-314.

5. Khristianovic, S. A. and Zheltov, Y. P.: "Formation of Vertical Fractures by Means of Highly Viscous Liquid," Proc. Fourth World Pet. Cong., Rome (1955) Sec. II, 579-586.

6. Geertsma, J. and de Klerk, F.: "A Rapid Method of Predicting Width and Extent of Hydraulically Induced Fractures," J. Pet. Tech. (December 1969) 1571-1581.

7. Daneshy, A. A.: "On the Design of Vertical Hydraulic Fractures," J. Pet. Tech. (January 1973) 83-97.

8. Geertsma, J. and Haafkens, R.: "A Comparison of the Theories for Predicting Width and Extent of Vertical Hydraulically Induced Fractures," Journal of Energy Resources Technology, ASME, Vol. 101 (1979).

9. Hagoort, J., Weatherill, B. D., and Settari, A.: "Modeling the Propagation of Waterflood-Induced Hydraulic Fractures," Soc. Pet. Eng. J. (August 1980) 293-303.

10. Settari, A.: "Simulation of Hydraulic Fracture Processes," Soc. Pet. Eng. J. (December 1980) 487-500.

11. Sneddon, I. N. and Lowengrub, M.: Crack Problems in the Classical Theory of Elasticity, John Wiley and Sons, New York (1969).

12. Sih, G. C.: Handbook of Stress-Intensity Factors, Institute of Fracture and Solid Mechanics, Lehigh University, Bethlehem, Pennsylvania (1973).

13. Collins, R. E.: Flow of Fluids Through Porous Materials, The Petroleum Publishing Company, Tulsa (1976).

APPENDIX

This appendix records the expressions for the fracture half-length ℓ, the fracture width w_b at the borehole, and the borehole pressure p_b associated with the solutions of Carter,[1] Nordgren,[4] and Geertsma and de Klerk.[6] Confining attention to a two-sided vertical hydraulic fracture, we have:

Carter

$$\ell = \left(\frac{q\, w_{avg}}{8C^2\, H\pi}\right)\left[e^{\xi^2}\ \text{erfc}\ (\xi) + \frac{2}{\pi^{\frac{1}{2}}}\,\xi - 1\right] \quad , \tag{A-1a}$$

$$w_b = w_{avg} \quad , \tag{A-1b}$$

$$p_b - p_o = \Delta p_{avg} \quad , \tag{A-1c}$$

Nordgren (large fluid-loss rate)

$$\ell = \ell_\infty = \left[\frac{q/2}{\pi\ C\ H}\right] t^{\frac{1}{2}} \quad , \tag{A-2a}$$

$$w_b = 4\left[\frac{4(1-\nu^2)\mu(q/2)^2}{\pi^3\ E\ C\ H}\right]^{\frac{1}{4}} t^{1/8} \quad , \tag{A-2b}$$

$$p_b - p_o = 4\left[\frac{E^3\,\mu(q/2)^2}{4\,\pi^3(1-\nu^2)^3\ C\ H^5}\right]^{\frac{1}{4}} t^{1/8} \quad , \tag{A-2c}$$

Geertsma and de Klerk*

$$\ell = \left[\frac{q\, w_{we}}{32H\ C^2}\right]\left[e^{\zeta^2}\ \text{erfc}(\zeta) + \frac{2}{\pi^{\frac{1}{2}}}\,\zeta - 1\right] \quad , \tag{A-3a}$$

*In obtaining these formulas, we have neglected the effect of spurt losses and have set $\bar{p} = p_w$ in the equations of Geertsma and de Klerk.[6]

$$w_b = \left[\frac{168\ \mu\ q\ (1 - \nu^2)}{\pi\ H\ E}\right]^{\frac{1}{4}}\ \ell^{\frac{1}{2}} \qquad \text{(A-3b)}$$

$$p_b - p_o = \left[\frac{21\ \mu\ q}{32\ \pi\ H}\left(\frac{E}{1 - \nu^2}\right)^3\right]^{\frac{1}{4}}\ \ell^{-\frac{1}{2}} \qquad \text{(A-3c)}$$

where the parameters ξ and ζ are defined by the equations

$$\xi = \left(\frac{2C}{w_{avg}}\right)(\pi t)^{\frac{1}{2}} \quad , \qquad \text{(A-4a)}$$

$$\zeta = \left(\frac{8C}{\pi\ w_{we}}\right)(\pi t)^{\frac{1}{2}} \quad , \qquad \text{(A-4b)}$$

and where w_{we} is the fracture width at the borehole at the time the pump stops. Since we are considering a hydraulic fracture treatment with a final fracture half-length L, we may evaluate (A-3b) at $\ell = L$ to obtain the expression

$$w_{we} = \left[\frac{168\ \mu\ q\ (1 - \nu^2)}{\pi\ H\ E}\right]^{\frac{1}{4}}\ L^{\frac{1}{2}} \quad . \qquad \text{(A-5)}$$

Finally, we recall that Carter[1] assumed that the fracture width was constant. It follows from expressions (A-1) and (A-4a) that for Carter's solution, the fluid-loss ratio V_L/V_T may be represented by the expression

$$\frac{V_L}{V_T} = \left[1 - \frac{2H\ w_{avg}\ \ell}{qt}\right] = 1 - \frac{1}{\xi^2}\left[e^{\xi^2}\ \text{erfc}(\xi) + \frac{2}{\pi^{\frac{1}{2}}}\ \xi - 1\right] \quad . \qquad \text{(A-6)}$$

SI Metric Conversion Factors

bbl x 1.589 873	E - 01	=	m^3
cp x 1.0*	E - 03	=	Pa-s
ft x 3.048*	E - 01	=	m
psi x 6.894 757	E + 00	=	kPa
psi^{-1} x 1.450 377	E - 01	=	kPa^{-1}

*Conversion factor is exact.

LIST OF FIGURE CAPTIONS

Figure 1: Geometry of Vertical Fracture (Plane strain in horizontal planes)

Figure 2: Cross Sections (x = constant) Through the Fracture in (a) The Actual Formation and (b) The Model Formation

Figure 3: Predictions for the Fracture Half-Length ℓ Showing the Effect of Varying the Fracturing Fluid Viscosity μ or the Pumping Rate q (Curves 3A, 3B and 3C are solutions for the parameters specified in Table 1)

Figure 4: Predictions for the Fracture Half-Length ℓ Showing the Effect of Varying the Formation Fluid Compressibility c_f (Curves 4A, 4B, 4C and 4D are solutions for the parameters specified in Table 1.)

Figure 5: Predictions for the Fracture Half-Length ℓ Associated with the Present Solution (R) and the Solutions of Carter (C), Nordgren (N), and Geertsma and de Klerk (GK)

Figure 6: Predictions for the Fracture Width w_b at the Borehole Associated with the Present Solution (R) and the Solutions of Carter (C), Nordgren (N) and Geertsma and de Klerk (GK)

Figure 7: Predictions for the Effective Pressure at the Borehole $p_b - p_o$ Associated with the Present Solution (R) and the Solutions of Carter (C), Nordgren (N) and Geertsma and de Klerk (GK)

Figure 8: Predictions for the Fluid-Loss Ratio V_L/V_T Associated with the Present Solution (R) and the Classical Solution of Carter (C)

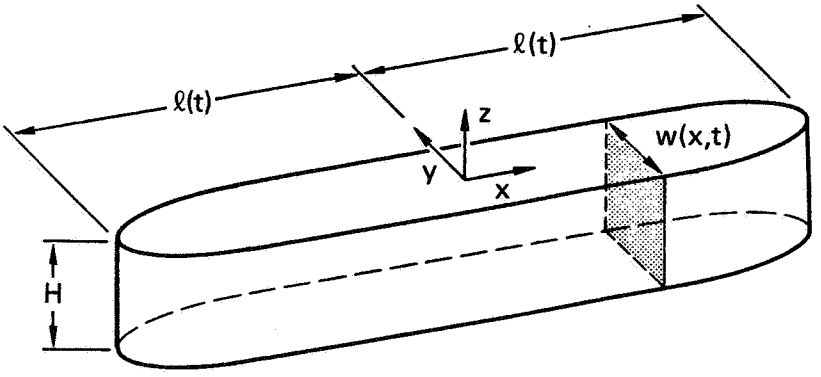

FIGURE 1 GEOMETRY OF VERTICAL FRACTURE
(Plane strain in horizontal planes)

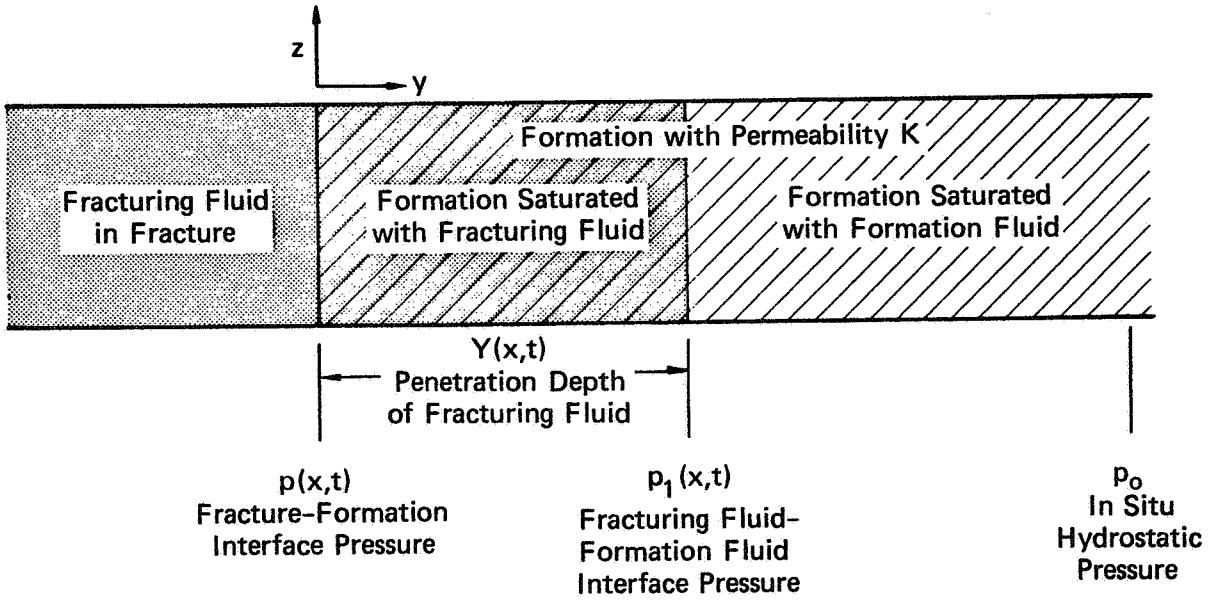

(a) ACTUAL FORMATION

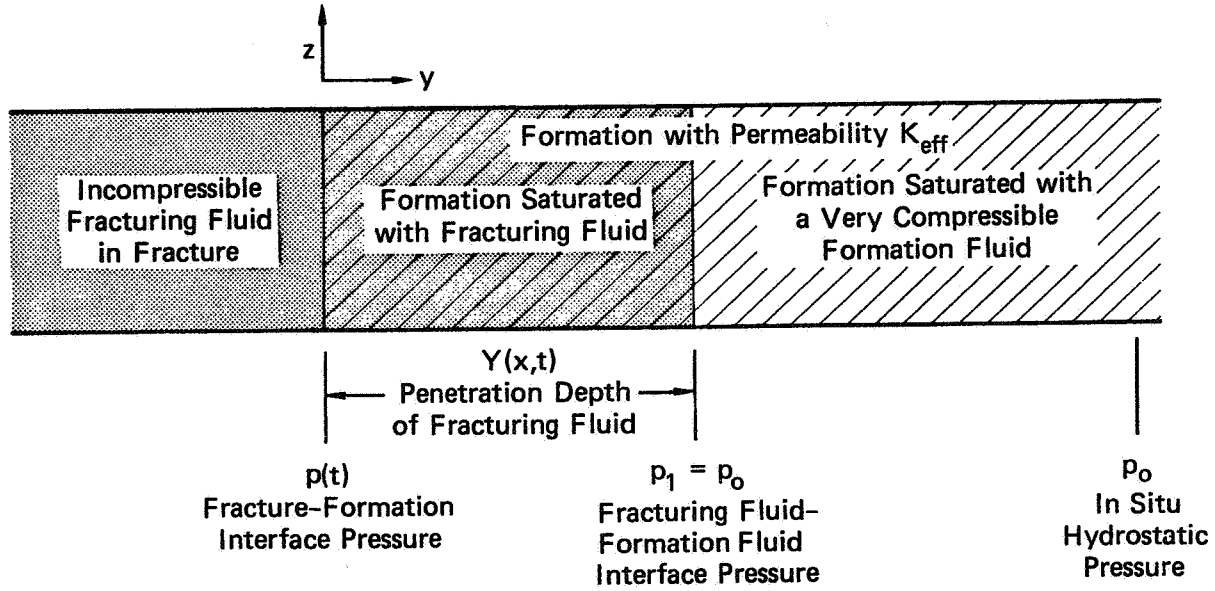

(b) MODEL FORMATION

MA-8975-44

FIGURE 2 CROSS SECTIONS (x = constant) THROUGH THE FRACTURE IN (a) THE ACTUAL FORMATION AND (b) THE MODEL FORMATION

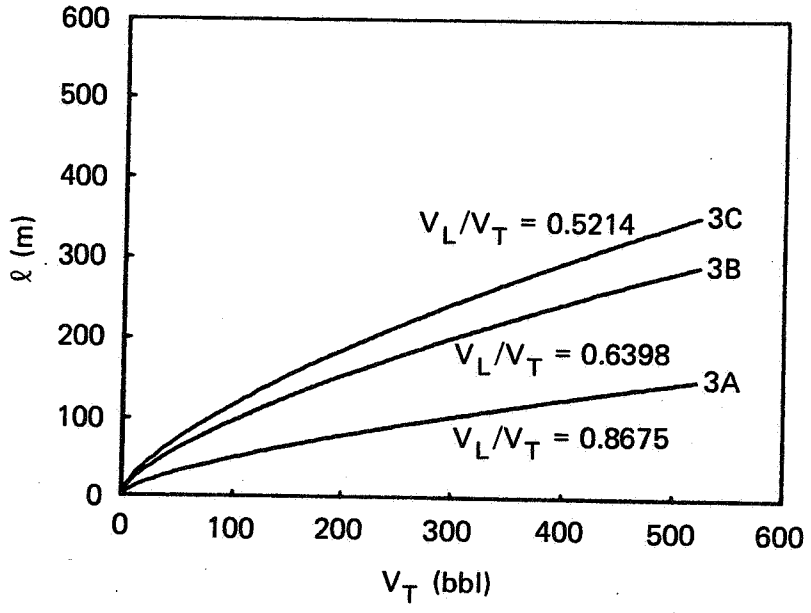

FIGURE 3 PREDICTIONS FOR THE FRACTURE HALF-LENGTH ℓ SHOWING THE EFFECT OF VARYING THE FRACTURING FLUID VISCOSITY μ OR THE PUMPING RATE q

Curves 3A, 3B and 3C are solutions for the parameters specified in Table 1.

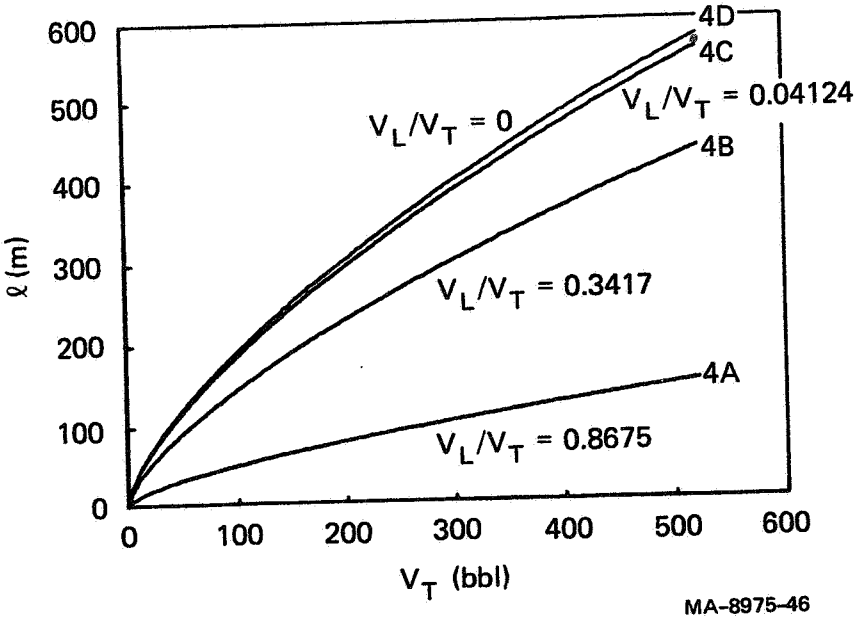

FIGURE 4 PREDICTIONS FOR THE FRACTURE HALF-LENGTH ℓ SHOWING THE EFFECT OF VARYING THE FORMATION FLUID COMPRESSIBILITY c_f

Curves 4A, 4B, 4C and 4D are solutions for the parameters specified in Table 1.

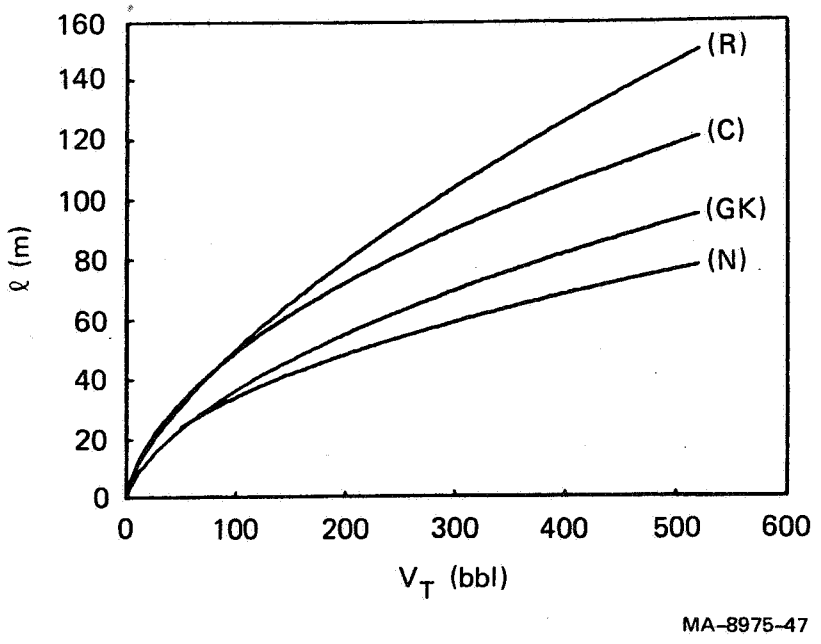

FIGURE 5 PREDICTIONS FOR THE FRACTURE HALF-LENGTH ℓ ASSOCIATED WITH THE PRESENT SOLUTION (R) AND THE SOLUTIONS OF CARTER (C), NORDGREN (N), AND GEERTSMA AND de KLERK (GK)

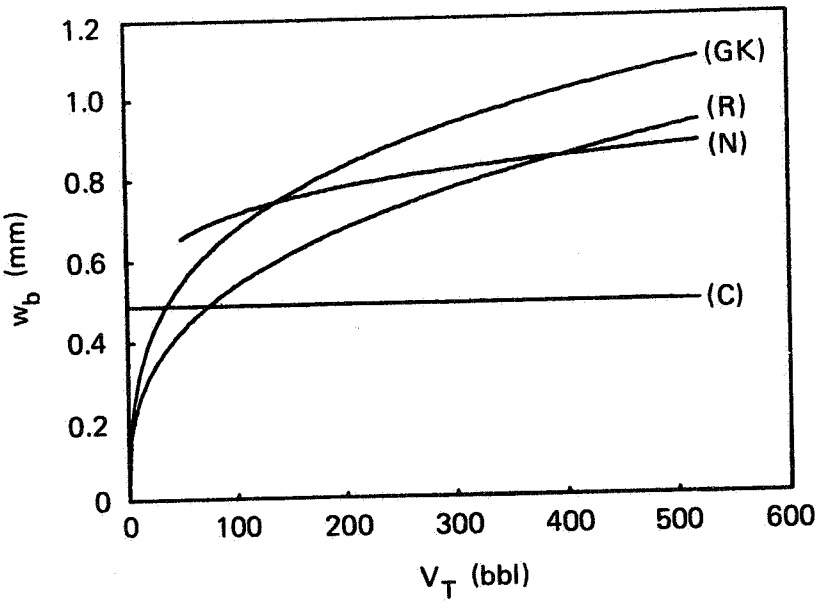

FIGURE 6 PREDICTIONS FOR THE FRACTURE WIDTH w_b AT THE BOREHOLE ASSOCIATED WITH THE PRESENT SOLUTION (R) AND THE SOLUTIONS OF CARTER (C), NORDGREN (N), AND GEERTSMA AND de KLERK (GK)

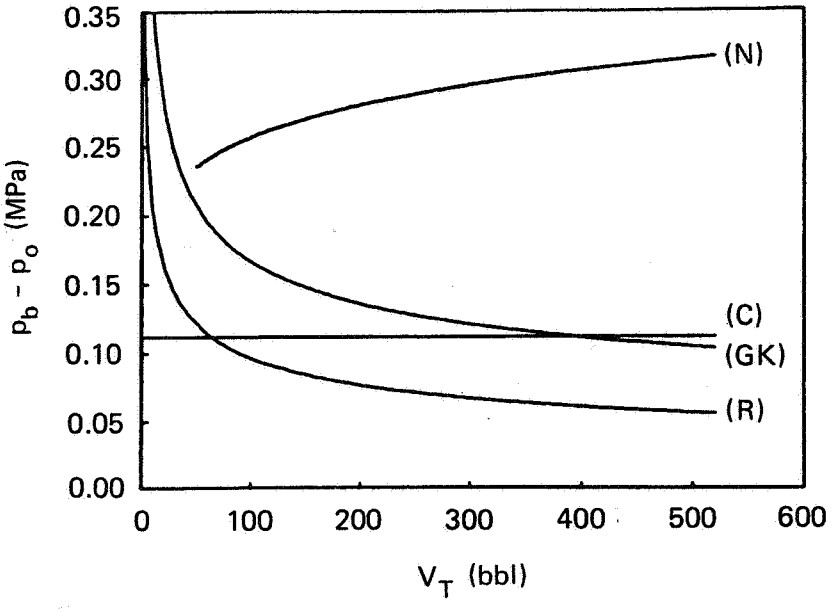

FIGURE 7 PREDICTIONS FOR THE EFFECTIVE PRESSURE AT THE BOREHOLE p_b-p_o ASSOCIATED WITH THE PRESENT SOLUTION (R) AND THE SOLUTIONS OF CARTER (C), NORDGREN (N), AND GEERTSMA AND de KLERK (GK)

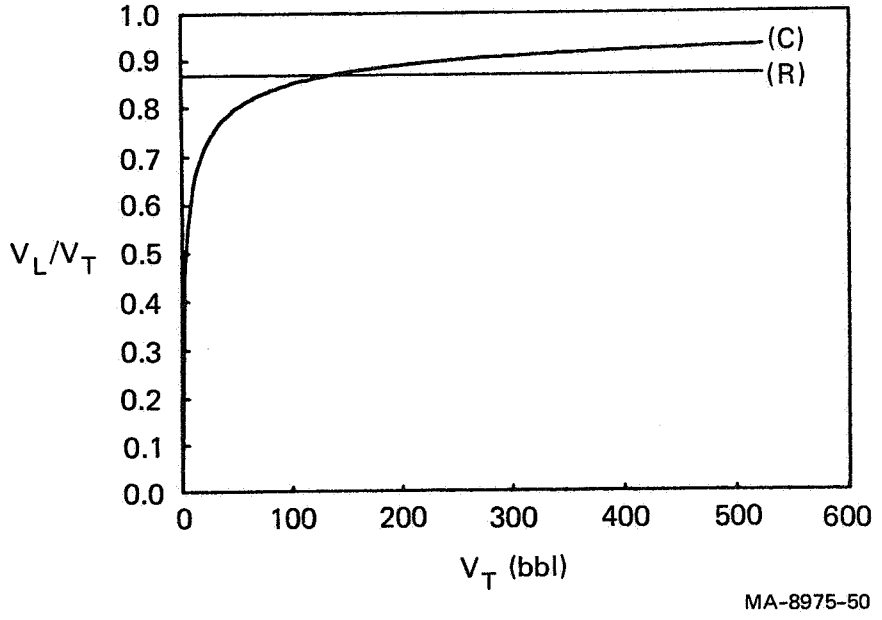

FIGURE 8 PREDICTIONS FOR THE FLUID LOSS RATIO V_L/V_T ASSOCIATED WITH THE PRESENT SOLUTION (R) AND THE CLASSICAL SOLUTION OF CARTER (C)

Appendix B

PHENOMENOLOGY EXPERIMENTS

In this appendix, we briefly describe one of the experiments that were conducted to obtain preliminary information about proppant transport during hydraulic fracture propagation. We also discuss of some experiments performed to investigate the effect of fluid viscosity.

In experiment 11, we used an impermeable model of PMMA similar to those described in Section 2, except no gages were used to measure the pressure in the fracture and the fracture width. The borehole pressure was recorded and the experiment was photographed using two movie cameras, one running at 297 fps and the other at 750 fps. The borehole of the model was filled with silicone carbide particles (ρ = 3.04 g•mℓ^{-1}, average diameter 50 μm). Then the model was connected to the motor pump (described in Section 2) and dyed water was used as a fracturing fluid. The model was fractured by pumping fluid at 73.2 mm^3/s without prefracturing the model as was done with the later impermeable experiments. When the borehole pressure reached about 30.7 MPa, the initial fracture propagated dynamically with an extension velocity of about 4 mm/ms, and then stopped. At about 0.4 s after fracture initiation, the model refractured and continued to refracture about every 3 s. Thus, the fracture propagation in the PMMA models that used water as a fracturing fluid typically was characterized by two phases that formed a repeating pattern: an unstable fracture propagation phase when the fracture propagated only for a short time (on the order of tens of milliseconds) followed by an inflation phase that lasted a relatively long time (on the order of a few seconds) as the fracture was inflating.

Figure B1 shows a frame from the movie film taken after pumping had ceased and before the borehole pressure was relieved. Notice that most of the proppants settled to the bottom of the fracture. Figure B2 is a photograph of the same model after the borehole pressure was relieved.

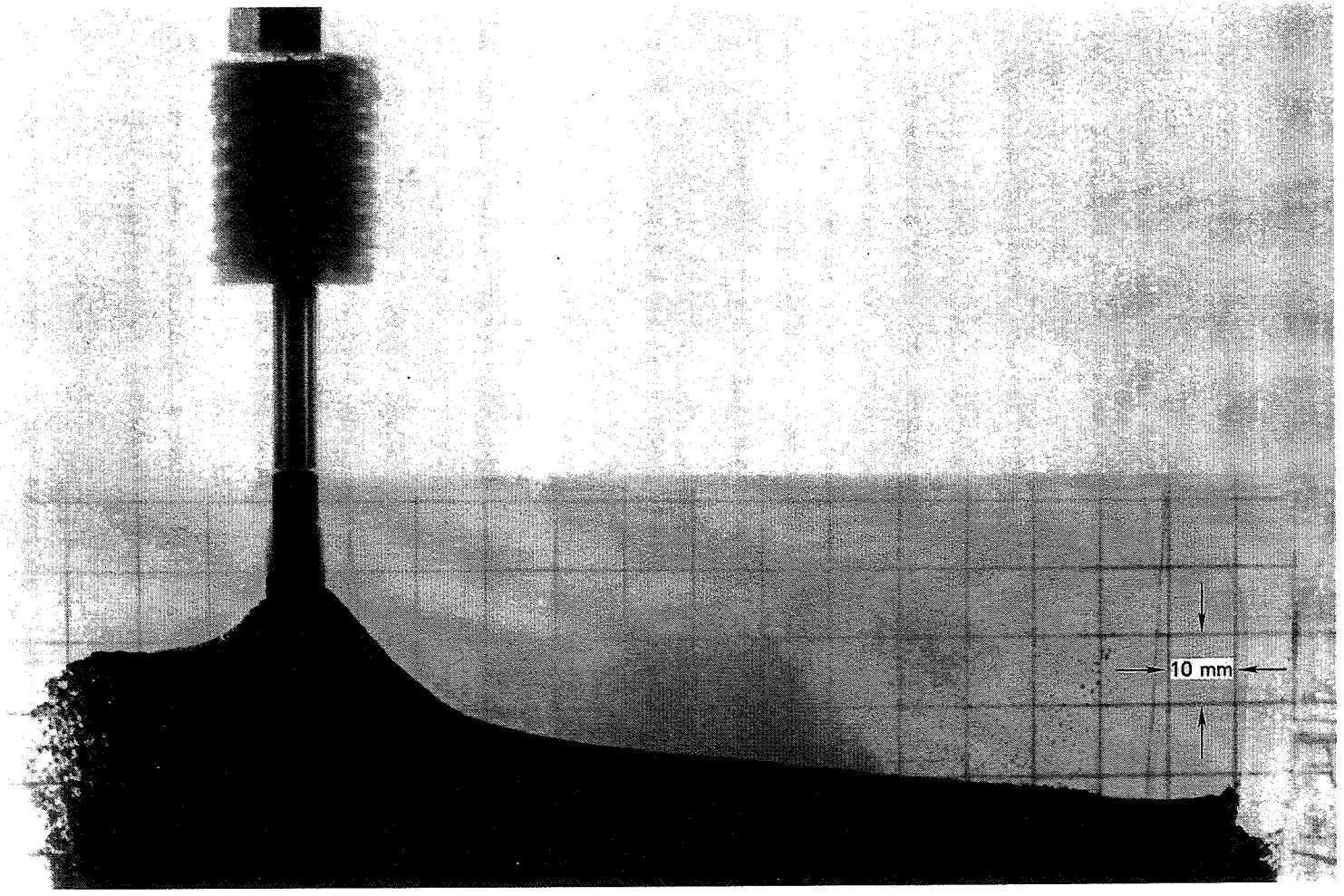

MP-8975-19

FIGURE B1 PROPPANT DISTRIBUTION IN MODEL 11 BEFORE BOREHOLE PRESSURE WAS RELIEVED

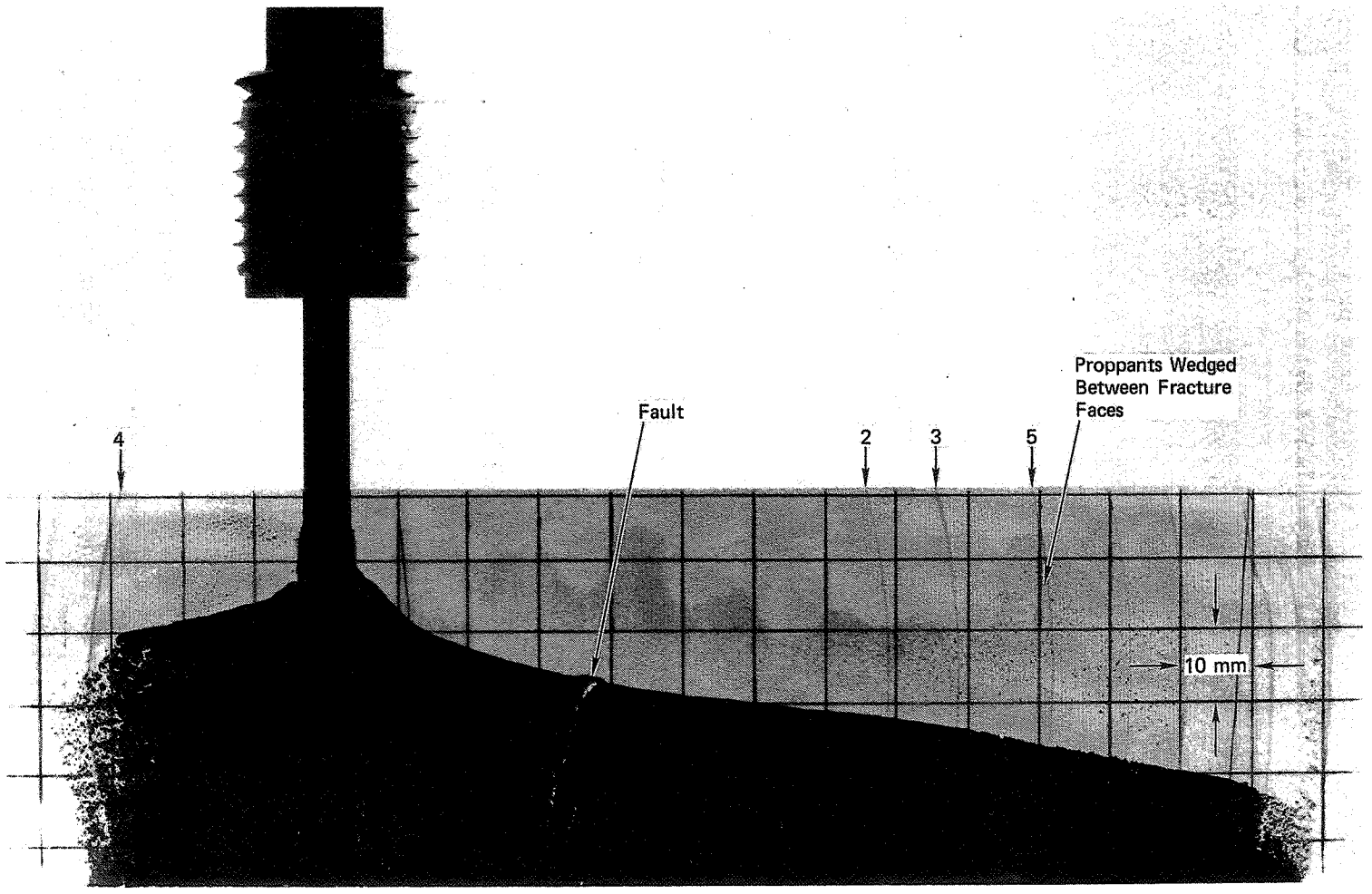

FIGURE B2 PROPPANT DISTRIBUTION IN MODEL 11 AFTER BOREHOLE PRESSURE WAS RELIEVED

When the fracture closed, some of the proppants were trapped between the fracture faces. Also, a fault in the proppant pack was created when the fracture closed. The mildly curved lines denoted by 2 through 5 in Figure B2 are typical of the lines created when the fracture propagation arrested. Each time the model refractured, the fracture tip advanced farther away from the borehole.

Figure B3 shows photographs of individual frames that have been reproduced from the movie taken at 297 fps. The elapsed time from fracture initiation is also recorded for each frame. In the first frame, the fracture width was so small that most of the proppants were filtered at the borehole so that only the smallest of proppants were carried by the fluid into the borehole. As the fracture width increased, more proppants were carried into the fracture. As proppants entered the fracture, they settled to the bottom.

From the movie, we observed that few proppants entered the fracture during the inflation phase of the fracture (described above) and that each time the model refractured it appeared that the proppant slurry moved into the fracture with a uniform horizontal velocity (parallel to the fracture plane) and a negligible vertical velocity so that relatively little mixing occurred. On the basis of these observations, we concluded that we could not obtain controlled proppant transport without fluid leak-off. Therefore, no quantitative data were obtained from impermeable experiments with proppants.

In Experiment 19, we tried to study the fracture geometry by fracturing an impermeable model with epoxy, letting the epoxy set, then sectioning the model. When epoxy was used as a fracturing fluid, the fracture propagated quasi-statically and continuously with an extension velocity of about 2.5×10^{-2} mm/ms, in contrast with an extension velocity of about 4 mm/ms when water was used as a fracturing fluid. The main difference between the epoxy and the water is the viscosity of the fluids. The analysis in Section 2.3 explains why a highly viscous fracturing fluid will have a stabilizing effect on fracture propagation.

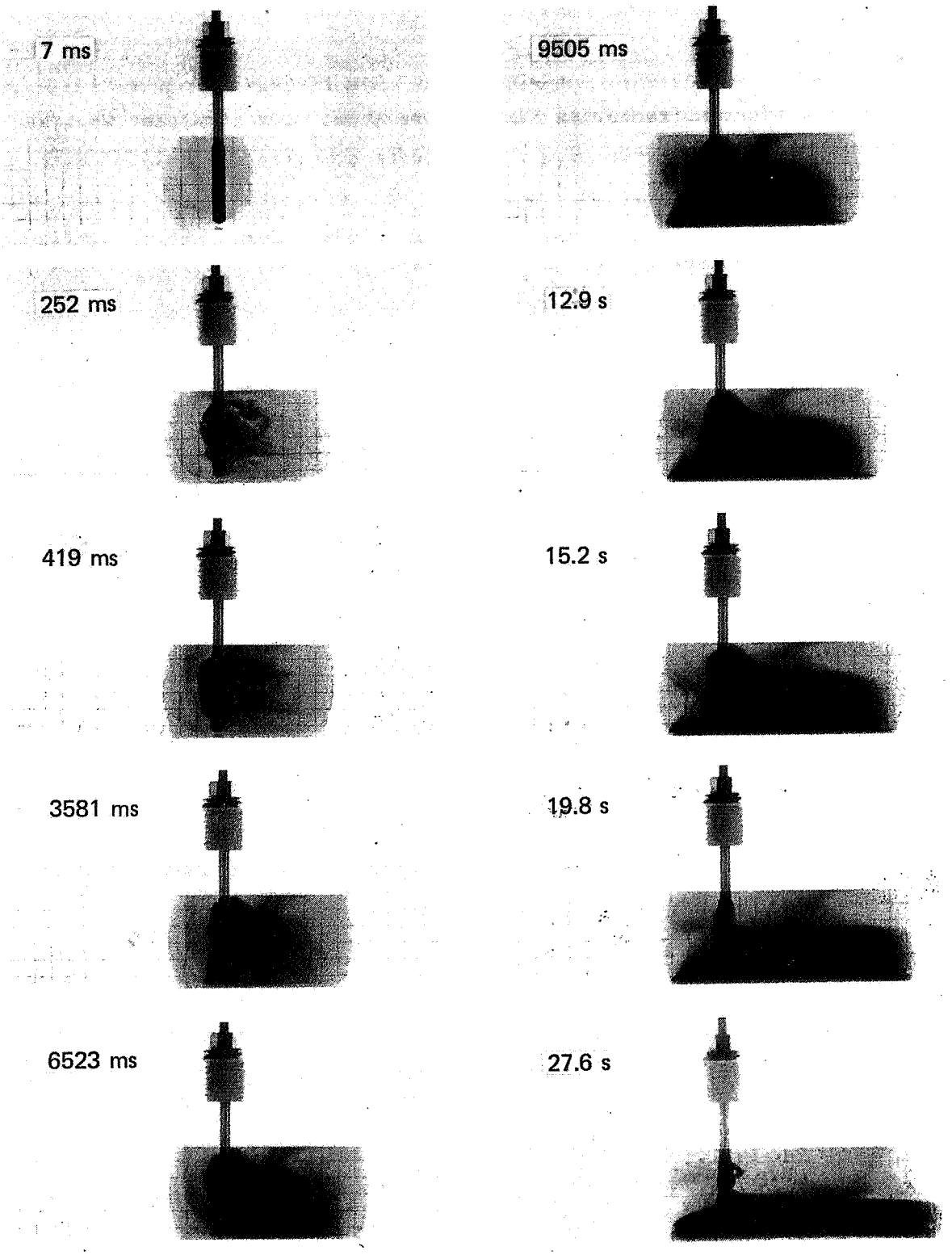

FIGURE B3 PROPPANT TRANSPORT DURING FRACTURE PROPAGATION IN MODEL 11

Since quasi-static continuous fracture propagation (associated with a highly viscous fracturing fluid) more accurately simulates what is expected in field tests than the discrete stepping (associated with an inviscid fracturing fluid, see Figure B2), we searched for a fracturing fluid, different from epoxy, that would produce quasi-static continuous fracture propagation. In experiment 20, we used Dow Corning 200 fluid (1,000 centistoke) as the fracturing fluid and in Experiment 21, Dow Corning 200 fluid (100,000 centistoke). In Experiment 20, the fracture propagated in discrete steps similar to the fracture propagation in Experiment 11 when water was used as a fracturing fluid. However, in Experiment 21, the fracture propagated quasi-statically and continuously as it did in Experiment 19 when epoxy was used as a fracturing fluid. Therefore, Dow Corning 200 fluid (100,000 centistoke) was chosen as the fracturing fluid for the impermeable experiments described in Section 2.

Appendix C

PMMA INTERFACE CONDITIONS

Here we describe a brief study of the conditions that exist at the intersection of the fracture and the chloroform welds, which bond together the layers of PMMA in our impermeable models (see Figure C1). These conditions were examined because a numerical simulation of the propagation of a vertical fracture contained between two horizontal planes requires making assumptions about the conditions existing at the intersections of the fracture with these planes. Since our main objective in conducting scaled model hydrofracture experiments is to provide quantitative data for computer code development and verification, it is important to examine these conditions, at least qualitatively.

A vertical cross section (see Figure C1) was taken from model 24, which was fractured with Dow Corning 200 fluid (100,000 centistoke). Figure C2 is a photograph of the fracture tip that stopped propagating in the chloroform weld (magnified 100X). Notice the bulb-shaped fracture tip and the minor microcracking of the chloroform weld. The residual width of the fracture and fracture tip must be caused by permanent deformation of the chloroform weld because the fracture opening is not maintained by fluid pressure. The fact that the fracture tip remained open after pressure was relieved in the fracture suggests that although the top and bottom PMMA layers of the models give support to the middle layer, plane strain conditions may still exist in horizontal planes of the middle layer.

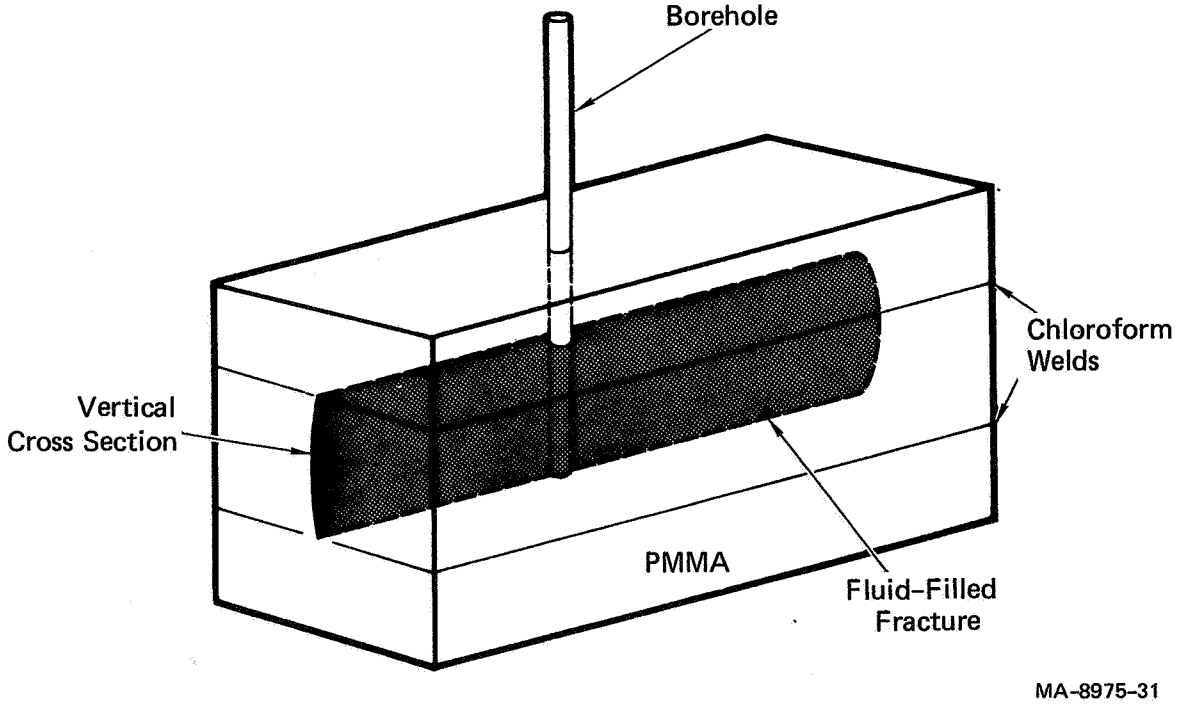

FIGURE C1 VERTICAL CROSS SECTION TAKEN FROM MODEL 24

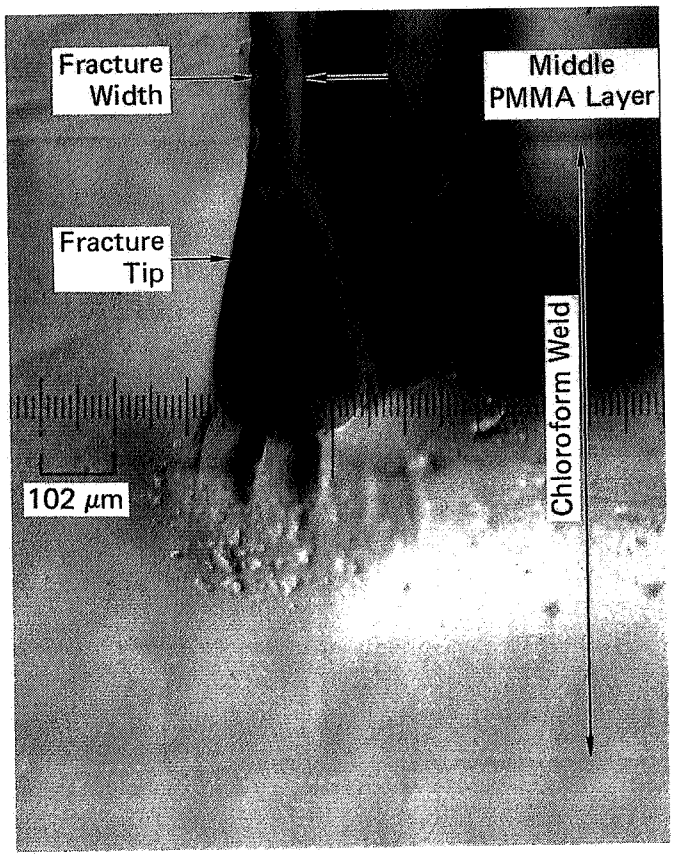

MP-8975-41

FIGURE C2 PHOTOGRAPH OF THE FRACTURE TIP THAT ARRESTED IN THE CHLOROFORM WELD OF MODEL 24 WHEN DOW 200 FLUID (100,000 centistoke) WAS USED AS A FRACTURING FLUID

(Magnified 100X)